

The Pennsylvania State University  
The Graduate School  
Eberly College of Science

**DEVELOPMENT OF SCALABLE APPROACHES TO NEUTRINO MASS  
MEASUREMENT USING CRES**

A Thesis in  
The Physics Department  
by  
Andrew Douglas Ziegler

© 2023 Andrew Douglas Ziegler

Submitted in Partial Fulfillment  
of the Requirements  
for the Degree of

Doctor of Philosophy

December 2023

The thesis of Andrew Douglas Ziegler was reviewed and approved\* by the following:

Luiz de Viveiros Souza  
Assistant Professor of Physics  
Thesis Advisor  
Chair of Committee

Carmen Carmona  
Assistant Professor of Physics

Doug Cowan  
Professor of Physics and Astrophysics

Xingjie Ni  
Associate Professor of Electrical Engineering

Stephanie Wissel  
Associate Professor of Physics

\*Signatures are on file in the Graduate School.

# **Abstract**

Some shit goes here.

# Table of Contents

List of Figures	viii
List of Tables	viii
Acknowledgments	viii
Chapter 1 Introduction	1
Chapter 2 Neutrinos and Neutrino Masses	2
2.1 Introduction . . . . .	2
2.2 Neutrinos . . . . .	2
2.3 Neutrino Oscillations . . . . .	2
2.4 Neutrino Mass . . . . .	3
2.4.1 Limits from Cosmology . . . . .	3
2.4.2 Limits from Neutrinoless Double Beta-decay Searches . . . . .	3
2.4.3 Kinematic Measurements of the Neutrino Mass . . . . .	4
2.5 Neutrino Mass Measurements Using Tritium Beta-decay Spectroscopy . . . . .	4
Chapter 3 Direct Measurement of the Neutrino Mass with Cyclotron Radiation Emission Spectroscopy	7
3.1 Introduction . . . . .	7
3.2 Cyclotron Radiation Emission Spectroscopy . . . . .	7
3.2.1 Charged Particles in a Magnetic Trap . . . . .	8
3.2.2 Radiation from a Charged Particle . . . . .	8
3.3 The Project 8 Collaboration . . . . .	8
3.3.1 Neutrino Mass Sensitivity Goals . . . . .	8
3.3.2 Phased Development Plans . . . . .	8
3.4 Phase II: First Tritium Beta Decay Spectrum and Neutrino Mass Measurement with CRES . . . . .	8
3.4.1 The Project 8 CRES Demonstrator . . . . .	8
3.4.2 CRES Track and Event Reconstruction . . . . .	8
3.4.3 Measurements with Krypton . . . . .	8

3.4.4	Tritium Spectrum and Neutrino Mass Results . . . . .	8
3.5	Phase III: Developing Free-space CRES Measurements with Antenna Arrays . . . . .	8
3.5.1	The Basic Approach . . . . .	9
3.5.2	The FSCD: Free Space CRES Demonstrator . . . . .	11

## **Chapter 4**

	<b>Signal Reconstruction Techniques for Antenna Array CRES and the FSCD</b>	<b>15</b>
4.1	Introduction . . . . .	15
4.2	FSCD Simulations . . . . .	16
4.2.1	Kassiopeia . . . . .	17
4.2.2	Locust . . . . .	21
4.2.3	CRESana . . . . .	25
4.3	Signal Detection and Reconstruction Techniques for Antenna Array CRES . . . . .	26
4.3.1	Digital Beamforming . . . . .	30
4.3.2	Matched Filtering . . . . .	38
4.3.3	Machine Learning . . . . .	45
4.4	Analysis of Signal Detection Algorithms for the Antenna Array Demonstrator . . . . .	49
4.4.1	Introduction . . . . .	49
4.4.2	Signal Detection with Antenna Array CRES . . . . .	52
4.4.2.1	Antenna Array and DAQ System . . . . .	52
4.4.2.2	Real-time Signal Detection . . . . .	54
4.4.3	Signal Detection Algorithms . . . . .	58
4.4.3.1	Power Threshold . . . . .	58
4.4.3.2	Matched Filtering . . . . .	60
4.4.3.3	Machine Learning . . . . .	64
4.4.4	Methods . . . . .	66
4.4.4.1	Data Generation . . . . .	66
4.4.4.2	Template Number and Match Estimation . . . . .	67
4.4.4.3	CNN Training and Data Augmentation . . . . .	68
4.4.5	Results and Discussion . . . . .	69
4.4.5.1	Trigger Classification Performance . . . . .	69
4.4.5.2	Computational Cost and Hardware Requirements . . . . .	71
4.4.6	Conclusion . . . . .	73

## **Chapter 5**

	<b>Antenna and Antenna Measurement System Development for the Project 8 Experiment</b>	<b>75</b>
5.1	Introduction . . . . .	75
5.2	Antenna Measurements for CRES experiments . . . . .	76
5.2.1	Antenna Parameters . . . . .	76
5.2.1.1	Radiation Patterns . . . . .	76
5.2.1.2	Directivity and Gain . . . . .	77
5.2.1.3	Far-field and Near-field . . . . .	78

5.2.1.4	Polarization . . . . .	79
5.2.1.5	Antenna Factor and Effective Aperture . . . . .	80
5.2.2	Antenna Measurement Fundamentals . . . . .	82
5.2.2.1	Friis Transmission Equation . . . . .	82
5.2.2.2	S-Parameters and Network Analyzers . . . . .	83
5.2.2.3	Antenna Array Commissioning and Calibration Measurements . . . . .	84
5.2.3	The Penn State Antenna Measurement System . . . . .	85
5.3	Development of a Synthetic Cyclotron Antenna (SYNCA) for Antenna Array Calibration . . . . .	89
5.3.1	Introduction . . . . .	89
5.3.2	Cyclotron Radiation Phenomenology . . . . .	92
5.3.3	SYNCA Simulations and Design . . . . .	98
5.3.4	Characterization of the SYNCA . . . . .	102
5.3.5	Beamforming Measurements with the SYNCA . . . . .	106
5.3.6	Conclusions . . . . .	109
5.4	FSCD Antenna Array Measurements with the SYNCA . . . . .	110
5.4.1	Introduction . . . . .	110
5.4.2	Measurement Setups . . . . .	112
5.4.2.1	FSCD Array Setup . . . . .	112
5.4.2.2	Synthetic Array Setup . . . . .	114
5.4.3	Simulations, Analysis, and Results . . . . .	115
5.4.3.1	Simulations . . . . .	115
5.4.3.2	Phase Analysis . . . . .	116
5.4.3.3	Magnitude Analysis . . . . .	121
5.4.3.4	Beamforming Characterization . . . . .	124
5.4.4	Conclusions . . . . .	127

<b>Chapter 6</b>		
<b>Development of Resonant Cavities for Large Volume CRES Measurements</b>	<b>128</b>	
6.1	Introduction . . . . .	128
6.2	Cylindrical Resonant Cavities . . . . .	129
6.2.1	General Field Solutions . . . . .	129
6.2.2	TE and TM Modes . . . . .	130
6.2.3	Resonant Frequencies of a Cylindrical Cavity . . . . .	132
6.2.4	Cavity Q-factors . . . . .	134
6.3	The Cavity Approach to CRES . . . . .	138
6.3.1	A Sketch of a Molecular Tritium Cavity CRES Experiment . . . . .	138
6.3.2	Magnetic Field, Cavity Geometry, and Resonant Modes . . . . .	140
6.3.3	Trade-offs Between the Antenna and Cavity Approaches . . . . .	143
6.4	Single-mode Resonant Cavity Design and Simulations . . . . .	145
6.4.1	Open Cylindrical Cavities with Coaxial Terminations . . . . .	145
6.4.2	Mode Filtering . . . . .	148

6.4.3	Simulations of Open, Mode-filtered Cavities . . . . .	150
6.5	Single-mode Resonant Cavity Measurements . . . . .	153
6.5.1	Cavities and Setup . . . . .	153
6.5.2	Results and Discussion . . . . .	155
	<b>Bibliography</b>	<b>158</b>

# **Acknowledgments**

Shout out to all the haters.

# **Dedication**

Something heartfelt.

# **Chapter 1**

---

## **Introduction**

# Chapter 2

## Neutrinos and Neutrino Masses

### 2.1 Introduction

### 2.2 Neutrinos

### 2.3 Neutrino Oscillations

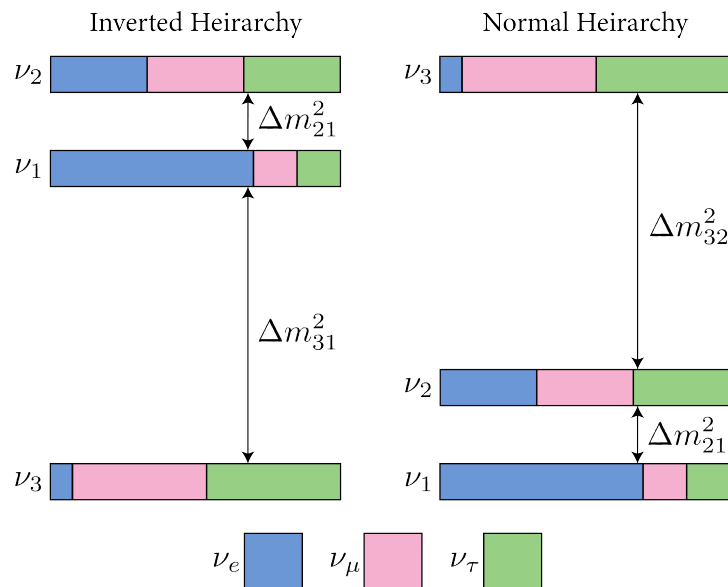


Figure 2.1: Caption

## 2.4 Neutrino Mass

### 2.4.1 Limits from Cosmology

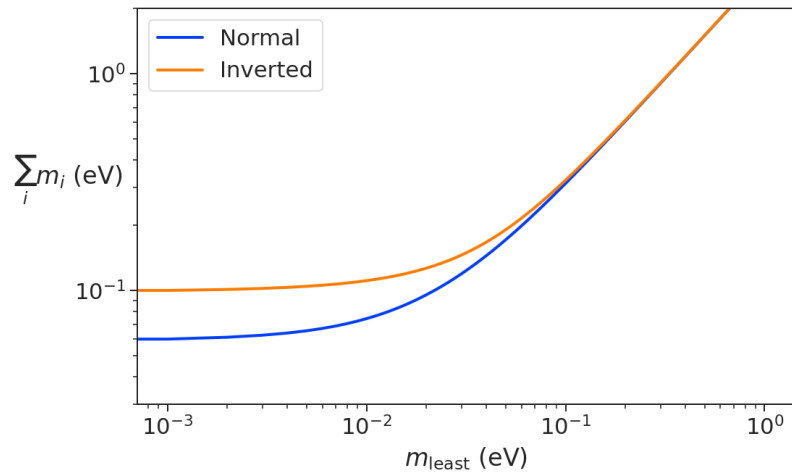


Figure 2.2: Caption

### 2.4.2 Limits from Neutrinoless Double Beta-decay Searches

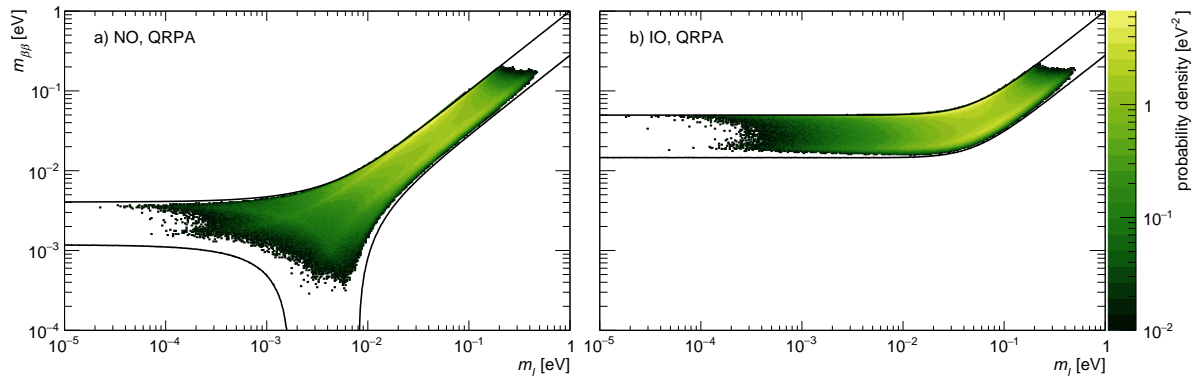


Figure 2.3: Caption



Figure 2.4: Caption



Figure 2.5: Caption

### 2.4.3 Kinematic Measurements of the Neutrino Mass

## 2.5 Neutrino Mass Measurements Using Tritium Beta-decay Spectroscopy

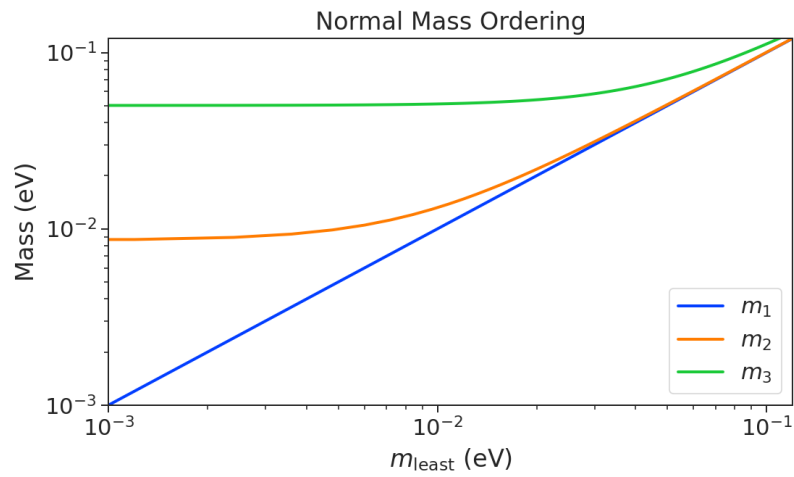


Figure 2.6: Caption

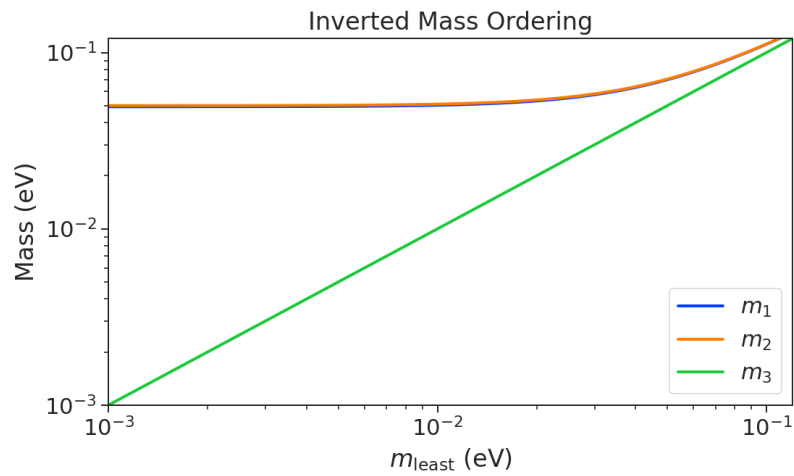


Figure 2.7: Caption



Figure 2.8: Caption

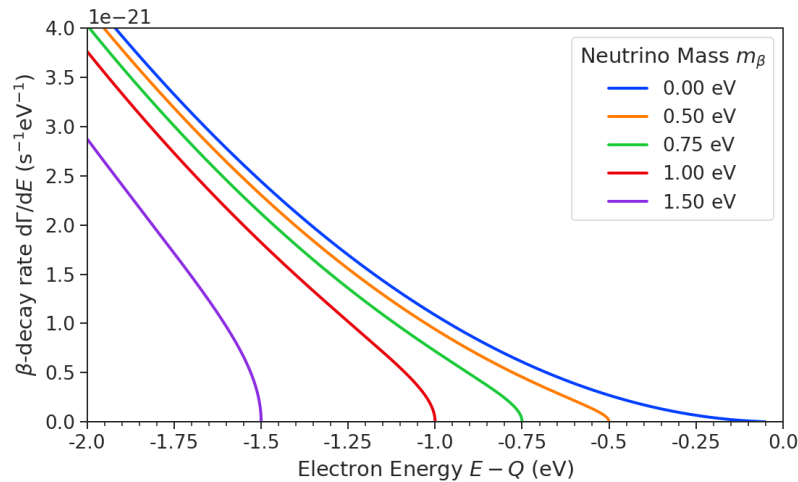


Figure 2.9: Caption

# **Chapter 3**

## **Direct Measurement of the Neutrino Mass with Cyclotron Radiation Emission Spec- troscopy**

### **3.1 Introduction**

### **3.2 Cyclotron Radiation Emission Spectroscopy**

Of the standard physical quantities the one that can be measured with the highest precision is time and the inversely related quantity frequency. In fact it is often advantageous to convert measurements of other physical quantities like mass or length into frequency measurements due to the digital nature of frequency measurements that make them immune to many sources of noise. Atomic clocks, which operate by measuring the frequencies of various atomic transitions, have been used to measure time with astounding relative uncertainties of  $10^{-18}$  seconds. The extreme precision possible with frequency measurements is often summarized using the a quote from the Physicist Arthur Schawlow who said advise his students to "Never measure anything but frequency!".

Neutrino mass measurements using tritium beta-decay are effectively attempting to measure

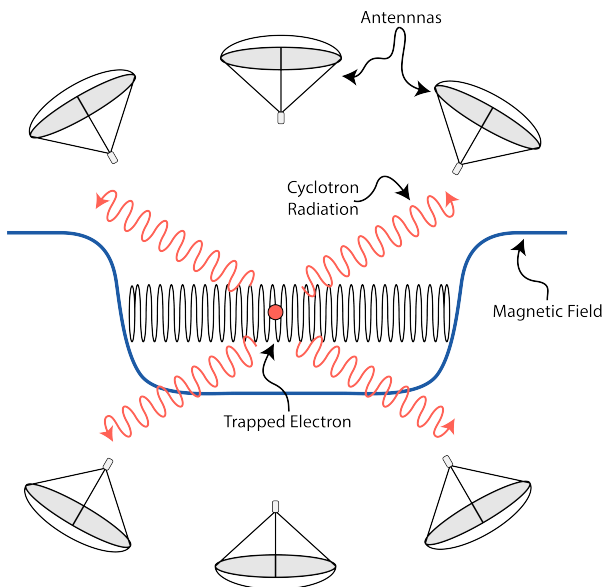


Figure 3.1: Caption

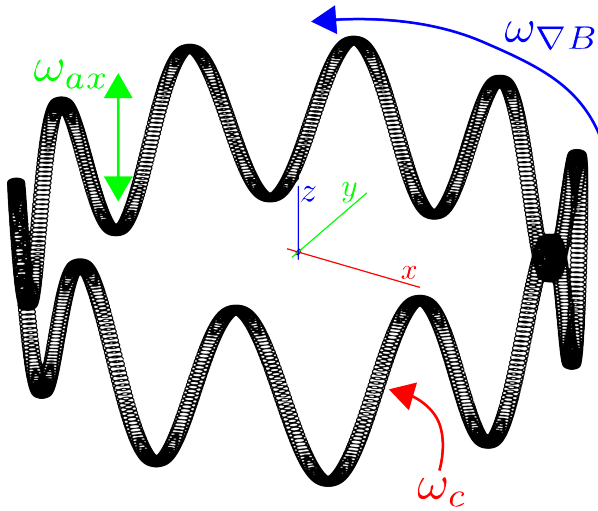


Figure 3.2: Caption

### 3.2.1 Charged Particles in a Magnetic Trap

### 3.2.2 Radiation from a Charged Particle

## 3.3 The Project 8 Collaboration

### 3.3.1 Neutrino Mass Sensitivity Goals

### 3.3.2 Phased Development Plans

## 3.4 Phase II: First Tritium<sub>8</sub> Beta Decay Spectrum and Neutrino Mass Measurement with CRES

### 3.4.1 The Project 8 CRES Demonstrator

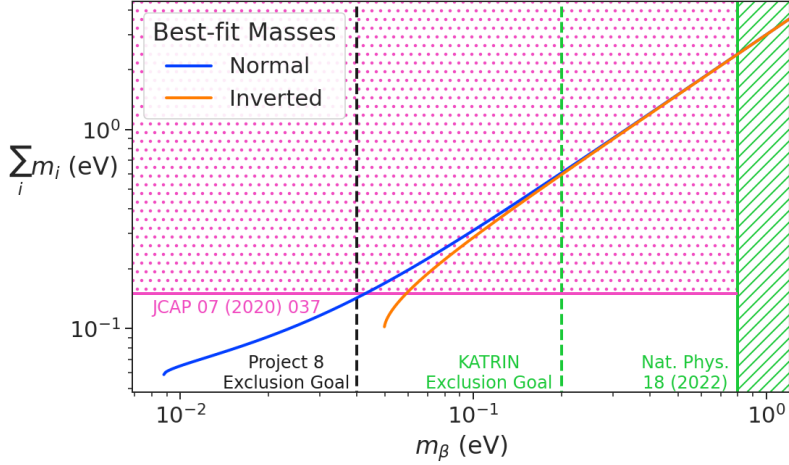


Figure 3.3: Caption

mass with a target sensitivity of 40 meV. One of the key technologies is a method for performing high resolution CRES measurements in a large volume, which allows one to observe a sufficient quantity of tritium to measure the low-activity endpoint region of the tritium spectrum.

### 3.5.1 The Basic Approach

One possible approach, suggested in the original CRES publication, is to use many antennas to surround a volume of tritium gas in a magnetic field (see Figure 3.10). When a decay occurs the electron will begin to emit cyclotron radiation that can be collected by the array and used to perform CRES. Scaling to large volumes with the antenna array approach is accomplished by increasing the number of antennas in the array, which increases the volume under observation proportionally.

Several features of the antenna array approach make it an attractive candidate technology for a large volume experiment. One example is the accurate position reconstruction made possible by the multichannel nature of the array. Using techniques like digital beamforming it is possible to estimate the radial and azimuthal positions of the electron in the magnetic trap with a precision significantly less than the size of the cyclotron wavelength. This capability allows one to perform event-by-event estimations of the magnetic field experienced by an electron, which is crucial to achieving high energy resolution with the CRES technique.

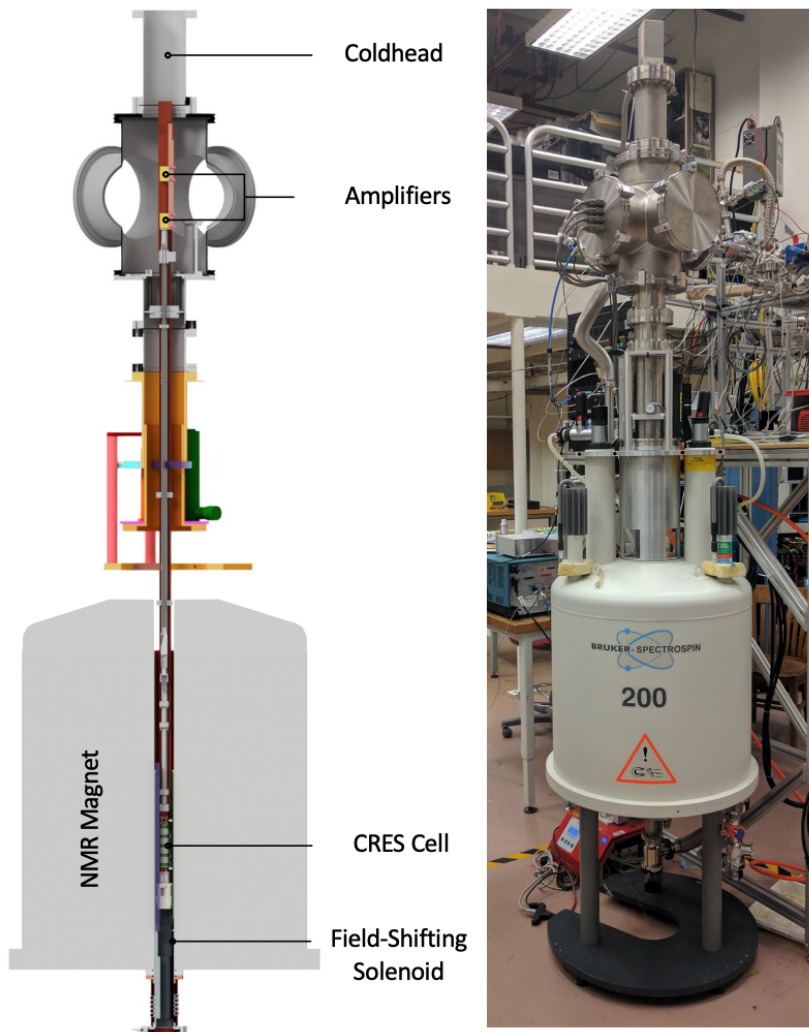


Figure 3.4: Caption

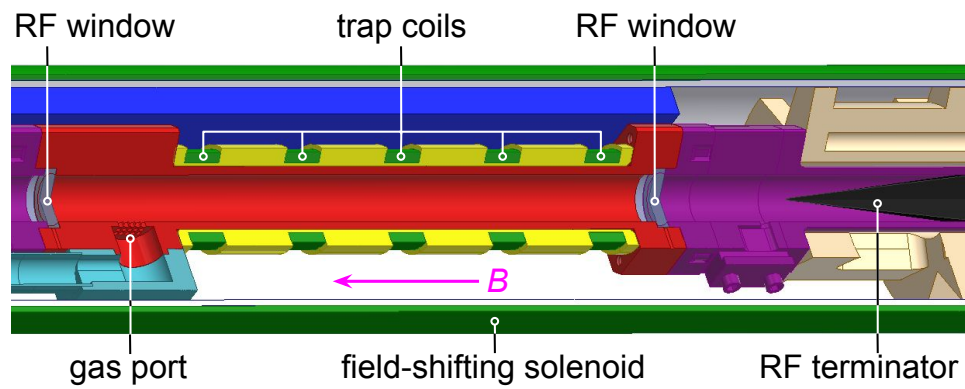


Figure 3.5: Caption

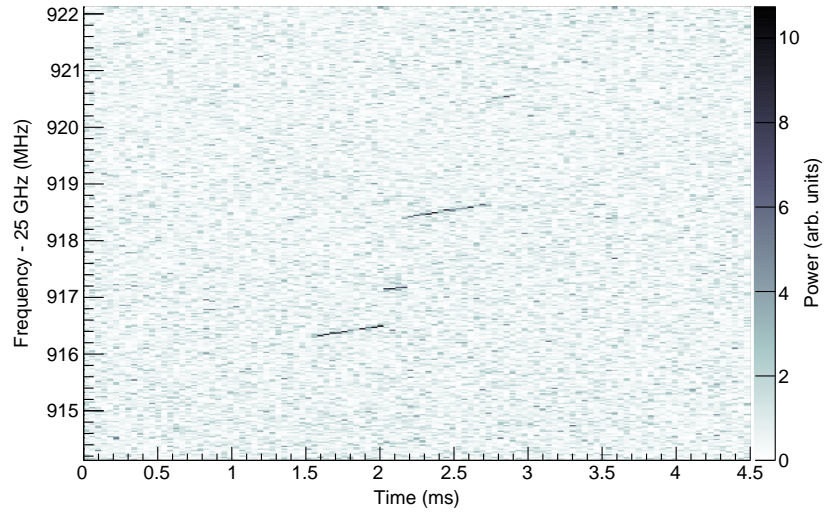


Figure 3.6: Caption

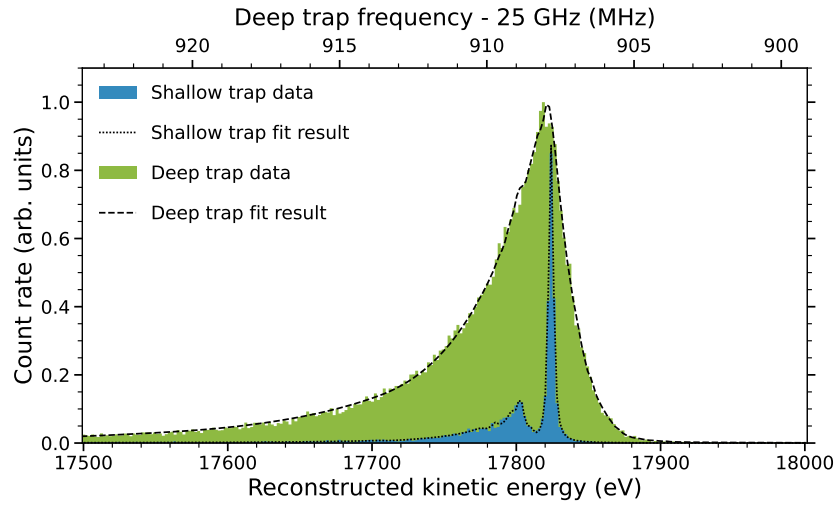


Figure 3.7: Caption

### 3.5.2 The FSCD: Free Space CRES Demonstrator

Magnetic Field

Gas System and Tritium Source

Antenna Array

Scaling

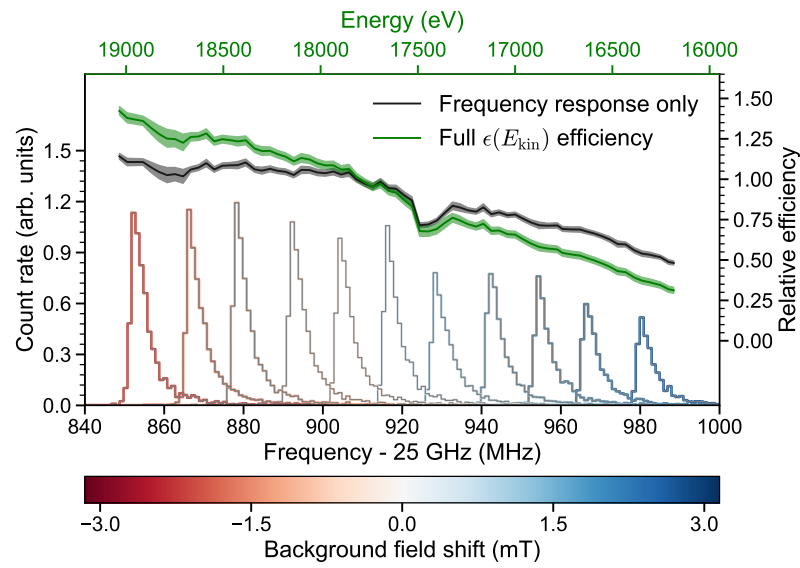


Figure 3.8: Caption

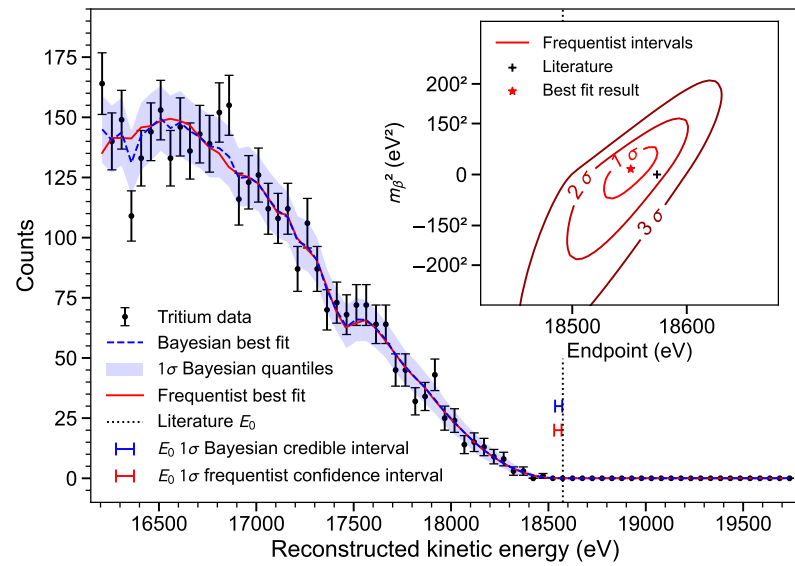


Figure 3.9: Caption

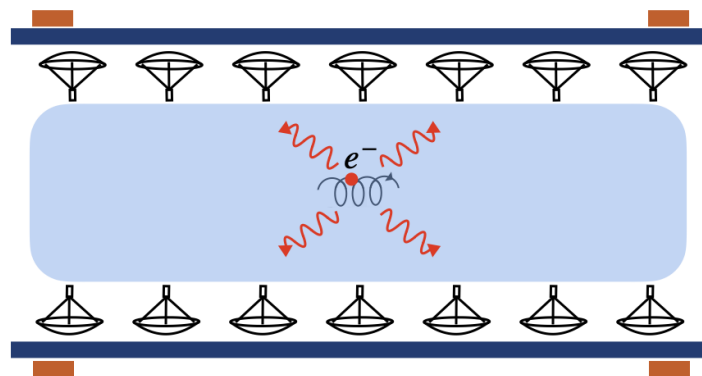


Figure 3.10



Figure 3.11

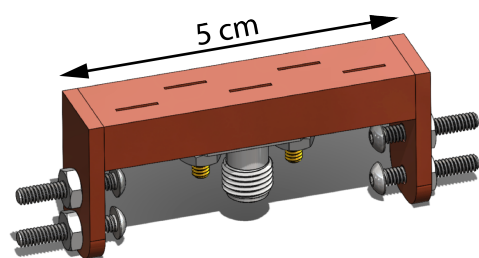


Figure 3.12

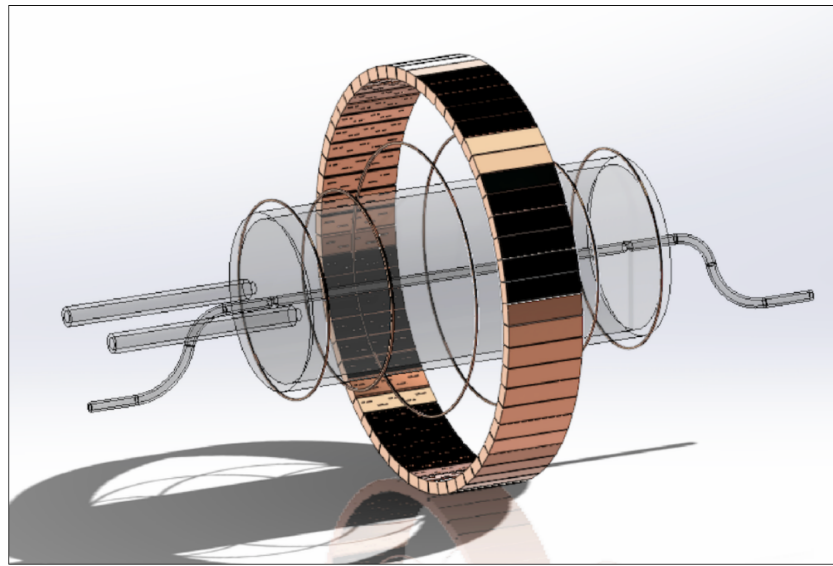


Figure 3.13

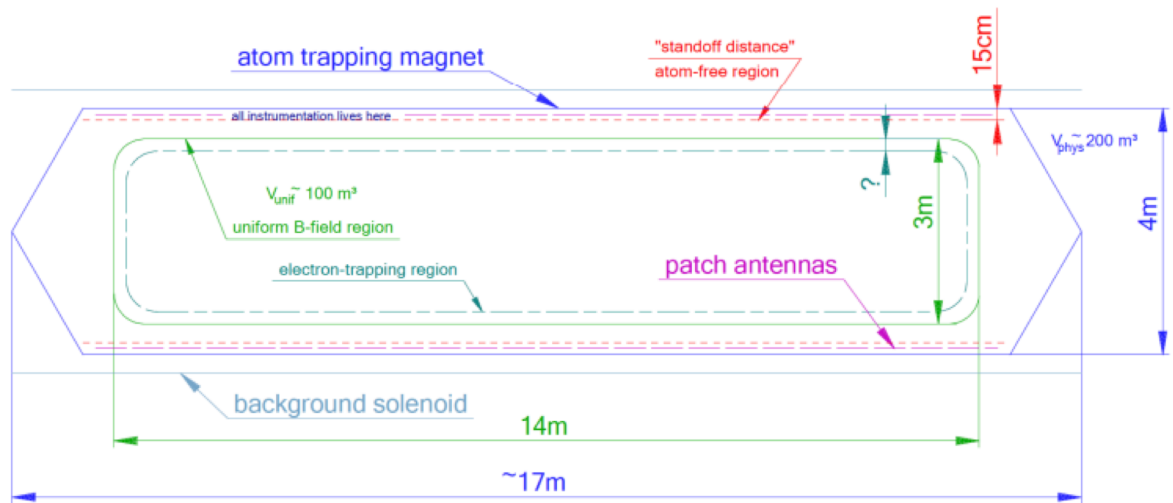


Figure 3.14

# **Chapter 4**

## **Signal Reconstruction Techniques for Antenna Array CRES and the FSCD**

### **4.1 Introduction**

The transition from a CRES experiment that utilizes the waveguide gas cell technology to an antenna array based experiment introduces new challenges related to data acquisition, signal detection, and signal reconstruction due to the multi-channel nature of the data. The development of signal reconstruction algorithms is crucial to the design of antenna array based experiments like the FSCD, because these algorithms directly influence the detection efficiency and energy resolution of the CRES experiment. In this Chapter I summarize my contributions to the development and analysis of signal reconstruction and detection algorithms for the FSCD experiment.

In Section 4.2 we discuss the primary tool for this work, which is the Locust simulations package developed by the Project 8 experiment for the simulation of CRES events in the detector. This package utilizes the Kassiopeia package to obtain particle trajectory solutions for electrons in the magnetic trap. The trajectory solutions can then be used to calculate the response of the antenna array to the cyclotron radiation produced by the electron, which results in signals that can be used to analyze the performance of different signal reconstruction algorithms. More recently, Project 8 has developed CREsana, which is a new simulations package that takes a more analytical approach to CRES signal simulations for antenna arrays. Although CREsana signals were not used for the signal reconstruction algorithm development detailed here, we introduce the software as it plays a role in the antenna array measurements presented in Section 5.4.

In Section 4.3 we discuss the signal reconstruction and detection approaches analyzed for the FSCD experiment. In general there are two steps to signal reconstruction: detection and parameter estimation. With signal detection one is primarily concerned

only with distinguishing between data that contains a signal versus data that contains only noise, whereas, with parameter estimation one is interested in extracting the kinematic parameters of the electron encoded in the cyclotron radiation signal shape. Due to the low signal power of electrons near the spectrum endpoint in the FSCD experiment, signal detection is a non-trivial problem. This is magnified by the need to maximize the detection efficiency of the experiment in order to achieve the neutrino mass sensitivity goals. My contributions to signal reconstruction analysis for the FSCD are focused on this signal detection component of reconstruction.

After the discussion of various signal detection approaches, in Section 4.4 we present a more detailed analysis of the detection performance of three algorithms, which could be used to signal detection in the FSCD. This section was originally prepared for publication in JINST as a separate paper. The algorithms include a digital beamforming algorithm, a matched filter algorithm, and a neural network algorithm, which we analyze in terms of both classification accuracy and estimated computational cost.

## 4.2 FSCD Simulations

Simulating the FSCD and antenna array CRES requires a combination of different capabilities not often found in a single simulation tool. First of all, accurate calculations of the magneto-static fields produced by current-carrying coils are required in order to accurately model the magnetic trap and background magnets. The resulting magnetic fields must then be used to calculate the exact relativistic trajectory of electrons, which is required in order to calculate the electro-magnetic (EM) fields produced by the acceleration of the electron. Finally, the simulation has to model the interaction of the antenna and RF receiver chain with these EM-fields in order to produce the simulated voltage signals produced by the antenna array during the CRES event. At the time when Project 8 was developing this simulation capability, no single available simulation tool was known to adequately perform this suite of calculations, which prompted the development of custom simulation framework to simulate the FSCD. This simulation framework includes custom simulation tools developed by Project 8 as well as other open-source and proprietary software developed by third-parties.

### 4.2.1 Kassiopeia

Kassiopeia<sup>1</sup> is a particle tracking and static EM-field solver developed by the KATRIN collaboration for simulations of their spectrometer based on magnetic adiabatic collimation with an electrostatic filter [1]. Due to the measurement technique employed by the KATRIN collaboration, Kassiopeia is not designed to solve for the EM-fields produced by electrons in magnetic fields. However, it does provide efficient solvers for static electric and magnetic fields and charged particle trajectory solvers. Because of this, Project 8 has incorporated parts of Kassiopeia into its own simulation framework.

#### Magnetostatic Field Solutions

The solutions to the electric and magnetic fields generated by a static configuration of charges and currents is given by Maxwell's equations in the limit where the time-dependent terms go to zero. In their static form Maxwell's equations are

$$\nabla \cdot \mathbf{E} = \frac{\rho}{\epsilon_0} \quad (4.1)$$

$$\nabla \times \mathbf{E} = 0 \quad (4.2)$$

$$\nabla \cdot \mathbf{B} = 0 \quad (4.3)$$

$$\nabla \times \mathbf{B} = \mu_0 \mathbf{J}, \quad (4.4)$$

where we can see that the electric and magnetic fields are now completely decoupled from each other. The solution for the magnetic field in this boundary value problem is given by the Biot-Savart law

$$\mathbf{B}(\mathbf{r}) = \frac{\mu_0}{4\pi} \int dr' \frac{r'^3 \mathbf{J}(\mathbf{r}') \times (\mathbf{r} - \mathbf{r}')}{|\mathbf{r}' - \mathbf{r}|^3}, \quad (4.5)$$

which Kassiopeia uses a variety of numeric integration techniques to solve for a user defined current distribution.

#### Kassiopeia Simulation of the FSCD Magnetic Trap

The trap developed for the FSCD experiment utilizes six current carrying coils, which surround a cylindrical tritium containment vessel (see Figure 4.1). Some critical aspects of the trap design include the total trapping volume, the maximum trap depth, the

---

<sup>1</sup><https://github.com/KATRIN-Experiment/Kassiopeia>

steepness of the trap walls, as well as the radial and azimuthal uniformity of the magnetic fields.

The volume of the FSCD trap is a cylindrically shaped region with a radius of 5 cm and a length of 15 cm resulting in a roughly 1 L total trap volume. The trap volume is an important design feature, because it sets the volume of the experiment that is potentially usable for CRES measurements. Trapping a larger volume allows one to observe a larger number of tritium atoms, which increases the statistical power and sensitivity of the neutrino mass measurement. Due to the cost of constructing magnets with large and uniform magnetic fields it is important that the trap use as much of the available volume as possible to limit the overall cost of the experiment.

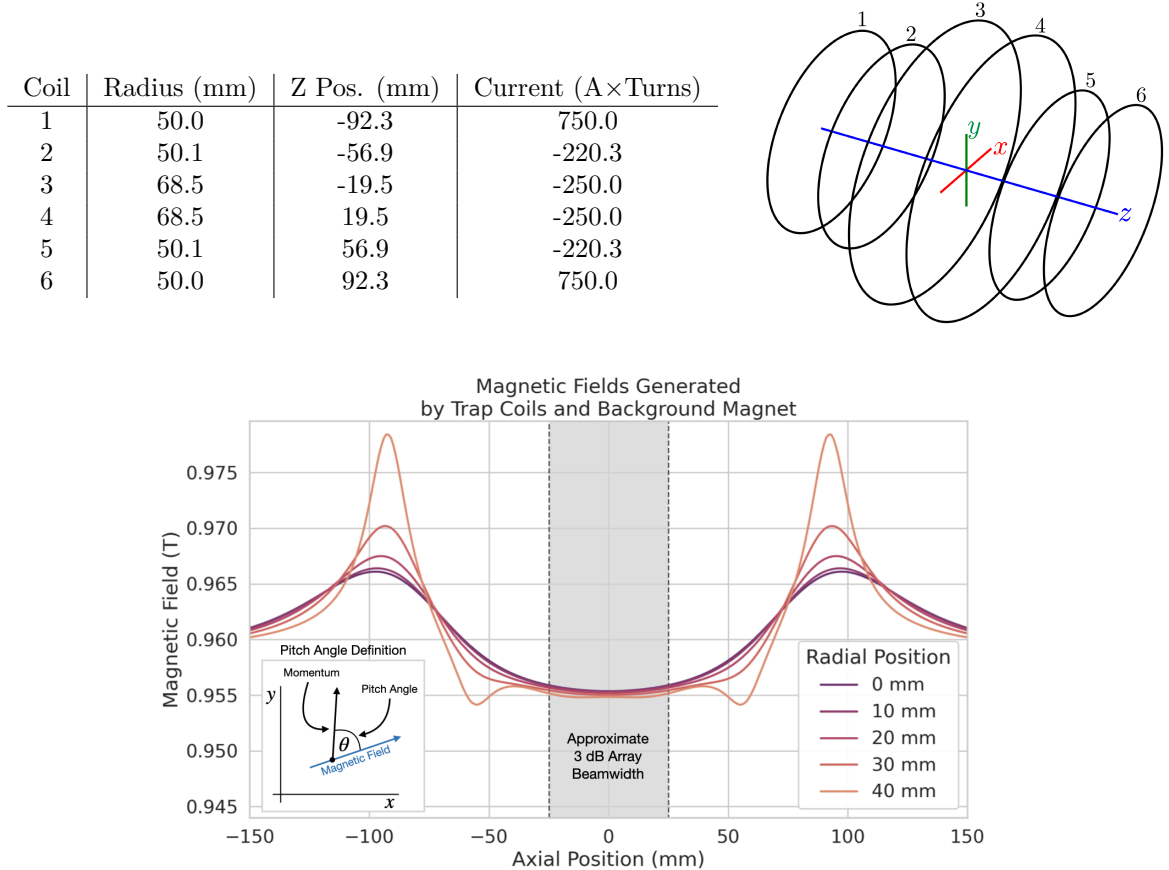


Figure 4.1: The geometry and parameters of the coils used to simulate the FSCD magnetic trap in Kassiopeia. Some axial profiles of the magnetic trap at different radial positions are shown to demonstrate the shape of the magnetic field and trap depth as a function of position.

The depth of the FSCD trap is approximately 10 mT when measured along the central axis of the trap, which is sufficient to trap electrons with pitch angles as small as  $84^\circ$ .

The total trap depth factors into the total efficiency of the experiment by controlling the range of electron pitch angles that can be trapped. If a higher fraction of pitch angles can be trapped then, in principle, more decay events can be observed. However, the signals from electrons with small pitch angles are typically significantly harder to detect than larger pitch angles, which increases the likelihood of not detecting the first track of the CRES event harming the energy resolution of the experiment.

The steepness of the trap walls as well as any non-uniformities in the magnetic field both contribute to the total energy resolution of the CRES measurement by causing uncertainty in the relationship between an electron's kinetic energy and it's cyclotron frequency. When an electron is trapped, it oscillates back and forth along the trap z-axis (see Figure 4.1) unless it is produced with a pitch angle of exactly 90°. As the electron is reflected from the trap walls it experiences a change in the total magnetic field, which causes a modulation in the cyclotron frequency in addition to the expected Doppler modulation. This change in magnetic field from the trap wall introduces a correlation between the pitch angle and kinetic energy parameters of the electron that can reduce energy resolution. In order to mitigate this effect as much as possible it is important to make the trap walls as steep as possible.

## Particle Trajectory Solutions

The magnetic fields solved by direct integration of the current densities can be used by Kassiopeia to solve for the trajectory of electrons based on user specified initial conditions. Various distributions are available within Kassiopeia that can be sampled in order to replicate realistic event statistics, including uniform, Gaussian, and Lorentzian among others. In general, an electron has six kinematic parameters that define its trajectory, which are the three-dimensional coordinates of the initial position and the three components of the electron's momentum vector. However, when simulating CRES events it is more common to parameterize the electron's trajectory in terms of it's initial position, the kinetic energy, the pitch angle, and the initial direction of the component of the electron's momentum perpendicular to the magnetic field. This parameterization is completely equivalent to specify each component of the electrons initial position and momentum vectors.

With the initial parameters of the electron and the magnetic field, Kassiopeia can solve for the trajectory of the electron. The direct approach proceeds by solving the motion of the electron using the Lorentz force equation, which takes the form a set of

differential equations

$$\frac{d\mathbf{r}}{dt} = \frac{\mathbf{p}}{\gamma m} \quad (4.6)$$

$$\frac{d\mathbf{p}}{dt} = e(\mathbf{E} + \frac{\mathbf{p} \times \mathbf{B}}{\gamma m}), \quad (4.7)$$

where  $\mathbf{r}$  is the position of the electron,  $\mathbf{p}$  is the electron's momentum,  $e$  is the charge of the electron,  $m$  is the electron's mass, and  $\gamma$  is the relativistic Lorentz term. To account for kinetic energy losses from radiation Kassiopeia includes an additional term in the momentum differential equation, which calculates the change in the electron's momentum induced by synchrotron radiation. Kassiopeia solves this pair of differential equations using numerical integration, however, the exact trajectory can be computationally intensive to solve. If the adiabatic approximation can be applied, then Kassiopeia can make use of a simpler set of equations that can be more readily solved numerically.

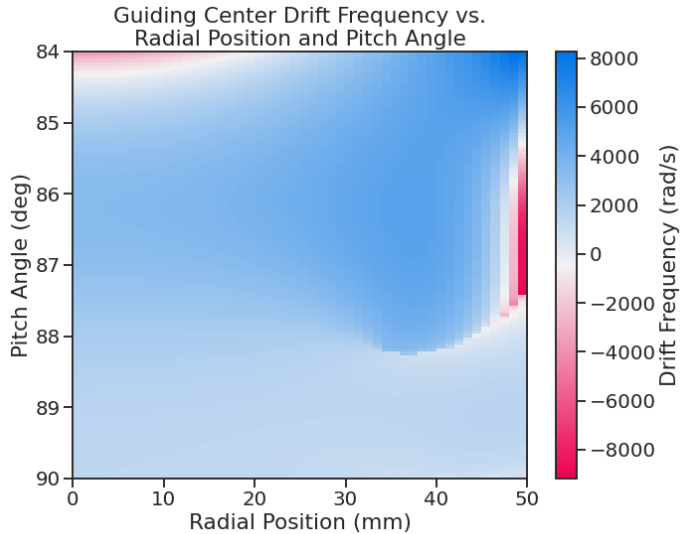


Figure 4.2: A map of the average  $\nabla B$ -drift frequency for electrons trapped in the prototype FSCD trap shown in Figure 4.1. Negative drift frequencies indicate electrons that are drifting opposite to the standard direction, which means that they are close to escaping the magnetic trap.

Even though Kassiopeia is not directly capable of simulating the cyclotron radiation, it is still an invaluable CRES simulation tool, due to the accurate trajectory solutions for electrons in magnetic traps. With Kassiopeia it is possible to test the efficiency of a particular trap design and analyze features of the electron trajectories that are important to the position, track, and event reconstruction algorithms (see Section 4.3). One example

of this for the FSCD is the analysis of the average  $\nabla B$ -drift frequency as a function of the electrons radial position and pitch angle in the magnetic trap (see Figure 4.2). Radial gradients in the trap cause the guiding center of the electron to drift around the center of the magnetic trap with an average frequency on the order of  $10^3$  rad/s. This frequency, while slow compared to the length of a typical CRES time-slice, is large enough to cause a significant loss in efficiency of certain signal reconstruction algorithms. Therefore, it is important to model the drift of the electron in the reconstruction algorithm in order to mitigate the effects of this motion on the reconstruction.

### 4.2.2 Locust

The Locust software package is the primary simulation tool developed and used by the Project 8 collaboration. Locust simulates the responses of antennas and receiver electronics chain to rapidly time-varying electric fields using a flexible approach that allows one to choose from a variety of electric field sources and antennas. Similarly, one can simulate the receiver chain using a series of modular generators that include standard signal processing operations such as down-mixing and fast Fourier transforms (FFT). Since the primary focus of this chapter is the application of Locust to analyses of the FSCD, we shall describe only the most relevant aspects of the software rather than provide a comprehensive description.

### Cyclotron Radiation Field Solutions

Simulating CRES events in the FSCD requires that we calculate the electric fields produced by the acceleration of the electron. In the general case this can be a complicated question to answer, due to back-reaction forces on the electron from its own electric fields that occur when the electron is surrounded by conductive material such as a waveguide or cavity. However, in the case of the FSCD it is possible to ignore such effects and approximate the electron as radiating into a free-space environment.

The equations that describe the electromagnetic fields from a relativistic moving point particle are known as the Liénard-Wiechert field equations, which are obtained by differentiating the Liénard-Wiechert potentials. In their full form the Liénard-Wiechert field equations are

$$\mathbf{E} = e \left[ \frac{\hat{n} - \boldsymbol{\beta}}{\gamma^2(1 - \boldsymbol{\beta} \cdot \hat{n})^3 |\mathbf{R}|^2} \right]_{tr} + \frac{e}{c} \left[ \frac{\hat{n} \times [(\hat{n} - \boldsymbol{\beta}) \times \dot{\boldsymbol{\beta}}]}{(1 - \boldsymbol{\beta} \cdot \hat{n})^3 |\mathbf{R}|} \right]_{tr} \quad (4.8)$$

$$\mathbf{B} = [\hat{n} \times \mathbf{E}]_{tr}, \quad (4.9)$$

where  $e$  is the charge of the particle,  $\hat{n}$  is the unit vector pointing from the particle to the position where the fields are calculated,  $\beta$  and  $\dot{\beta}$  are the velocity and acceleration of the particle divided by the speed of light ( $c$ ),  $\mathbf{R}$  is the distance from the particle to the field calculation position, and  $\gamma$  is the relativistic Lorentz term. The subscript  $t_r$  indicates that the equations must be evaluated at the retarded time so that the time-delay from the travel time of the electromagnetic radiation is correctly accounted for.

The only required input to calculate the electric field at the position of an FSCD antenna is the velocity and acceleration of the electron, which can be obtained from Kassiopeia simulations. Therefore, when simulating a CRES event Locust first runs a Kassiopeia simulation of the electron and calculates the electric field incident on the antenna. The only difficulty with this approach is the determination of the retarded time. The retarded time corresponds to the time that a photon, which has just arrived at an antenna at the space-time position  $(t, \mathbf{r})$ , was actually emitted by the electron at the space-time position of  $(t_r, \mathbf{r}_e(t_r))$ . Defined in this way, finding the retarded time requires solving

$$c(t - t_r) = |\mathbf{r} - \mathbf{r}_e(t_r)|, \quad (4.10)$$

where the distance traveled by the photon between the measurement and retarded times is equal to the distance between the antenna and the electron at the retarded time. Locust solves Equation 4.10 using a built-in root finding algorithm to find the retarded time, and thus the electric field produced by the electron at the position of each antenna in the FSCD array.

### Antenna Response Modeling

With the electric field it is possible, in principle, to calculate the resulting voltages produced in the antenna. However, direct simulation of the antenna itself is computationally expensive since it would require the modeling of complex interactions of the electron's electric fields with charge carriers in the conductive elements of the antenna. Direct simulation of the antenna in Locust can be avoided by modeling the antenna response using the antenna factor, or antenna transfer function, approach. The antenna factor defines the voltage produced in the antenna terminal for an incident electric field,

$$A_F = \frac{V}{|\mathbf{E}|}, \quad (4.11)$$

where  $V$  is the voltage and  $|\mathbf{E}|$  is the magnitude of the incident electric field. To obtain the antenna factor for the antennas developed for the FSCD Project 8 employs Ansys HFSS. HFSS is a commercially available finite element method electromagnetic solver widely used throughout the antenna engineering industry. HFSS is capable of calculating the antenna factor and gain patterns for complex antenna designs and outputting the resulting quantities in the form of a text file that can be used as an input to the Locust simulation.

The antenna factor defines the steady-state response of the antenna to electromagnetic plane waves and is a function of the frequency of the radiation. Therefore, in order to apply the transfer function for the calculation of the antenna voltage response in the time domain, Locust models the antenna as a linear time-invariant system. In this formalism the response of the system to the driving force is given by

$$y[n] = h * x = \sum_k h[k]x[n - k], \quad (4.12)$$

where  $y[n]$  is the discretely sampled response,  $x$  is the driving force stimulus, and  $h$  is the finite impulse response (FIR) filter. When applied to the FSCD array, this formalism calculates the voltage time-series produced in each antenna by convolving the electric field time-series with the antenna FIR filter, which is obtained by performing a inverse Fourier transform on the transfer function from HFSS.

## Radio-frequency Receiver and Signal Processing

After obtaining the voltage time-series by computing the electron trajectory and antenna response, Locust simulates the signal processing associated with the radio-frequency receiver chain. The standard receiver chain used in Locust simulations of the FSCD attempts to mimic the operations that would actually occur in hardware (see Figure 4.3).

Frequency down-conversion is used in the FSCD to reduce the digitization bandwidth required to read-out CRES data. According to the Nyquist sampling theorem, the minimal sampling rate that guarantees no information loss for a signal with a bandwidth  $\Delta f$  is given by

$$f_{\text{Nyq}} = 2\Delta f. \quad (4.13)$$

The total bandwidth of CRES signal frequencies from tritium beta-decay ranges from 0 to 26 GHz in a 0.95 T magnetic field, therefore, direct digitization of CRES signals from the FSCD would require sampling frequencies greater than 50 GHz, which is infeasible for

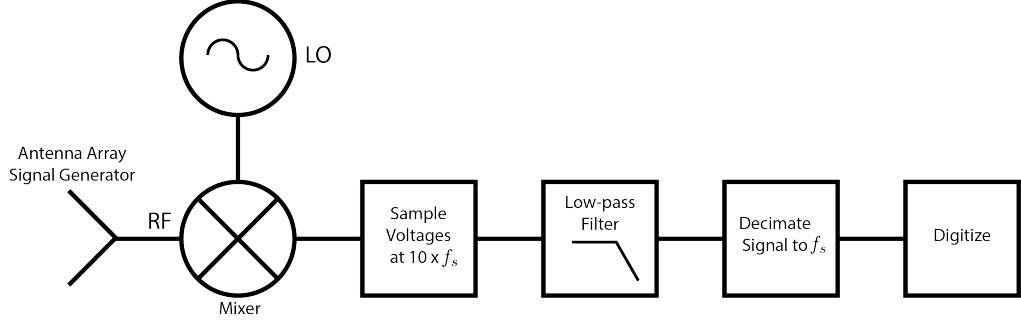


Figure 4.3: The receiver chain used by Locust when simulating CRES events in the FSCD.

a real experiment. However, for the purposes of neutrino mass measurement we are only interested in measuring the shape of the spectrum in the last 100 eV, which corresponds to a frequency bandwidth of 5 MHz. Down-conversion is a technique for reducing the base frequencies of signals in a bandwidth given by  $[f_{\text{LO}}, f_{\text{LO}} + \Delta f]$  to the bandwidth  $[0, \Delta f]$ , by performing the following multiplication

$$x(t) \rightarrow x(t)e^{-2\pi f_{\text{LO}} t}. \quad (4.14)$$

In down-conversion the signal ( $x(t)$ ) is multiplied by a sinusoidal signal with frequency  $f_{\text{LO}}$  to reduce the absolute frequencies of the signals in the bandwidth. In the FSCD this allows us to detect events in the last 100 eV of the tritium spectrum while sampling the data far below 50 GHz. The standard bandwidth used in the FSCD is 200 MHz, which allows for higher frequency resolution than the minimum sampling frequency for 100 eV of energy bandwidth.

Trying to directly simulate down-conversion with a frequency multiplication in Locust would require the sampling of the electric fields at each antenna in the FSCD array with a period of  $\approx 20$  ps, which is extremely slow computationally. To avoid this Locust performs the down-conversion by intentionally under-sampling the electric fields with a frequency of 2 GHz. Sampling below the Nyquist limit causes the higher frequency components of the CRES signal to alias, however, Locust can remove these aliased frequency peaks using a combination of low-pass filtering and decimation to recreate frequency down-conversion. After filtering and decimation, Locust simulates digitization by an 8-bit digitizer at a sampling frequency of 200 MHz to recreate the conditions of the FSCD. The voltage offset and the digitizer range must be configured by the user based on the characteristics of the simulation.

## Data

The output of Locust simulations for the FSCD primarily consists of two data files. The first is the electron trajectory information calculated by Kassiopiea, which is output in the form of a `.root` file. This file contains important kinematic information about the electron such as its position and pitch angle as a function of time. The other file is produced by Locust and it contains the digitized signals acquired from each antenna in the FSCD array. The Locust output files conform to the Monarch specification developed by Project 8, which is based on the commonly used HDF5 file format, and matches the format of the files produced by the Project 8 data acquisition software. This makes it possible to use the same data analysis code to analyze both simulated and real data.

### 4.2.3 CREsana

Locust is the primary simulation tool used by Project 8 in the development and simulation of the FSCD and antenna array CRES more broadly. However, simulations of CRES events in larger antenna arrays ( $\geq 100$  antennas) using Locust can take several hours to complete, which is prohibitively long when one is performing a sensitivity analysis for a large scale antenna experiment. One of the reasons for Locust's slow operation is that the electric fields from the electron must be solved numerically for each time-step for each of the antennas in the array. These numerical solutions allow Locust to accurately simulate the electric fields from arbitrarily complicated electron trajectories at the cost of more computations and slower simulations. Therefore, an additional simulation tool that sacrifices some accuracy for computational efficiency would be extremely useful simulations and sensitivity analyses of larger antenna array experiments.

To fill this need, Project has developed a new simulations package called CREsana, specifically designed to perform analytical simulations of antenna array based CRES experiments. CREsana is not as flexible as Locust, but it provides a significant increase in simulation speed. It does this by using well-justified analytical approximations of the electrons motion in the magnetic field and the resulting electric fields from the electron's acceleration. The electric fields and signals generated by CREsana are consistent with theoretical calculations of the electron's radiation, and are test for accuracy using well-known test-case simulations and consistency checks.

## 4.3 Signal Detection and Reconstruction Techniques for Antenna Array CRES

### Antenna Array CRES Signal Reconstruction

A robust set of FSCD simulation tools are vital to the development of the analysis algorithms necessary for antenna array CRES to succeed. In order to perform CRES measurements using an antenna array one must develop an algorithm that uses the multi-channel time-series obtained by digitizing the array to estimate the starting kinetic energies of electrons produced in the magnetic trap. This procedure consists of a multi-stage process of detecting a CRES signal then estimating the parameters of the electron that produced and is often referred to as simply CRES signal reconstruction.

Compared with the signal reconstruction used in previous CRES experiments by Project 8, the antenna array CRES technology as well as the goals of the FSCD both requires a different approach to signal reconstruction than what was used in the Phase I and Phase II experiments. In the Phase I and II experiments CRES was performed using a waveguide gas cell that could be directly integrated into a waveguide transmission line, which would transmit the cyclotron radiation along its length to an antenna at either end of the waveguide. However, in the case of an antenna array the electron is essentially radiating into free-space and the amount of cyclotron radiation power collected by the array is proportional to the solid angle surrounding the electron that is filled with antennas. Because it is not practical to fully surround the magnetic trap with antennas, some of the cyclotron radiation power that would have been collected by the waveguide escapes into free-space. Furthermore, the power that is collected by the antenna array is split between every channel in the antenna array, which significantly lowers the signal-to-noise ratio (SNR) of CRES signals in a single antenna channel compared to a waveguide apparatus. Therefore, a suite of completely new signal reconstruction techniques are needed in order to perform CRES in the FSCD.

Changes to the approach to CRES signal reconstruction are motivated not only by the switch to a new CRES detector technology, but also by the more ambitious scientific goals of the FSCD experiment. A measurement of the tritium beta-decay spectrum sensitive to neutrino masses as small as 40 meV requires that we measure the kinetic energies of individual electrons with a resolution of 115 meV. This resolution includes all sources of potential uncertainty in the electrons kinetic energy such as magnetic field inhomogeneities and event start time uncertainty. This level of energy resolution is

compatible only with an event-by-event signal reconstruction approach where the kinetic energies, pitch angles, and other parameters of the individual CRES events are estimated before constructing the beta-decay spectrum. This approach is distinct from the analysis done for the Phase I and Phase II experiments where only the starting cyclotron frequency of the event was estimated by analyzing the tracks formed by the carrier frequency in the time-frequency spectrogram. These frequencies were then combined into a frequency spectrogram, which was converted to the beta-decay energy spectrum using an ensemble approach that averaged over all other event parameters. The ensemble approach to signal reconstruction results in poor energy resolution because other kinematic parameters such as pitch angle change the cyclotron carrier frequency due to changes in the average magnetic field experience by the electron, and it is therefore incompatible with the future goals of the Project 8 collaboration.

### Components of Reconstruction: Signal Detection and Parameter Estimation

In developing new signal reconstruction approaches for the FSCD and beyond it is helpful to pose signal reconstruction as a two-step procedure consisting of signal detection followed by parameter estimation. In the former we are only concerned with the identification of the presence of a CRES signal in the data regardless of its specific parameters, whereas, in the latter we always operate under the assumption that a signal is present and attempt figure out it's parameters. More formally, signal detection is essentially a binary hypothesis test between the signal and noise data classes and parameter estimation describes a procedure of fitting a model to the observed data. While both of these processes are required for a complete reconstruction (see Figure 4.4), the focus of my work and this chapter is on the signal detection aspect of antenna array CRES signal reconstruction.

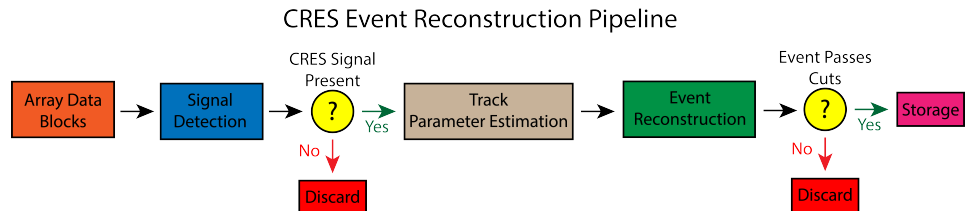


Figure 4.4: A high-level diagram depicting the process of CRES event reconstruction. The first step consists of identifying the presence of a signal in the data. This step is necessary to avoid the danger of performing a reconstruction of a false event, which would constitute a background contribution to the tritium spectrum measured by CRES.

## Detection Theory

The problem of signal detection is equivalent to a statistical hypothesis test. For CRES signals, which are essentially vectors with added WGN, we need to select between two hypotheses

$$\mathcal{H}_0 : \mathbf{y} = \boldsymbol{\nu} \quad (4.15)$$

$$\mathcal{H}_1 : \mathbf{y} = \mathbf{x} + \boldsymbol{\nu}, \quad (4.16)$$

where  $\mathbf{y}$  is the CRES data vector,  $\boldsymbol{\nu}$  is a sample of WGN, and  $\mathbf{x}$  represents the CRES signal. We label the hypothesis that the data contains only noise  $\mathcal{H}_0$  and the hypothesis that the data contains signal  $\mathcal{H}_1$ .

To visualize this procedure we examine the case where we attempt to distinguish between  $\mathcal{H}_0$  and  $\mathcal{H}_1$  using only the first sample of data. The likelihood of choosing either hypothesis is given by the area underneath the probability distribution curve. A true positive corresponds to correctly identifying that the data contains signal, whereas, a true negative means that we have correctly identified the data as noise. The rate at which the detector performs a true positive classification is given by the green region underneath  $p(\mathbf{y}[0]; \mathcal{H}_0)$ , and the rate at which the detector performs a true negative classification is given by the orange region underneath  $p(\mathbf{y}[0]; \mathcal{H}_1)$  (see Figure 4.5). Two types of misclassifications are possible. Either we declare noise data as signal, which is called a false positive, or we declare signal data as noise, which is a false negative. Note that it is only possible to trade off these two types of errors by tuning the detection threshold. One cannot simultaneously reduce the rate of false positives without also increasing the rate of false negatives.

The approach we take with CRES signals is to fix the rate of false positives by setting a minimum value for a detection threshold. The rate of false positives that is acceptable at the detection stage depends upon the rate of background events compatible with the sensitivity goals of the experiment. The ultimate goal of a neutrino mass measurement with 40 meV sensitivity in general has strict requirements on the number of background events, which requires a relatively high detection threshold to achieve. Consequently, we are interested in the signal detection algorithm that achieves the maximum rate of true positives for a fixed rate of false positives, so that we can maximize the detection efficiency of the experiment.

According to the Neyman-Pearson theorem, the statistical hypothesis test that maximizes the probability of detection for a fixed rate of false positives is the likelihood

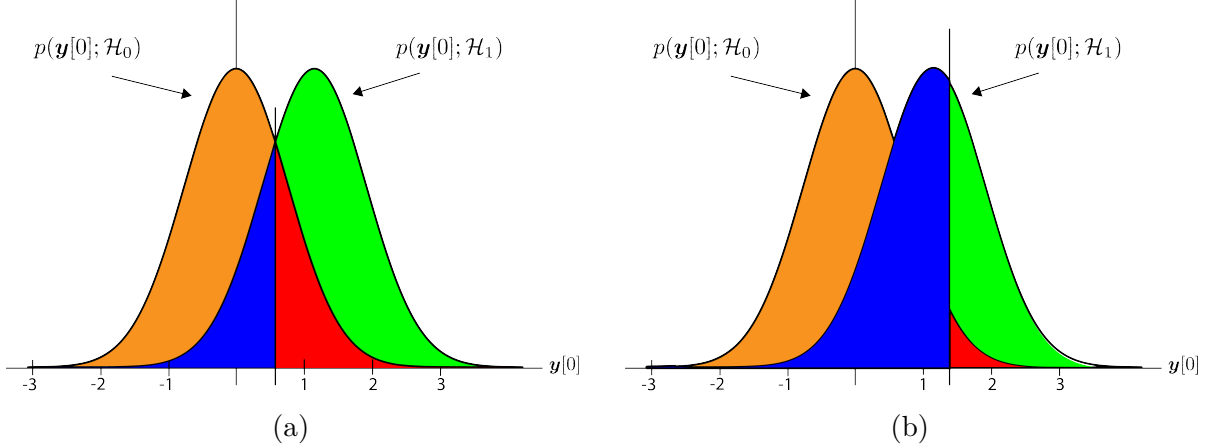


Figure 4.5: An illustration of two PDFs associated with a binary hypothesis test. The decision threshold is represented by the vertical line that partitions both distributions. The orange and red areas correspond to the true negative and false positive probabilities and the blue and green areas correspond to the false negative and true positive probabilities respectively. To decide between the two hypotheses we perform the likelihood ratio test specified by the Neyman-Pearson theorem. This approach achieves the highest true positive probability for a given false positive probability.

ratio test, which is formed by computing the ratio of the signal likelihood to the noise likelihood,

$$L(x) = \frac{P(\mathbf{y}; \mathcal{H}_1)}{P(\mathbf{y}; \mathcal{H}_0)} > \gamma. \quad (4.17)$$

Here, the likelihood of the hypotheses  $\mathcal{H}_0$  and  $\mathcal{H}_1$  are described by the probability distributions  $P(\mathbf{y}; \mathcal{H}_0)$  and  $P(\mathbf{y}; \mathcal{H}_1)$  respectively, and  $\gamma$  is the threshold for deciding  $\mathcal{H}_1$ . The decision threshold is determined by integrating  $P(\mathbf{y}; \mathcal{H}_0)$  such that

$$P_{FP} = \int_{\gamma}^{\infty} P(\tilde{\mathbf{y}}; \mathcal{H}_0) d\tilde{\mathbf{y}} = \alpha, \quad (4.18)$$

where  $\alpha$  is the desired false positive detection rate given by the red colored areas shown in Figure 4.5. The true positive detection rate is given by the similar integral

$$P_{TP} = \int_{\gamma}^{\infty} P(\tilde{\mathbf{y}}; \mathcal{H}_1) d\tilde{\mathbf{y}}, \quad (4.19)$$

which corresponds to the green areas in Figure 4.5.

Changing the decision threshold allows us to trade-off between  $P_{TP}$  and  $P_{FP}$  as appropriate for the given situation. It is common to summarize the relationship between  $P_{TP}$  and  $P_{FP}$  using the receiver operating characteristic (ROC) curve, which is obtained

by evaluating the true positive and false positive probabilities as a function of the decision threshold value (see Figure 4.6). The ROC curve provides a convenient way to compare

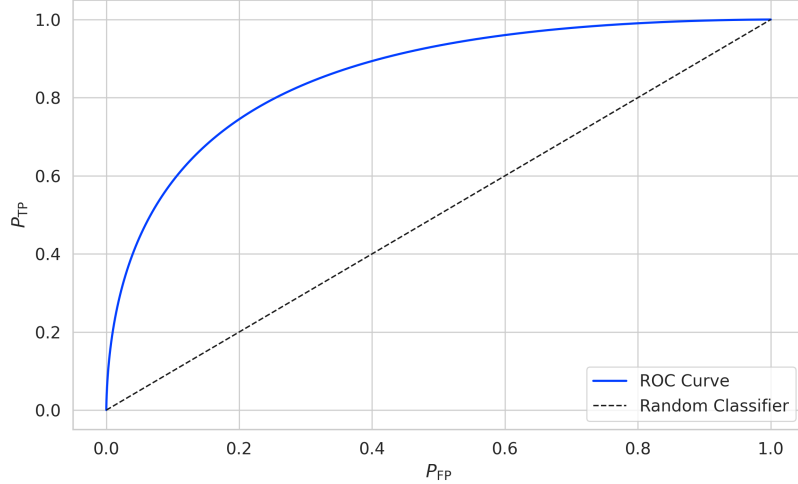


Figure 4.6: An example ROC curve formed by computing the  $P_{\text{FP}}$  and the  $P_{\text{TP}}$  for a given likelihood ratio test. As the decision threshold is increased  $P_{\text{FP}}$  decreases at the expense of a lower  $P_{\text{TP}}$ . The black dashed line indicates the lower bound ROC curve obtained by randomly deciding between  $\mathcal{H}_0$  and  $\mathcal{H}_1$ .

the performance of different signal detection algorithms. In general, a classifier with a higher the  $P_{\text{TP}}$  as a function of  $P_{\text{FP}}$  is desirable, which corresponds to a larger area underneath the respective ROC curve. A perfect classifier has an area underneath the curve of 1.0, however, such a classifier is never achievable in practice.

### 4.3.1 Digital Beamforming

#### Introduction to Beamforming

Beamforming refers to a suite of antenna array signal processing techniques that are designed to enhance the radiation or gain of the array in certain directions and suppress it in other directions. Beamforming is of interest to Project 8 as a first level of signal reconstruction for the FSCD and other antenna array CRES experiments, which operates at the signal detection stage of reconstruction. This is because beamforming is designed to combine the outputs of the different antennas in the array into a single signal, that could be analyzed in a similar way as previous CRES experiments to start and provide the basis for the development of new follow-up analysis algorithms.

At a basic level beamforming is accomplished by performing a phased summation

of the signals received by the antenna array. The beamforming phases are chosen such that the signals emitted by the array in the transmit mode will constructively interfere at the point of interest (see Figure 4.7). As a consequence of the reciprocal theorem, therefore, when the array is operating in the receive mode signals emitted from a source at the same point will constructively interfere when they are summed. The origin of

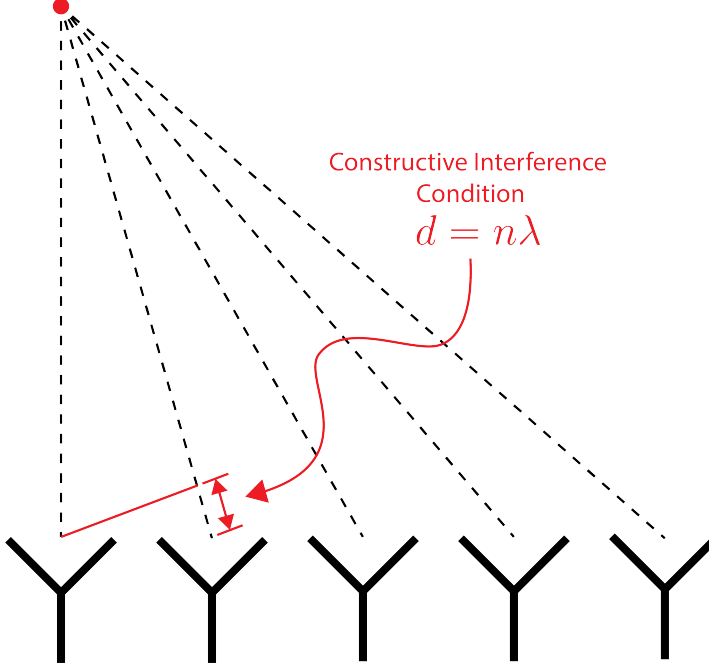


Figure 4.7: An illustration of the constructive interference condition which is the operating principle of digital beamforming using a uniform linear array as an example.

the phase delays in beamforming is the path-length difference to the beamforming point between different antennas in the array. The relationship between the phase delay and the path-length difference is given by the familiar equation

$$\phi = \frac{2\pi d}{\lambda}, \quad (4.20)$$

where  $\phi$  is the phase delay,  $d$  is the path-length difference, and  $\lambda$  is the wavelength of the radiation. In practice, one chooses the values of  $d$  by specifying the beamforming positions of interest and then calculates the beamforming phases using Equation 4.20, which is guaranteed to follow the constructive interference condition shown in Figure 4.7.

Beamforming can be neatly expressed mathematically using the vector equation

$$y[n] = \Phi^T[n] \mathbf{x}[n], \quad (4.21)$$

where  $\mathbf{x}[n]$  is the array snapshot vector,  $\Phi[n]$  is a vector of beamforming shifts, and  $y[n]$  is the resulting summed signal. The beamforming shifts consist of a set of complex numbers that contain the beamforming phase shift and an amplitude weighting factor,

$$\Phi[n] = [A_0[n]e^{-2\pi i \phi_0[n]}, A_1[n]e^{-2\pi i \phi_1[n]}, \dots, A_{N-1}[n]e^{-2\pi i \phi_{N-1}[n]}], \quad (4.22)$$

where the set of magnitudes  $A_i[n]$  are amplitude weighting factors and  $\phi_i[n]$  are the phase shifts from the path-length differences. The index  $i$  is used to denote the antenna channel number. The amplitude weighting factor is the relative magnitude of the signal received by a particular antenna to the other antennas in the array, such that the antennas that receive signals with higher amplitude, due to being closer to the source, have more weight in the beamforming summation. The input and outputs signals beamforming are naturally expected to be functions of time as indicated by the index  $[n]$ , however, it is also possible to use time dependent beamforming phases that shift the beamforming position of the array over time.

The name digital beamforming refers to a specific type of beamforming algorithm that is of interest to Project 8 for CRES applications. Specifying digital beamforming means that the beamforming phases are applied to the array signals in software rather than employing fixed beamforming phase shifts in the receiver chain hardware. The advantage of digital beamforming is that for a given series of array snapshots one can specify a large number of beamforming positions and effectively search for electrons by performing the beamforming summation associated with each point and applying a signal detection algorithm to identify the presence of a CRES signal.

One of the most attractive features of digital beamforming is the spatial filtering effect, which is a direct consequence of the constructive interference condition used to define the beamforming phases. Spatial filtering allows for signals from multiple electrons at different positions in the trap to be effectively separated, because the constructive interference condition will force the signals from electrons at positions different from the beamforming position to cancel. This helps to reduce signal pile-up that could become an issue for large scale CRES experiments using a dense tritium source.

The digital beamforming positions can be specified with arbitrary densities limited only by the available computational resources. This provides a very straight-forward way to estimate the position of the electron in the trap by using a dense grid of beamforming positions and maximizing the output power of the beamforming summation over this grid. This natural approach to position reconstruction is attractive due the requirements

of an event-by-event signal reconstruction, which needs an accurate estimation of the exact magnetic field experienced by the electron in order to correctly estimate its kinetic energy. Combined with an accurate map of the magnetic field inhomogeneities of the trap obtained from calibrations, beamforming allows us to apply this magnetic field correction with a spatial resolution that is a fraction of the cyclotron wavelength.

### FSCD Beamforming Simulations

Using Locust simulations of the FSCD we can perform beamforming reconstruction studies using the simulated CRES signal data. As we mentioned in the previous section, the beamforming procedure begins by specifying a set of beamforming positions and corresponding beamforming shifts. In practice these beamforming positions form a grid that covers the region of interest in the field of view of the antenna array and we perform the beamforming summation using each of these grid positions. There are effectively an infinite number of ways to specify the grid positions, however, uniform square grids are the most commonly used due to their simplicity. In a real FSCD experiment the number and pattern of the grid positions would be optimized to cover the most important regions of the magnetic trapping volume to maximize detection efficiency while minimizing superfluous calculations.

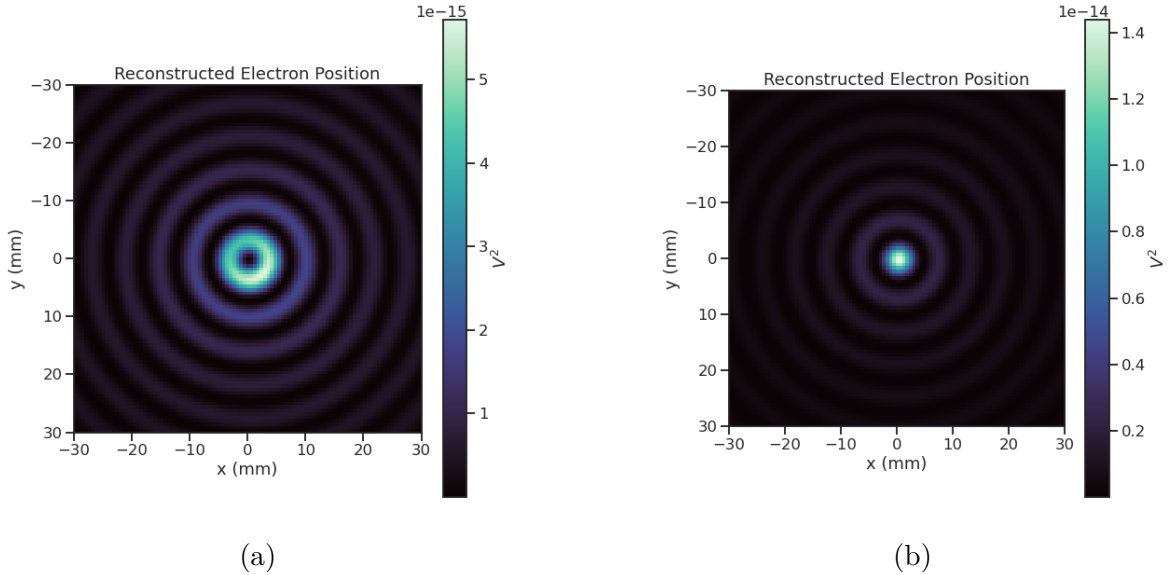


Figure 4.8: Beamforming images visualizing the reconstruction of an electron without (a) and with (b) the cyclotron phase correction.

The beamforming grids used for signal reconstruction with the FSCD consist of a

set of points that cover a region of the two-dimensional plane formed by the perimeter of the antenna array. The axial dimension is left out of the beamforming grid because the electrons are assumed to occupy only an average axial position, which corresponds to the center of the magnetic trap. This is because we are unable to resolve the axial position of the electron as a function of time due to the rapid axial oscillation frequencies of trapped electrons relative to the FSCD time-slice duration.

After beamforming, we obtain for each grid position a summed time-series that can be evaluated for the presence of a signal using a signal detection algorithm. We can visualize this process by arranging the beamforming grid points according to their physical locations to form a three-dimensional matrix where the first two dimensions encode the XY-position of the beamforming point and the third dimension contains the summed time-series. We can then obtain a two-dimensional beamforming image by taking the time-averaged power (see Figure 4.8). We emphasize that the formation of the beamforming image is purely for the purposes of visualization and is not particularly useful for signal detection or reconstruction.

If the beamforming phases consist only of the spatial phase component from Equation 4.20, then the resulting beamforming image contains a relatively high-power ring-shaped region that is centered on the position of the electron (see Figure 4.8a). The origin of this shape is an additional phase offset particular to a cyclotron radiation source. Essentially, the circular motion that produces the cyclotron radiation introduces a relative phase offset to the electric fields that is equal to the azimuthal position of the antenna or field measurement point. For example, if we have two antennas, one located at an azimuthal position of  $0^\circ$  and another located at an azimuthal position of  $90^\circ$ , then the CRES signals received by these antennas will be out of phase by  $90^\circ$ , which is the difference in their azimuthal positions. We can correct for this phase offset by adding an additional term to the beamforming phase equation that is equal to the azimuthal position of the antenna relative to the electron,

$$\phi_i[n] = \frac{2\pi d_i[n]}{\lambda} + \Delta\varphi_i[n], \quad (4.23)$$

where  $\Delta\varphi_i$  is difference between the azimuthal position of the electron and the  $i$ -th antenna channel. Using the updated beamforming phases in the summation changes the ring feature into a Bessel function peak whose maximum corresponds to the position of the electron. Including this cyclotron phase correction significantly improves the signal detection and reconstruction capabilities of beamforming by more than doubling the summed signal power and shrinking the beamforming maxima feature size.

The beamforming image examples in Figure 4.8 were produced using an electron

located on the central axis of the magnetic trap, which do not experience  $\nabla B$ -drift. However, for electrons produced at non-zero radial position the beamforming phases must be made time-dependent in order to track the position of the electron's guiding center over time. Without this correction the  $\nabla B$ -drift causes the electron to move between beamforming positions, which effectively spreads the cyclotron radiation power over a wider area in the beamforming image (see Figure 4.9). This effect significantly

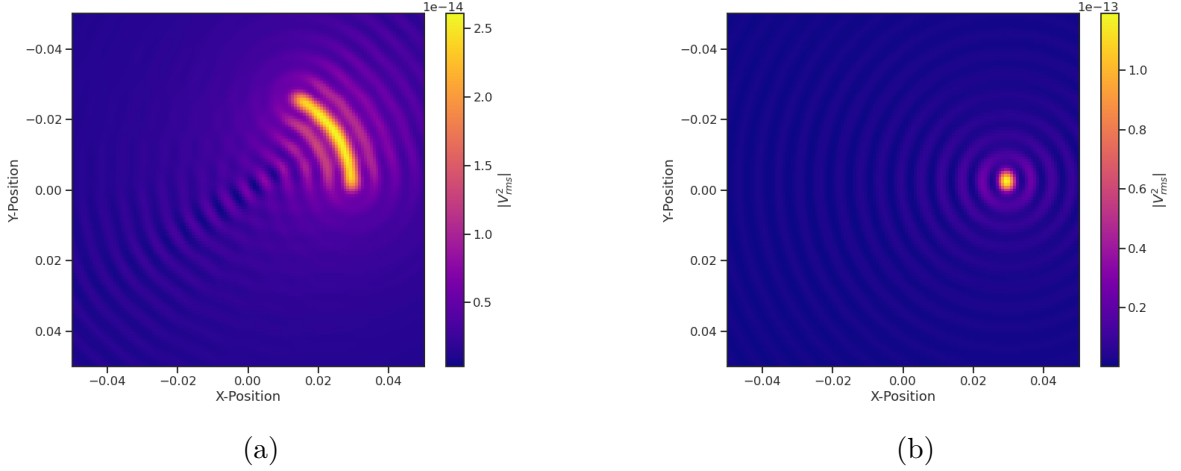


Figure 4.9: Beamforming images visualizing the reconstruction of an electron located off the central axis of the FSCD trap. In (a) we performing beamforming without the  $\nabla B$ -drift correction, and in (b) we include the  $\nabla B$ -drift correction.

reduces the power of the beamforming maxima and increases the size of the beamforming features, simultaneously harming detection efficiency and position reconstruction.

The  $\nabla B$ -drift correction simply adds a circular time-dependence to the beamforming positions as a function of time,

$$r[n] = r_0 \quad (4.24)$$

$$\varphi[n] = \varphi_0 + \omega_{\nabla B} t[n], \quad (4.25)$$

where  $\omega_{\nabla B}$  is the drift frequency and  $t[n]$  is the time vector. In the ideal case the  $\nabla B$ -drift frequencies from Figure 4.2 for the correct pitch angle and radial position would be used, however, it is not possible to know the electron's pitch angle a priori. In principle, one could perform multiple beamforming summations for a given beamforming position using different drift frequencies and choose the one that maximizes the summed power, but this approach leads to a huge computational burden that would be impractical for a real FSCD experiment. A compromise is to use an average value of  $\omega_{\nabla B}$  obtained by

averaging over the drift frequencies for electrons of different pitch angle at a particular radius. This approach keeps the computational cost of time-dependent beamforming to a minimum while still providing a significant increase in the detection efficiency of digital beamforming.

### Signal Detection with Beamforming and a Power Threshold

Up to this point we have neglected any specific discussion of how digital beamforming is used for signal detection and reconstruction. This is because, strictly speaking, digital beamforming consists only of the phased summation of the array signals and cannot be used alone for signal detection. The example beamforming images shown in Figures 4.8 and 4.9 were produced using simulated data that contained no noise, which significantly degrades the utility of analyzing the beamforming images for signal detection and reconstruction.

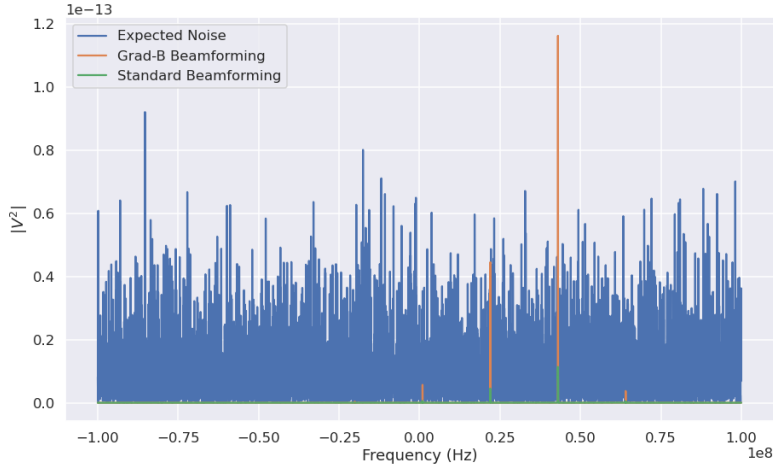


Figure 4.10: A plot of a typical frequency spectrum obtained by applying a Fourier transform to the time-series obtained from beamforming. The frequency spectra are plotted without noise on top of an example of a typical noise spectrum to visualize a realistic signal-to-noise ratio. In the example we see that without beamforming it would not be possible to detect anything since the signal amplitudes would be reduced by a factor of sixty relative to the noise. Additionally, we see that the  $\nabla B$ -drift correction is needed to detect this electron since it comes from a simulation of an electron with a significant off-axis position.

When discussing digital beamforming as a detection algorithm for antenna array CRES this is generally understood within Project 8 to mean digital beamforming plus a detection threshold placed on the amplitude of the frequency spectrum obtained by

applying a fast Fourier transform (FFT) to the summed time-series (see Figure ??). This approach is most similar to the time-frequency spectrogram analysis employed in previous CRES experiments, however, in principle any signal detection algorithm could be used after the beamforming procedure. In Section 4.4 we analyze the signal detection performance of the power threshold approach in detail.

From the example frequency spectra in Figure 4.10 it is clear that without a reconstruction technique that coherently combines the signals from the full antenna our ability to detect CRES signals will be drastically reduced. Because the CRES signals are in-phase at the correct beamforming position the summed power increases as a function of  $N^2$  compared to a single antenna channel, where  $N$  is the number of antennas. It is true that the noise power is also increased by beamforming, but, because the noise is incoherent, its power only increases linearly. Consequently the signal-to-noise ratio of the CRES signal increases linearly with the number of antennas, which greatly improves detection efficiency compared to using only the information in a single antenna.

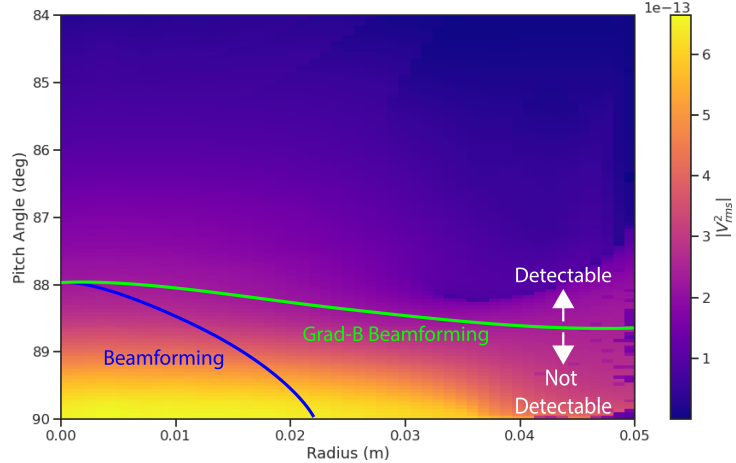


Figure 4.11: A plot of the total signal power received by the FSCD array from trapped electrons with different radial positions and pitch angles generated using Locust simulations. The lines on the plot indicate a 10 dB detection threshold above the mean value of the noise in the frequency spectrum. With static beamforming electrons with radial positions larger than about two centimeters are undetectable due to the change in the electron's position over time causing losses from beamforming phase mismatch. This is corrected by including  $\nabla B$ -drift frequencies in the beamforming phases. Both beamforming techniques fail to detect electrons below  $\approx 88.0^\circ$ , since these signal are composed of several relatively weak sidebands that are comparable to the noise.

The power threshold detection algorithm searches for high-power frequency bins that should correspond to a frequency component of the CRES signal. In order to prevent

random noise fluctuations from being mistaken as CRES signals we need to set our power threshold high enough so that it is highly unlikely that random noise could be responsible. A consequence of this is that many electrons that can be trapped will go undetected because the modulation caused by axial oscillations leads to the cyclotron carrier power to falling below the decision threshold. The time-dependent beamforming used to correct for the  $\nabla B$ -drift increases the volume of the magnetic trap where we are able to detect electrons, but is ineffective at increasing the range of detectable pitch angles (see Figure 4.11). Fundamentally, this is because the power threshold only uses a fraction of the signal power to detect electrons and ignores the power present in the frequency sidebands. In the subsequent sections we examine two other signal detection algorithms that seek to improve the detection efficiency of the FSCD by utilizing the more of the signal shape to compute the detection test statistics.

### 4.3.2 Matched Filtering

#### Introduction to Matched Filtering

The problem of CRES signal detection is the problem of detecting a signal in the presence of white Gaussian noise (WGN), which has been examined at great depth in the signal processing literature. For a fully known signal in WGN it is known that the optimal detector is the matched filter. In this context the optimal detector is the one that achieves the highest true positive rate for a fixed rate of false positives. The matched filter test statistic is calculated by taking the inner product of the data with the matched filter template

$$\mathcal{T} = \left| \sum_n h^\dagger[n] y[n] \right|, \quad (4.26)$$

where  $h[n]$  is the matched filter template and  $y[n]$  is the data. The matched filter test statistic defines a binary hypothesis test in which the data vector is assumed to be an instance of two possible data classes. By setting a decision threshold on the value of  $\mathcal{T}$ , we can classify a given data vector as belonging to two distinct hypotheses. Under the first hypothesis the data is composed of pure WGN, and under the second hypothesis the data is composed of the known signal with additive WGN. The matched filter template is obtained by rescaling the known signal in the following way

$$h[n] = \frac{x[n]}{\sqrt{\tau \sum_n x^\dagger[n] x[n]}}, \quad (4.27)$$

where  $\tau$  is the variance of the WGN and  $x[n]$  is the known signal. Strictly speaking, Equation 4.27 is only true for noise with a diagonal covariance matrix, however, in the context of the FSCD we are justified in assuming this to be true. Defining the matched filter templates in this way guarantees that the expectation value of  $\mathcal{T}$  is equal to one when the data contains only noise, which is the standard matched filter normalization in the signal processing literature.

Even though the matched filter is usually formulated in terms of a perfectly known signal, it is still possible to apply the matched filter technique given imperfect information about the signal provided that the signal is deterministic. From our discussion of CRES simulation tools for the FSCD (see Section 4.2) we know that the shape of CRES signals are completely determined by the initial parameters of the electron. The random collisions with background gas molecules which cause the formation of signal tracks (see Section ??) are the only stochastic component of the CRES event after the initial beta-decay, therefore, it is possible to develop a matched filter for the detection of CRES signal tracks which are fully determined by the parameters of the electron after the initial beta-decay or subsequent collision events.

The matched filter test statistic for CRES signals is a modified version of Equation 4.26

$$\mathcal{T} = \max_{\mathbf{h}, m} |\mathbf{h} * \mathbf{y}| = \max_{\mathbf{h}, m} \left| \sum_k h^\dagger[k] x[m - k] \right|, \quad (4.28)$$

where the matched filter inner product has been replaced with a convolution operation and a maximization over the template and convolution delay ( $m$ ). Replacing the inner product with a convolution accounts for the fact that the start time of the CRES signal is now an unknown parameter, in addition, we now perform a maximization of the matched filter convolution over a number of different templates. Because the shape of the signal is unknown we are forced to guess a number of different signal shapes to create a template bank with which we can identify unknown signals by performing an exhaustive search.

The template bank approach to matched filtering, while quite powerful, can quickly become computationally intractable. This is especially true in the case of the FSCD because of the large amount of raw data produced by the array that must be analyzed. Specifically, the time-domain convolution specified by Equation 4.28 is particularly computationally intensive and is a major barrier towards the implementation of a matched filter for signal detection in an experiment like the FSCD. This can be avoided by using the convolution theorem to replace the time-domain convolution with an inner product in the frequency domain.

The convolution theorem states that

$$\mathbf{f} * \mathbf{g} = \mathcal{F}^{-1}(\mathbf{F} \cdot \mathbf{G}) \quad (4.29)$$

where  $\mathbf{f}$  and  $\mathbf{g}$  are discretely sampled time-series,  $\mathbf{F}$  and  $\mathbf{G}$  are the respective discrete Fourier transforms, and  $\mathcal{F}^{-1}$  is the inverse discrete Fourier transform operator. The convolution theorem allows us to perform the matched filter convolution by first computing the Fourier transform of the template and data, then performing a point-wise multiplication of the two frequency series, and finally performing the inverse Fourier transform to obtain the convolution output. Because discrete Fourier transforms can be performed extremely efficiently, the convolution theorem is almost always used in lieu of directly computing the convolution.

One thing to note here is that the convolution theorem for discrete sequences shown here, is technically valid only for circular convolutions, which is not directly specified in Equation 4.28. However, because typical CRES track lengths are much longer than the Fourier analysis window and also that the frequency chirp rates are small compared to the time-slice duration, it is relatively safe to use circular convolutions to evaluate matched filter scores for CRES signals, which allows us to apply the convolution theorem to compute matched filter scores using the frequency representation of the data and matched filter template.

### Matched Filter Analysis of the FSCD

The optimality provided by the matched filter makes it a useful algorithm for analysis of CRES experiment designs for sensitivity analyses, since it indicates the best possible detection efficiency achievable by an experiment configuration. The standard approach to performing these studies involves generating a large number of simulated electron signals that span the kinematic parameter space of electrons in the magnetic trap. In general, electrons have six kinematic parameters along with an additional start time parameter.

In order to limit the number of simulations required to evaluate the detection efficiency the standard approach is to fix the starting axial position, starting azimuthal position, starting direction of the perpendicular component of the electron's momentum, and event start time to reduce the parameter space to starting radial position, starting kinetic energy, and starting pitch angle. The fixed variables are true nuisance parameters that do not affect the detection efficiency estimates for the FSCD design, because they manifest as phases which are marginalized during the calculation of the matched filter score.

Across radial position, kinetic energy, and pitch angle we can define a regular grid of parameters and use Locust to simulate the corresponding signals. This grid of simulated signals can be used to estimate the likelihood of detecting signals in the FSCD by using the same set of signals as both the data and templates when evaluating the matched filter scores. The matched filter score specifies the shape of the PDF that defines the detection probability.

### Optimized Matched Filtering Implementation for the FSCD

The biggest practical obstacle to the implementation of a matched filter template bank detection approach is oftentimes the computational cost associated with exhaustively calculating the matched filter scores of the template bank, and the FSCD is no exception in this regard. At a basic level computing a matched filter score requires the convolution of two vectors, which can be performed very efficiently by computers if the convolution theorem and fast Fourier transforms (FFT) are utilized. Furthermore, one can consider applying digital beamforming as a pre-processing step to reduce the dimensionality of the data before the matched filter is applied. In order to understand the relative gain in computational efficiency offered by these optimizations we analyze the total number of floating-point operations (FLOP) of several matched filter implementations in big  $O$  notation that utilize different combinations of optimizations.

A direct implementation of a matched filter as specified by Equation 4.28 involves the convolution of  $N_{\text{ch}}$  signals of length  $N_s$  with template signals of length  $N_t$ . As a uniform metric we shall compare the FLOP of the various matched filter implementations on a per-template basis, since each implementation scales linearly with the number of templates. The direct convolution approach to matched filtering costs

$$O(N_{\text{ch}}) \times O(N_s \times N_t) \quad (4.30)$$

FLOP per-template, whose cost is dominated by the  $O(M \times N)$  convolution operation.

The computational cost of the direct matched filter approach can be significantly reduced by exploiting the convolution theorem and FFT algorithms. If we restrict ourselves to signals and templates that contain equal numbers of samples then the convolution can be calculated by Fourier transforming both vectors, performing the point-wise multiplication, and then performing the inverse Fourier transform to obtain the convolution result. The FFT algorithm is able to compute the Fourier transform utilizing only  $O(N \log N)$  operations compared to  $O(N^2)$  for a naive Fourier transform

implementation. This optimization results in a computational cost per-template of

$$O(N_{\text{ch}}) \times O(N_s \log N_s) \quad (4.31)$$

A typical signal vector in the FSCD contains  $O(10^4)$  samples in which case the FFT reduces the computational cost of the matched filter by a factor of  $O(10^3)$ . This large reduction in computational cost implies that a direct implementation of a matched filter is completely infeasible in the FSCD due to resource constraints.

Rather than relying solely on the matched filter it is tempting to consider using digital beamforming as an initial step in the signal reconstruction for the purposes of data reduction. The primary motivation is to reduce the dimensionality of the data by a factor of  $N_{\text{ch}}$  by combining the array outputs coherently into a single channel. One can view the beamforming operation as a partial matched filter, in the sense that the matched filter convolution contains the beamforming phased summation along with a prediction of the signal shape. By separating beamforming from the signal shape one hopes to reduce the overall computational cost by effectively shrinking the number of templates and reducing the number of operations required to check each one.

The nature of this optimization requires that we account for the number of templates used for pure matched filtering versus the hybrid approach. To first order, the total number of templates at the trigger stage is a product of the number of guesses for each of the electron's parameters

$$N_T = N_E \times N_\theta \times N_r \times N_\varphi, \quad (4.32)$$

where  $N_E$  is the number of kinetic energies,  $N_\theta$  is the number of pitch angles,  $N_r$  is the number of starting radial positions, and  $N_\varphi$  is the number of starting azimuthal positions. The starting axial position and cyclotron motion phase are not necessary to include in the template bank since these parameters manifest themselves as the starting phase of the signal, which is effectively marginalized when using a FFT to compute the matched filter convolution. Therefore, the total number of operations required by a matched filter to detect a signal in a segment of array data is on the order of

$$O(N_T) \times O(N_{\text{ch}}) \times O(N_s \log N_s) \quad (4.33)$$

With the hybrid approach we attempt to remove the spatial parameters from the template bank by using beamforming to combine the array signals into a single channel.

Beamforming explicitly assumes a starting position, which allows us to only use matched filter templates that span the two-dimensional space of kinetic energy and pitch angle. The total computational cost of the hybrid method is directly proportional to the number of beamforming positions. For the time-dependent beamforming defined in Section 4.3.1, the number of beamforming positions is given by

$$N_{\text{BF}} = N_r \times N_\varphi \times N_{\omega_{\nabla B}}, \quad (4.34)$$

where  $N_r$  and  $N_\varphi$  are the same spatial parameters encountered in the pure matched filter template bank and  $N_{\omega_{\nabla B}}$  is the number of  $\nabla B$ -drift frequency assumptions. If a unique drift frequency is used for each pitch angle then the hybrid approach is effectively equivalent to a pure matched filter in the number of operations. The key efficiency gain of the hybrid approach is to exploit the relatively small differences in  $\omega_{\nabla B}$  for electrons of different pitch angles by using only a small number of average drift frequencies.

The total number of operations for the hybrid approach can be expressed as a sum of the operations required by the beamforming and matched filtering steps,

$$O(N_{\text{BF}}) \times O(N_{\text{ch}}N_s) + O(N_{\text{BF}}) \times O(N_E N_\theta) \times O(N_s \log N_s). \quad (4.35)$$

The first product in the sum is the number of operations required by beamforming, which is simply the number of beamforming points times the computational cost of the beamforming matrix multiplication, and the second product is the computational cost of matched filtering the summed signal generated by each beamforming position. To compare this to pure matched filtering we take the ratio of Equations 4.33 and 4.35 to obtain

$$\Gamma_{\text{BFMF}} = \frac{O(N_{\omega_{\nabla B}})}{O(N_E N_\theta) \times O(\log N_s)} + \frac{O(N_{\omega_{\nabla B}})}{O(N_{\text{ch}})}. \quad (4.36)$$

This expression can be simplified by observing that  $O(N_E N_\theta) \times O(\log N_s) \gg O(N_{\text{ch}})$ , which means that the ratio of computational cost for the two methods can be reduced to

$$\Gamma_{\text{BFMF}} \approx \frac{O(N_{\omega_{\nabla B}})}{O(N_{\text{ch}})}. \quad (4.37)$$

If we limit ourselves to a number of estimated drift frequencies of  $O(1)$  then we see that the estimated computational cost reduction of the hybrid approach is of  $O(N_{\text{ch}})$ . This is quite a large reduction considering that the FSCD antenna array contains sixty antennas in the baseline design.

The main drawback of the hybrid approach is that the limited number of allowed

drift frequency guesses can lead to detection efficiency loss due to phase mismatch. The degree of phase error from an incorrect drift frequency is proportional to the length of the array data vector used by the signal detection algorithm. For signals with lengths equal to the baseline FSCD Fourier analysis window of 8192 samples, typical phase errors from using an average versus the exact  $\nabla B$ -drift frequency are on the order of a few percent in terms of the signal energy. This has a relatively small impact on the overall detection efficiency, however, future experiments with antenna array CRES will want to balance optimizations such as these during the design phase to keep experiment costs to a minimum while still achieving scientific goals.

### Kinetic Energy and Pitch Angle Degeneracy

More accurate modeling of a matched filter requires that we consider the effects of mismatched signals and template, since this more accurately reflects the real-world usage of a matched filter where many incorrect templates are convolved with the data until the matching template is found. One way to study this is to use the grid of simulated signals to compute the matched filter scores between mismatched signals and templates and evaluate the matched filter scores under this scenario. What one finds when performing this analysis is that templates for kinetic energies and pitch angles that do not match the underlying signal can have matched filter scores that are indistinguishable from the matched filter score of the correct template (see Figure 4.12 and Figure 4.12).

This degeneracy in matched filter score is the result of correlations between the kinetic energy of the electron and the pitch angle caused by changes in the average magnetic field experienced by an electron for different pitch angles. While in principle helpful for the purposes of signal detection these correlations are unacceptable since they greatly reduce the energy resolution of the experiment by causing electrons with specific kinetic energy to templates across a wide range of energies. It is important to emphasize that this degeneracy cannot be fixed by implementing a different signal reconstruction algorithm. As revealed by the matched filter scores the shapes of the signals for different parameters are identical. Resolving this degeneracy between pitch angle and energy requires the design of a new magnetic trap with steeper walls so that the average magnetic field experienced by an electron is less dependent on pitch angle.

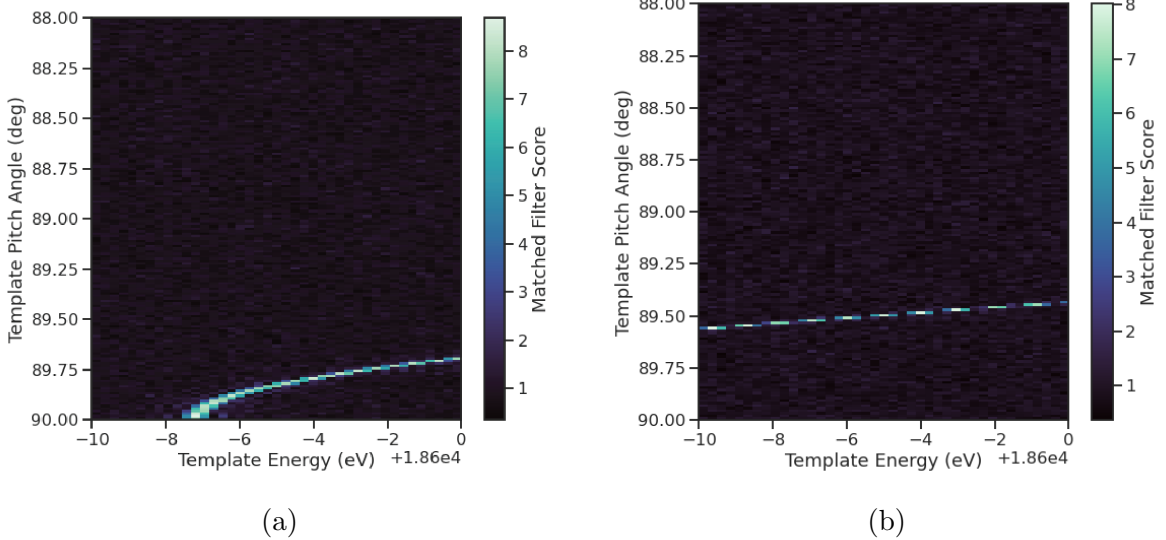


Figure 4.12: Two example illustrations of the correlation between kinetic energy and pitch angle imparted by the shape of the FSCD magnetic trap. The correlations manifest themselves as degeneracies in the matched filter score where multiple matched filter templates have the same matched filter for a particular signal. These degeneracies are a sign that the magnetic trap must be redesigned in order to break the correlation between pitch angle and kinetic energy.

### 4.3.3 Machine Learning

Machine learning is a vast and rapidly developing field of research. In this Section we shall attempt to provided a brief introduction to some of the concepts and techniques of machine learning that were applied to CRES signal detection rather than attempt a comprehensive overview.

#### Introduction to Machine Learning

Digitization of the FSCD antenna array generates large amounts of data that must be rapidly processed to enable real-time signal detection and reconstruction. While digital beamforming combined with a power threshold is relatively computationally inexpensive, it is relatively ineffective at detecting CRES signal with small pitch angles, since it relies on a visible frequency peak above the noise. On the other hand, a matched filter is able to detect signals with a significantly larger range of parameters, however, the exhaustive search of matched filter templates can be computationally expensive. Machine learning based triggering algorithms have been used successfully in many different high-energy physics experiments and recent developments have shown success in the detection

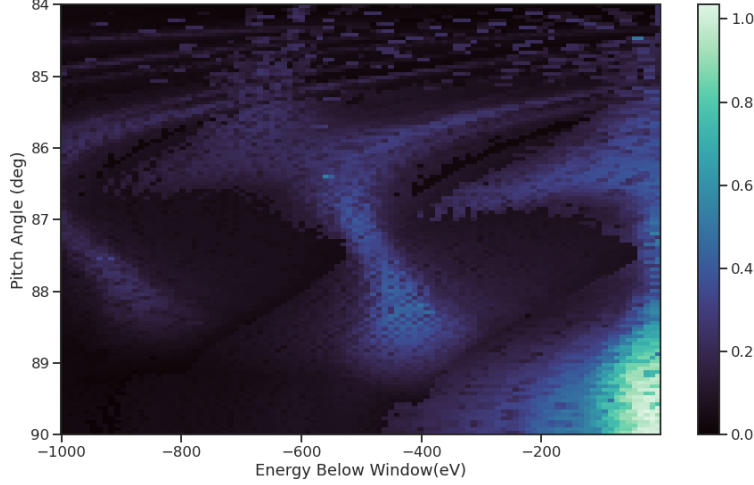


Figure 4.13: A visualization of the correlation between energy and pitch angle in the FSCD magnetic trap. The image is formed by computing the match of the best template from a grid consisting of pitch angles from 84 to 90 degrees in steps of 0.05 degrees, kinetic energies from 17574 to 18574 eV, located at 2 cm from the central axis, and simulated for a length of three FSCD time-slices. The signals used to compute the best matching template consisted of a grid from 84 to 90 degrees in steps of 0.05 degrees, kinetic energies from 18550 to 18575 eV in steps of 0.25 eV, located 2 cm from the central axis, and simulated for three FSCD time-slices. The colored regions of the plot show how well signals with lower energy can match those of higher energy for the FSCD magnetic trap, which is proportional to the achievable energy resolution of the FSCD design.

of gravitational wave signals using machine learning techniques in place of the more traditional matched filtering method. This motivates the exploration of machine learning as a potential CRES signal detection algorithm.

There are several different approaches to machine learning, but the one most important to our discussion here is the supervised learning approach. In supervised machine learning one uses a differentiable model, which is essentially a parameterizable function, that is designed to map the input data to the appropriate label. The data is usually represented as a multidimensional matrix of floating point values such as an image or a time-series in the case of a CRES signal, and the label is usually some class name such as signal or noise for classification problems or a continuous value like kinetic energy in the case of regression problems.

In supervised learning the model is trained to map from the data to the correct label by evaluating the output of the model using a training dataset consisting of a set of paired data and labels. To evaluate the difference between the model output and the correct label a loss function is used to quantify the error between the model prediction

and the ground truth. For example, a common loss function in regression problems is the squared error loss function, which quantifies error using the squared difference between the model output and label.

Using the outputs of the loss function the next step in supervised learning is to compute the gradient of error with respect to the model parameters in a process called backpropogation. Using the model parameter gradients the last step in the supervised learning process is to perform an update of the parameter values in order to minimize the error in the model predictions across the whole dataset. This loop is performed many times while randomly shuffling the dataset until the error converges to a minimum value at which point the training procedure has finished. It is standard practice to monitor the training procedure by evaluating the performance of the model using a separate validation dataset that matches the statistical distribution of the training data and to check the performance of the model after training using yet another dataset called the test dataset. These practices help to guard against overtraining which is a concern for models with many parameters.

## Convolutional Neural Networks

A popular class of machine learning models are neural networks. A neural network is essentially a function composed of a series of linear operations called layers which take a piece of data typically represented as a matrix, multiplies the elements of the data by a weight, and then sums these products to produce an output matrix. Neural networks composed of purely linear operations are unable to model complex non-linear behavior, therefore, non-linear activation functions are applied to the outputs of each of the layers to increase the ability of the neural network to model complex relationships between the data.

Neural networks are typically composed of at least three layers, but with the present capabilities of computer hardware they more often contain many more than this. The first layer in a neural network is called the input layer, because it takes the data objects as input, and the last layer in a neural network is known as the output layer. The output layer is trained by machine learning to map the data to a desired output using the supervised learning procedure described in Section 4.3.3. In between the input and the output layer are typically several hidden layers that receive inputs from and transmit outputs to other layers in the neural network model. The term deep neural network (DNN) refers to those neural networks that have at least one hidden layer, which have proven to be extremely powerful tools for pattern recognition and function approximation.

An important type of DNN are convolutional neural networks (CNN) that typically contain several layers which perform a convolution of the input with a set of filters. These convolution operations are typically accompanied by layers that attempt to down-sample the data along with the standard neural network activation functions. A standard CNN is composed of several convolutional layers at the beginning of the network and ends with a series of fully-connected neural network layers at the output. Intuitively, one can imagine that the convolutional layers are extracting features from the data that fully-connected layers use to perform the classification or regression task.

## Deep Filtering for Signal Detection in the FSCD

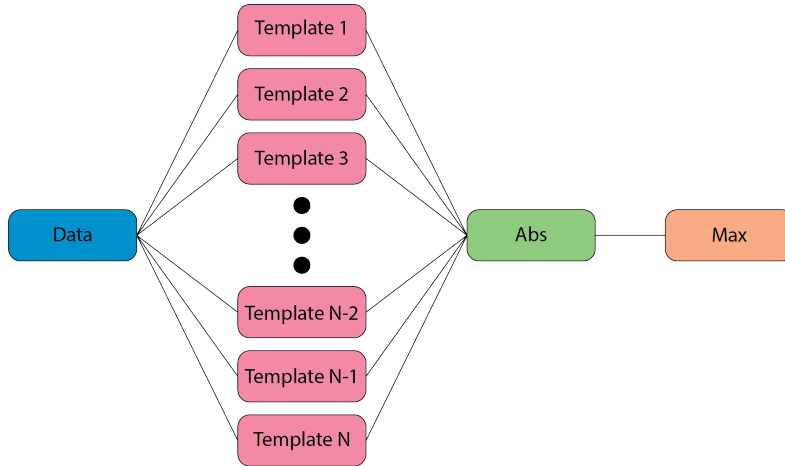


Figure 4.14: A representation of a matched filter template bank as a convolutional neural network. The network has a single layer composed of the templates, which act as convolutional filters. The activation of the neural network is an absolute value followed by a max operator.

CNNs have been extremely influential in the field of computer vision, particularly tasks such as image segmentation and classification, but have also been applied in numerous experimental physics contexts. Given the particular challenge posed by signal detection and reconstruction in the FSCD we are interested in exploring the potential of machine learning as an effective algorithm for real-time signal detection, since this application requires both high efficiency and fast evaluation.

In the machine learning paradigm signal detection is equivalent to a binary classification problem between the signal and noise data classes, and my investigation focuses specifically on the application of CNNs to signal detection in the FSCD, which is motivated by relatively recent demonstrations of CNNs achieving classification accuracies for

gravitational wave time-series signals comparable to a matched filter template bank. In this framework it is possible to interpret the matched filter as a type of CNN composed of a single convolutional layer with the templates making up the layer filters (see Figure 4.14). Since this neural network has no hidden layers, it is not a DNN like we have been discussing so far, but we can attempt to construct a proper CNN that attempts to reproduce the classification performance of the matched filter network.

The name deep filtering refers to this scheme of replacing a matched filter template bank with a DNN. The reason why one might want to do this is that it may be possible to exploit redundancies and correlations between templates that may allow one to perform signal detection with similar accuracy but with fewer computations, which is important for real-time detection scenarios like the FSCD experiment. In Section 4.4 we perform a detailed comparison of the signal detection performance of a CNN to beamforming and a matched filter template bank.

## 4.4 Analysis of Signal Detection Algorithms for the Antenna Array Demonstrator

This section contains an early version of the manuscript for the triggering paper prepared for publication in JINST. In it I present a relatively detailed analysis of the signal detection performance of the three signal detection approaches discussed so far using a population of simulated CRES signals generated with Locust. The focus of the paper is on the performance of the signal detection algorithms for pitch angles below  $88.5^\circ$  where the beamforming power threshold begins to fail.

### 4.4.1 Introduction

Cyclotron Radiation Emission Spectroscopy (CRES) is a technique for measuring the kinetic energies of charged particles by observing the frequency of the cyclotron radiation that is emitted as they travel through a magnetic field [2]. The Project 8 Collaboration is developing the CRES technique as a next-generation approach to tritium beta-decay endpoint spectroscopy for neutrino mass measurement. Recently, Project 8 has used CRES to perform the first ever tritium beta-decay energy spectrum and neutrino mass measurement [3, 4].

Previous CRES measurements have utilized relatively small volumes of gas that are directly integrated with a waveguide transmission line, which transmits the cyclotron

radiation emitted by the trapped electrons to a cryogenic amplifier. While this technology has had demonstrable success, it is not a feasible option for scaling up to significantly larger measurement volumes. In particular, the goal of the Project 8 Collaboration is to use CRES combined with atomic tritium to measure the neutrino mass with a 40 meV sensitivity. Achieving this sensitivity goal will require a multi-cubic-meter scale measurement volume in order to obtain the required event statistics in the tritium beta-spectrum endpoint region; hence, there is a need for new techniques to enable large volume CRES measurements for future experiments.

One approach is to surround a large volume with an array of antennas that together collect the cyclotron radiation emitted by trapped electrons [5,6]. A promising array design is an inward-facing uniform cylindrical array that surrounds the tritium containment volume. Increasing the size of the antenna array, by adding additional rings of antennas along vertical axis, allows one to grow the experimental volume until a sufficient amount of tritium gas can be observed by the array. A challenging aspect of this approach is that the total radiated power emitted by an electron near the tritium spectrum endpoint is on the order of 1 fW or less, which is then distributed between all the antennas in the array. Consequently, detecting the presence of a CRES signal and determining the electron's kinetic energy requires reconstructing the entire antenna array output over the course of the CRES event, posing a significant data acquisition and signal reconstruction challenge.

Project 8 has developed a triggering system to enable real-time identification of CRES events using an antenna array [7]. Previous measurements with the CRES technique have utilized a threshold on the frequency spectrum formed from a segment of CRES time-series data. This algorithm relies on the detection of a frequency peak above the thermal noise background, which limits the kinematic parameter space of detectable electrons. Due to the limitations of this power threshold, Project 8 has been investigating alternative signal identification approaches, including both matched filtering and machine learning based classifiers, to improve the detection efficiency of the experiment. In order to evaluate the relative gains in detection efficiency that come from utilizing these alternative algorithms, we develop analytical models for the power threshold and matched filter signal classifier performance applicable to an antenna array based CRES detector. In addition, we implement and test a basic convolutional neural network (CNN) as a first step towards the development of neural-network based classifiers for CRES measurements. These results allow us to compare the estimated detection efficiencies of each of these methods, which we weigh against the associated computational costs for

real-time applications.

The outline of this paper is as follows. In Section 4.4.2 we give an overview of a prototypical antenna array CRES experiment, and describe the major steps involved in the proposed approach to real-time signal identification. In Section 4.4.3 we develop models for the power threshold and matched filter algorithms, and introduce the machine learning approach and CNN architecture. In Section 4.4.4 we describe our process for generating simulated CRES signal data and the details of training the CNN. Finally, in Section 4.4.5 we perform a comparison of the signal classification accuracy of the three approaches and discuss the relevant trade-offs in terms of detection efficiency and computational cost.

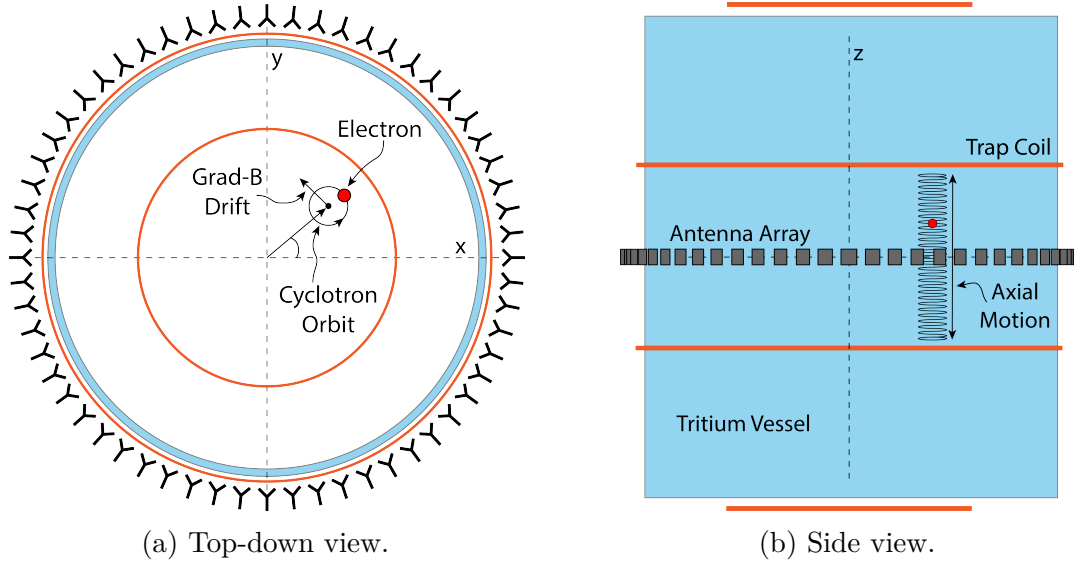


Figure 4.15: An illustration of the conceptual design for an antenna array CRES tritium beta-decay spectrum measurement. The antenna array geometry consists of a 20 cm interior diameter with 60 independent antenna channels arranged evenly around the circumference. The nominal antenna design is sensitive to radiation in the frequency range of 25-26 GHz, which corresponds to the cyclotron frequency of electrons emitted near the tritium beta-spectrum endpoint in a 1 T magnetic field. The array is located at the center of the magnetic trap produced by a set of current-carrying coils. The nominal magnetic trap design is capable of trapping electrons up to 5 cm away from the central axis of the array and traps electrons within an approximately 6 cm long axial region centered on the antenna array.

## 4.4.2 Signal Detection with Antenna Array CRES

### 4.4.2.1 Antenna Array and DAQ System

In order to explore the potential of antenna array CRES for neutrino mass measurement, the Project 8 Collaboration has developed a conceptual design for a prototype antenna array CRES experiment [5, 6], called the Free-space CRES Demonstrator or FSCD, which could be used as a demonstration of the antenna array measurement technique (see Figure 4.15). The FSCD utilizes a single ring of antennas, which is the simplest form of a uniform cylindrical array configuration, to surround a radio-frequency (RF) transparent tritium gas vessel. A prototype version of this antenna array has been built and tested by the Project 8 collaboration to validate simulations of the array radiation pattern and beamforming algorithms [8]. In the FSCD the antenna array is positioned at the center of the magnetic trap formed by a set of electro-magnetic coils that are designed to produce a magnetic trap with flat central region and steep walls both radially and axially.

When a beta-decay electron is trapped its motion consists of three primary components. The component with the highest frequency is the cyclotron orbit whose frequency is determined by the size of the background magnetic field. The FSCD design assumes a background magnetic field value of approximately 0.96 T, which results in cyclotron frequencies for electrons with kinetic energies near the tritium beta-spectrum endpoint from 25 to 26 GHz. The component with the next highest frequency is the axial oscillation experienced by electrons with pitch angles of less than 90° [9]. The flat region of the FSCD magnetic trap extends approximately 3 cm above and below the antenna array plane causing electrons to move back and forth as they are reflected from the trap walls. Typical oscillation frequencies are on the order of 10's of MHz, which results in an oscillation period that is  $O(10^3)$  smaller than the duration of a typical CRES event. Therefore, when reconstructing CRES events we treat the electron as occupying only an average axial position at the center of the magnetic trap, since we are not able to resolve the axial position as a function of time. The component of motion with the smallest frequency is  $\nabla B$ -drift caused by radial field gradients in the trap, producing an orbit of the electron around the central axis of the trap with a frequency on the order of a few kHz, dependent on the pitch angle and the radial position of the electron.

The data acquisition (DAQ) system digitizes the signals from the antenna array and combines thee data streams into a time-ordered matrix of array snapshots that can be used by the reconstruction algorithms. The FSCD DAQ system design [7] is divided into three layers 4.16. The first layer is the RF front-end, which includes the antenna array,

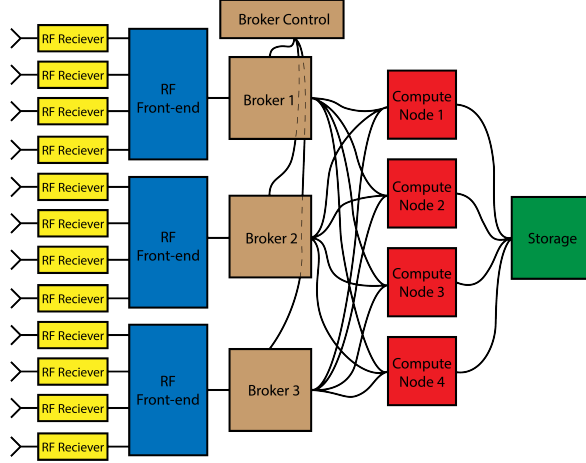


Figure 4.16: A high-level diagram of the DAQ system archctecture envisioned for the FSCD.

the RF receiver boards, and the digitization electronics. The receiver board contains an amplifier, RF mixer, and bandpass filter to enable down-conversion, and is followed by the digitization electronics that sample the CRES signals at 200 MHz. In order to achieve an adequate signal-to-noise ratio to detect CRES events, the DAQ system for the antenna array demonstrator must have a total system noise temperature of  $\approx 10$  K, which we can achieve by using low-noise amplifiers and operating at cryogenic temperatures. After digitization, the array data must be reorganized from individual data streams sorted by channel into array snapshots sorted by time. In order to solve this data transfer and networking problem the second layer of the DAQ system consists of a set of broker computer nodes that reorganize the array data into time-ordered chunks. This approach allows us to accommodate different data transfer requirements by scaling the number of broker nodes in this layer accordingly. Next, the broker layer distributes these chunks of array data to the final layer of the DAQ system, which consists of a set of identical reconstruction nodes that perform the calculations required for CRES reconstruction. Similar to the broker layer, the number of reconstruction nodes can be increased or decreased depending on the amount of computer power required for real-time CRES reconstruction.

The design of the FSCD DAQ system is intended to enable a significant portion of the CRES event reconstruction to occur in real-time. The motivation for this comes from the fact that the FSCD antenna array generates approximately 1 exabyte of raw data per year of operation. Therefore, in order to reduce the data-storage requirements, it is ideal to perform at least some of the CRES event reconstruction in real-time so that it

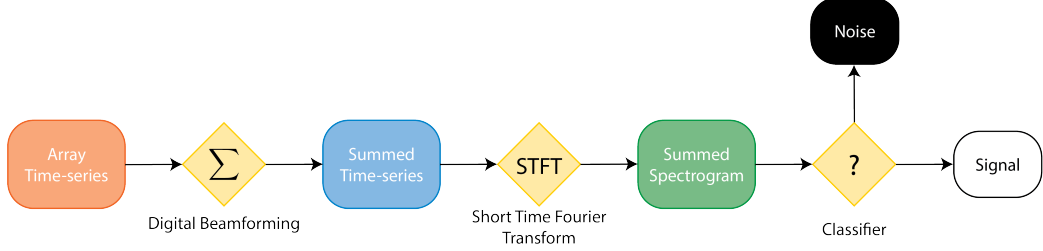


Figure 4.17: A block diagram illustration of the real-time triggering algorithm proposed for antenna array CRRES reconstruction.

is possible to save a reduced form of the data for offline analysis. The first step of the real-time reconstruction would be a real-time signal detection algorithm, which is the focus of this paper. Our approach consists of three main operations performed on the time-series data blocks including digital beamforming, a short time Fourier transform (STFT), and a binary classification algorithm to distinguish between signal and noise data (see Figure 4.17).

#### 4.4.2.2 Real-time Signal Detection

The first step in the real-time detection algorithm is digital beamforming, which is a phased summation of the signals received by individual antennas in the array (see Figure 5.21). The phase shifts correspond to the path length differences between a spatial position and each individual antenna such that, when there is an electron located at the beamforming position, all the signals received by the array constructively interfere. Since we do not know ahead of time where an electron will be produced in the detector, we define a grid of beamforming positions that cover the entire region where electrons can be trapped and perform a phased summation for each of these points for every time-step in the array data block. As we saw in Section 4.4.2.1, the axial oscillation of the electrons prevents us from resolving its position along the Z-axis of the trap, therefore our beamforming grid need only cover the possible positions of the electron in the two-dimensional plane defined by the antenna array.

The equation defining digital beamforming can be expressed as

$$\mathbf{y}[n] = \Phi^T[n]\mathbf{x}[n], \quad (4.38)$$

where  $\mathbf{x}[n]$  is array snapshot vector at the sampled time  $n$ ,  $\Phi[n]$  is the matrix of beamforming phase shifts, and  $\mathbf{y}[n]$  is summed output vector that contains the voltages

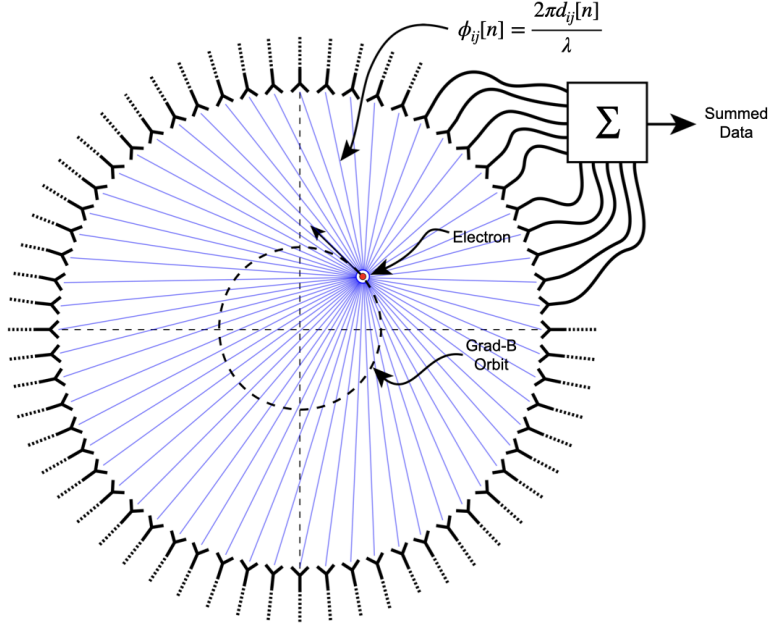


Figure 4.18: An illustration of the digital beamforming procedure. The blue lines indicate the various distances from the beamforming position to the antenna. In the situation depicted the actual position of the electron matches the beamforming position, so we should expect constructive interference when the phase shifted signals are summed. To prevent the electron's  $\nabla B$ -motion from moving the electron off of the beamforming position, the beamforming phase include a time-dependence to follow the trajectory of the electron in the magnetic trap.

for each of the summed channels that correspond to a particular beamforming position. The elements of the beamforming phase shift matrix can be expressed as a weighted complex exponential

$$\Phi_{ij}[n] = A_{ij}[n] \exp(2\pi i \phi_{ij}[n]), \quad (4.39)$$

where the indices  $i$  and  $j$  label the beamforming and antenna positions respectively. The weight  $A_{ij}$  accounts for the relative power increase for antennas that are closer to the position of the electron, and  $\phi_{ij}$  is the total beamforming phase shift for the  $j$ -th antenna at the  $i$ -th beamforming position.

The beamforming phase shift is a sum of two terms

$$\phi_{ij}[n] = \frac{2\pi d_{ij}[n]}{\lambda} + \theta_{ij}[n], \quad (4.40)$$

where the first term is the phase shift originating from the path length difference ( $d_{ij}[n]$ ) between the beamforming and antenna positions, which are represented by the vectors

$(r_j, \theta_j)$  and  $(r_i, \theta_i[n])$ , and the second term is the angular separation ( $\theta_{ij}[n]$ ) of the two positions. The angular separation enters into the beamforming phase due to an effect caused by the circular orbit of the electron that produces radiation whose phase is linearly dependent on the relative azimuthal position of the antenna [10, 11]. The time-dependence of the beamforming phases is intended to correct for the effects of  $\nabla B$ -drift, which cause the guiding centers of electrons to orbit the center of the magnetic trap. By including a linear time-dependence in the azimuthal beamforming position,

$$\theta_i[n] = \omega_{\nabla B} t[n] + \theta_{i,0}, \quad (4.41)$$

where  $\omega_{\nabla B}$  is the azimuthal grad-B drift frequency,  $t[n]$  is the time vector and,  $\theta_{i,0}$  is the starting azimuthal position, we can configure the beamforming phases to effectively track the XY-position of the guiding center over the event duration. Predicting accurate values of  $\omega_{\nabla B}$  for a specific trap and set of kinematic parameters will be done by simulations, which are performed using the Kassiopeia software package [1] by Project 8.

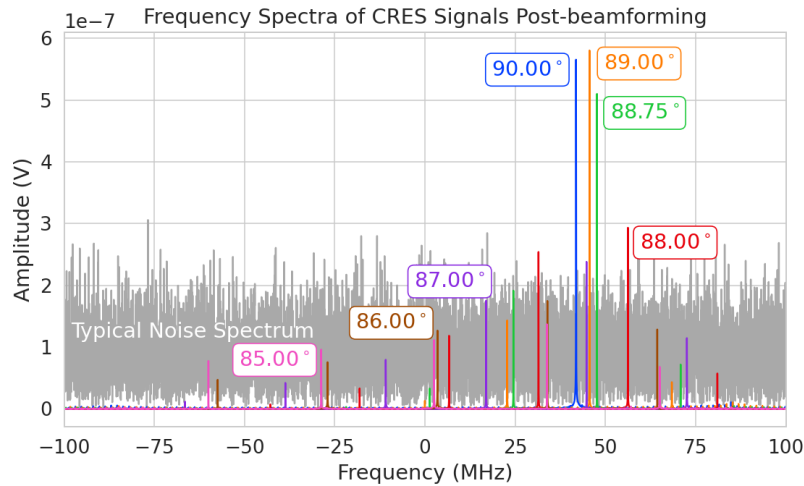


Figure 4.19: Frequency spectra of simulated CRES signals post-beamforming. The signal of a  $90^\circ$  electron consists of a single frequency component that is easy to detect with a power threshold on the frequency spectrum. This power threshold is still effective for signals with relatively large pitch angles such as  $89.0^\circ$  and  $88.75^\circ$ , which are composed of a main carrier and a few small sidebands. Signals with smaller pitch angles, below about  $88.5^\circ$ , tend to be dominated by sidebands such that no single frequency component can be reliably distinguished from the noise with a power threshold.

After digital beamforming, we apply a short-time Fourier transform (STFT) to the summed time-series to obtain the frequency spectrum representation of the signals (see

Figure 4.19). From the detection perspective, the frequency representation of the CRES data is advantageous compared to the time domain, because the frequency spectra of CRES signals are well-approximated by a frequency and amplitude modulated sinusoidal whose carrier frequency increases as a linear chirp. The modulation is caused by the axial oscillation of the electron in the magnetic trap and produce frequency spectra that are well-described by a small number of frequency components. The linear chirp is caused by the energy loss due to cyclotron radiation, which results in a relatively slow increase in the frequency components of the CRES signal over time. During the standard Fourier analysis window for the FSCD of 40.96  $\mu$ sec, we expect a typical CRES signal to increase in frequency by approximately 15 kHz, which is smaller than the frequency bin width given the 200 MHz sample rate. Therefore when considering a single frequency spectrum it is justifiable to neglect the effects of the linear frequency chirp.

In the cases where the electron's pitch angle is  $\gtrsim 88.5^\circ$ , the majority of the signal power is contained in a single frequency component, with the remaining signal power contained in a small number of sidebands proportional to the electron's axial modulation (see Figure 4.19). In these cases detection is relatively straight-forward by implementing a power threshold on the STFT, since the amplitude of the main signal peak is distinct from the thermal noise spectrum. However, as the pitch angle of the electron is decreased below  $88.5^\circ$ , the modulation index of the signal increases causing the maximum amplitude of the frequency spectrum to be comparable to typical noise fluctuations. At this point, the power threshold trigger is no longer able to distinguish between signal and noise leading to a reduction in detection efficiency. The neutrino mass sensitivity of the FSCD is directly linked to the overall detection efficiency. And, because the distribution of electron pitch angles is effectively uniformly distributed across the range of pitch angles that can be trapped, the overall detection efficiency is directly influenced by the range of pitch angles that have detectable signals. Therefore, utilizing a signal detection algorithm that can more effectively identify signals with pitch angles less than  $88.5^\circ$  will improve both detection efficiency and ultimately the neutrino mass sensitivity of the FSCD and other CRES experiments.

Modeling the detection performance of alternative signal detection algorithms for the FSCD requires that we pose the signal detection problem in a consistent manner. The approach we take is to perform a binary hypothesis test on the frequency spectra generated by the STFT. Mathematically, this is expressed as,

$$\mathcal{H}_0 : y[n] = \nu[n] \quad (4.42)$$

$$\mathcal{H}_1 : y[n] = x[n] + \nu[n]. \quad (4.43)$$

Where under hypothesis  $\mathcal{H}_0$ , the vector representing the frequency spectrum ( $y[n]$ ) is composed of pure white Gaussian noise (WGN) represented by  $\nu[n]$ , and under hypothesis  $\mathcal{H}_1$  the frequency spectrum is composed of a CRES signal ( $x[n]$ ) with added WGN. The dominant source of noise in a FSCD-like experiment is expected to be thermal Nyquist-Johnson noise, which is well approximated by a WGN distribution. In order to decide between these two hypotheses we follow the standard Neyman-Pearson approach by performing a log-likelihood ratio test between the probability distributions of the signal classifier output under  $\mathcal{H}_1$  and  $\mathcal{H}_0$  [12]. The output of the log-likelihood ratio test is called the test statistic, which is used to assign the data as belonging to the noise ( $\mathcal{H}_0$ ) or signal ( $\mathcal{H}_1$ ) classes by setting a decision threshold on the value of the test statistic.

In practice, we select the decision threshold by finding the value of the test statistic that guarantees an acceptable rate of false positives and then attempt to maximize the signal detection probability under that fixed false positive rate. Because the signal classifier will be used to evaluate the spectra of  $O(10^2)$  beamforming positions every 40.96  $\mu$ sec, we will require the signal classifiers to operate with decision thresholds that provide false positive rates significantly smaller than 1%. This reduces the burden placed on later stages of the CRES reconstruction chain to reject these false positives and decreases the overall likelihood of reconstructing a false event. Below, we calculate the probability distributions that allow us characterize how different detection algorithms will perform for CRES signals in an FSCD experiment.

### 4.4.3 Signal Detection Algorithms

#### 4.4.3.1 Power Threshold

The power threshold detection algorithm uses the maximum amplitude of the frequency spectra as the detection test statistic. To model the performance of this approach, consider first the case where the signal is pure WGN. For a single bin in the frequency spectrum, the probability that the amplitude falls below a specific threshold value is given by the Rayleigh cumulative distribution function (CDF),

$$\text{Ray}(x; \tau) = 1 - \exp(-|x|^2/\tau), \quad (4.44)$$

where the complex amplitude of the frequency bin is  $x$ , and  $\tau$  is the WGN variance. Because the noise samples for each frequency bin are independent and identically dis-

tributed (IID), the probability that every bin in the frequency spectrum falls below the threshold is the joint CDF formed by the product of each individual frequency bin CDF,

$$F_0(x; \tau, N_{\text{bin}}) = \text{Ray}(x; \tau)^{N_{\text{bin}}}. \quad (4.45)$$

The PDF for the power threshold classifier can then be obtained by differentiating the CDF.

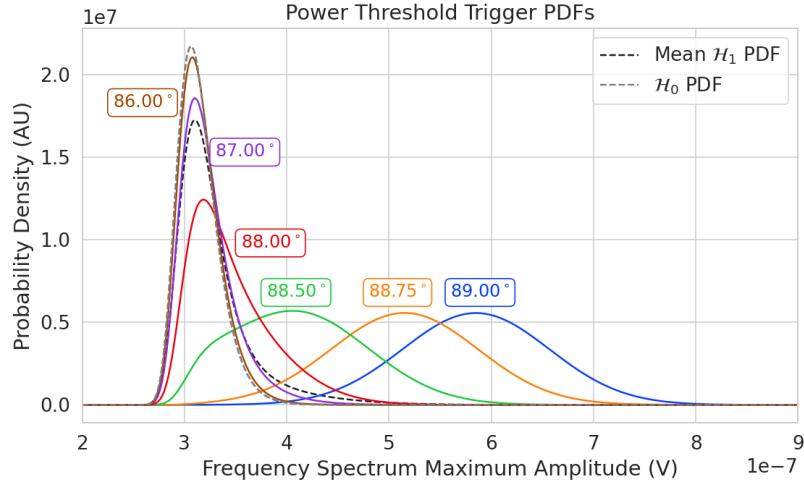


Figure 4.20: PDFs of the power threshold test statistic for CRES signals with various pitch angles as well as the PDF for the noise-only signal case. The average PDF computed for pitch angles ranging from 85.5 to 88.5° is also shown. As the pitch angle is decreased the signal PDF converges towards the noise PDF which indicates that the power threshold trigger is unable to distinguish between small pitch angle signals and noise.

The probability distribution for the power threshold classifier under  $\mathcal{H}_1$  is formed in a similar way, but the frequency bins that contain signal must be treated separately. For a frequency bin that contains both signal and noise we can describe the probability that the amplitude of the bin will fall below our threshold using the Rician CDF,

$$\text{Rice}(x; \tau, \nu) = 1 - Q_1 \left( \frac{|\nu|}{\sqrt{2\tau}}, \frac{|x|}{\sqrt{2\tau}} \right), \quad (4.46)$$

where the parameter  $|\nu|$  defines the noise-free amplitude of the signal and  $Q_1$  is the Marcum Q-function. This time the CDF that describes the probability that the entire

spectrum falls below the decision threshold is the product of both signal and noise CDFs,

$$F_1(x; \tau, \nu, N_{\text{bin}}, N_s) = \text{Ray}(x; \tau)^{N_{\text{bin}} - N_s} \prod_{k=0}^{N_s} \text{Rice}(x; \tau, \nu_k). \quad (4.47)$$

The first half of Equation 4.47 is the contribution from the bins in the frequency spectrum that contain only noise, and the second half is the product of the Rician CDFs for the frequency bins that contain signal peaks with a noise-free amplitude of  $|\nu_k|$ . In Figure 4.20 we show plots of example PDFs under  $\mathcal{H}_1$  and  $\mathcal{H}_0$ .

#### 4.4.3.2 Matched Filtering

The shape of a CRES signal is completely determined by the initial conditions of the electron as it is emitted from beta-decay, which implies that it is possible to apply matched filtering as a signal detection algorithm. With a matched filter one uses the shape of the known signal, which is called a template, to filter the incoming data by computing the convolution between the signal and the data [12]. For cases where the signal is buried in WGN, the matched filter is the optimal detector in that it achieves the maximum probability of a true detection for a fixed false positive rate. Since CRES signals have an unknown shape but are deterministic, we can apply a matched filter by using simulations to generate a large number of signal templates called a template bank, which spans the parameter space of possible signals. Then at detection time, we use the template bank to identify signals by performing the matched filter convolution for each template in an exhaustive search.

As we saw from the frequency spectra in Figure 4.19, CRES signals are highly periodic in nature. In such cases, it is advantageous to utilize the convolution theorem to replace the matched filter convolution with an inner product in the frequency-domain. With the convolution theorem, the matched filter test statistic that describes the detection of a signal buried in WGN using a matched filter template bank is given by

$$\mathcal{T} = \max_{\mathbf{h}} \left| \sum_{n=0}^{N_{\text{bin}}} h^\dagger[n] y[n] \right|, \quad (4.48)$$

where  $h^\dagger[n]$  is the complex conjugate of the signal template. For the case when our template bank consists of only a single template it is possible to derive an exact analytical form for the PDF describing the matched filter test statistic. First, we derive PDF under the signal hypothesis, where the equation describing the matched filter test statistic, also

known as the matched filter score, becomes

$$\mathcal{T} = \left| \sum_{n=0}^{N_{\text{bin}}} h^\dagger[n] y[n] \right|. \quad (4.49)$$

Each noisy frequency bin represented by  $y[n]$  is the sum between value of the signal at that bin and complex WGN, which means that  $y[n]$  is itself Gaussian distributed. Therefore, the value of the inner product between the template and the data is also a complex Gaussian variable; and, since the matched filter score is the magnitude of this inner product, it must follow a Rician distribution.

We can derive the equation for the Rician PDF by expressing the matched filter template  $\mathbf{h}$  in terms of the corresponding simulated signal, which we write as  $\mathbf{x}_h$  to distinguish from the signal in the data. Using the standard normalization and assuming uncorrelated WGN, the matched filter templates can be written as

$$\mathbf{h} = \frac{\mathbf{x}_h}{\sqrt{\tau |\mathbf{x}_h|^2}} \quad (4.50)$$

where  $\tau$  is the noise variance. Inserting this into Equation 4.48 and expressing the data as a sum between a signal and a WGN vector yields,

$$\mathcal{T} = \frac{1}{\sqrt{\tau |\mathbf{x}_h|^2}} \left| \sum_{n=1}^{N_{\text{bin}}} x_h[n] (x[n] + \nu[n]) \right|. \quad (4.51)$$

Next, we transform the expression by isolating the randomly distributed components giving

$$\mathcal{T} = \frac{\left| \sum_{n=1}^{N_{\text{bin}}} x_h[n] x[n] \right|}{\sqrt{\tau |\mathbf{x}_h|^2}} + \frac{1}{\sqrt{\tau |\mathbf{x}_h|^2}} \left| \sum_{n=1}^{N_{\text{bin}}} x_h[n] \nu[n] \right|. \quad (4.52)$$

The first term of 4.52 can be simplified by using the Cauchy-Schawrz inequality to express the magnitude of the inner product in terms of the magnitudes of the signal and template as well as an orthogonality constant which we call "match" ( $\Gamma$ ). Using this we obtain,

$$\mathcal{T} = |\mathbf{h}| |\mathbf{x}| \Gamma + \frac{1}{\sqrt{\tau |\mathbf{x}_h|^2}} \left| \sum_{n=1}^{N_{\text{bin}}} x_h[n] \nu[n] \right|. \quad (4.53)$$

The second term is a sum of Gaussian distributed variables, which we should expect also

follows a Gaussian distribution. Each of the samples  $\nu[n]$  is described by

$$\nu[n] \sim \mathcal{N}(0, \tau), \quad (4.54)$$

where  $\mathcal{N}(0, \tau)$  is a complex Gaussian distribution with zero mean and variance  $\tau$ . Therefore,

$$\frac{x_h[n]}{\sqrt{\tau|\mathbf{x}_h|^2}}\nu[n] \sim \mathcal{N}\left(0, \frac{x_h[n]^2}{|\mathbf{x}_h|^2}\right), \quad (4.55)$$

$$\sum_{n=1}^{N_{\text{bin}}} \frac{x_h[n]}{\sqrt{\tau|\mathbf{x}_h|^2}}\nu[n] \sim \mathcal{N}\left(0, \frac{\sum_{n=1}^{N_{\text{bin}}} x_h[n]^2}{|\mathbf{x}_h|^2}\right) = \mathcal{N}(0, 1), \quad (4.56)$$

$$|\mathbf{h}||\mathbf{x}|\Gamma + \sum_{n=1}^{N_{\text{bin}}} \frac{x_h[n]}{\sqrt{\tau|\mathbf{x}_h|^2}}\nu[n] \sim \mathcal{N}(|\mathbf{h}||\mathbf{x}|\Gamma, 1). \quad (4.57)$$

We see that  $\mathcal{T}$  is magnitude of a complex variable with mean  $|\mathbf{h}||\mathbf{x}|\Gamma$  and variance one. In order to simply the expression a bit further, we define the quantity  $\mathcal{T}_{\text{ideal}} = |\mathbf{h}||\mathbf{x}|\Gamma$ , which we call the ideal matched filter score, because it represents the value of the matched filter inner product that we would expect if no noise was present in the signal. We can write the matched filter test statistic as the magnitude of a two-dimensional vector in the complex plane

$$\mathcal{T} = |(\mathcal{T}_{\text{ideal}} + n_r, n_i)|, \quad (4.58)$$

where  $n_r$  and  $n_i$  are the real and imaginary components of the noise each with variance  $1/2$ , which is modeled by a Rician distribution with shape factor  $\mathcal{T}_{\text{ideal}}$ . Therefore, the probability distribution of the matched filter test statistic is given by,

$$P_1(x; \mathcal{T}_{\text{ideal}}) = 2x \exp(- (x^2 + \mathcal{T}_{\text{ideal}}^2)) I_0(2x\mathcal{T}_{\text{ideal}}), \quad (4.59)$$

where  $I_0$  is the zeroth-order modified Bessel function.

The shape of the matched filter score distribution is controlled by the parameter  $\mathcal{T}_{\text{ideal}}$ , which is effectively the value of the matched filter score if the data contained no noise. Without noise, the data vector reduces to the signal,  $\mathbf{x}$ , in which case Equation 4.49 becomes the magnitude of an inner product between two vectors. We can write the magnitude of an inner product in terms of the lengths of the individual vectors and a constant that describes the degree of orthogonality between them. Applying this to Equation 4.49, we obtain

$$\mathcal{T}_{\text{ideal}} = |\mathbf{h}^\dagger \cdot \mathbf{x}| = |\mathbf{h}| |\mathbf{x}| \Gamma \quad (4.60)$$

where  $\Gamma$  describes the orthogonality between  $\mathbf{h}$  and  $\mathbf{x}$ . From the point of view of matched filtering, we can interpret  $\Gamma$  as describing how well the template matches the underlying signal in the data.

The matched filter score PDF under the noise hypothesis can be readily obtained from Equation 4.59 by setting the value of  $\mathcal{T}_{\text{ideal}}$  to zero, since the data contains no signal in the noise case. Doing this, we obtain the Rayleigh distribution that describes the matched filter score under  $\mathcal{H}_0$ ,

$$P_0(x) = 2x \exp(-x^2). \quad (4.61)$$

Equations 4.59 and 4.61 describe the behavior of the matched filter test statistic under  $\mathcal{H}_0$  and  $\mathcal{H}_1$  for a single template. However, defining a PDF that describes the matched filter test statistic in the case of multiple templates is in general a mathematically intractable problem, since there is no guarantee of orthogonality between matched filter templates. This leads to correlations between the matched filter scores of different templates because only one sample of noise is used to compute the matched filter scores of the template bank. In order to proceed, we need to make the simplifying assumption that we can treat the matched filter scores as IID variables, which allows to ignore correlations between templates. The overall effect of this will be an underestimate of the performance of the matched filter, since we are under counting the number of templates that could contribute a detectable score.

For  $\mathcal{H}_0$  we model the probability that the matched filter score falls below our threshold using the CDF obtained by integrating Equation 4.61. Because we are assuming that the matched filter scores using different templates are independent, the probability that the matched filter score for all templates falls below a threshold value is the joint CDF formed by multiplying the CDF for each template. Under  $\mathcal{H}_0$  this is

$$F_0(x) = \left(1 - e^{-x^2}\right)^{N_t}, \quad (4.62)$$

where  $x$  is the matched filter score threshold and  $N_t$  is the number of templates. We should expect that the distribution describing the matched filter template bank maximum score depends on  $N_t$ , because with more templates there is a greater chance of a random match between the template and data.

For  $\mathcal{H}_1$ , we start by denoting the CDF of the best matching template as  $F_{\text{best}}(x; \mathcal{T}_{\text{best}})$ , and treat the matched filter scores for all other templates as negligible ( $\mathcal{T}_{\text{ideal}} \approx 0$ ). Then we form the joint CDF by combining the distributions for all templates used during

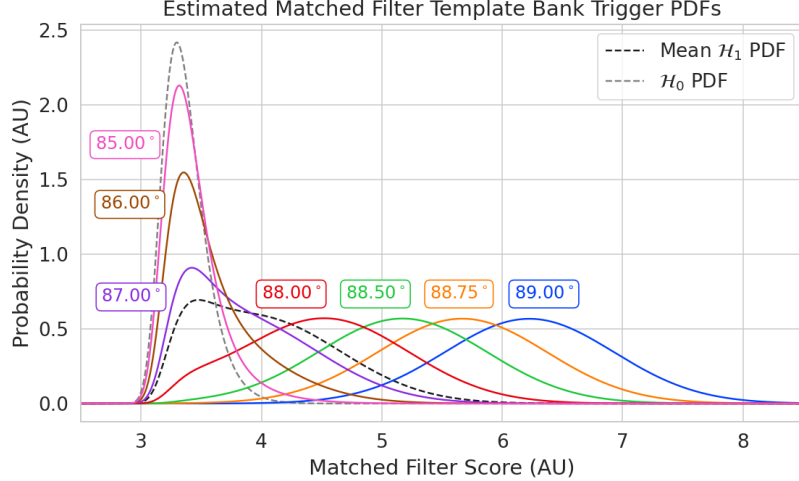


Figure 4.21: Plots of the estimated PDFs for the matched filter template bank test statistic for CRES signals with various pitch angles as well as the estimated PDF for the noise only signal case. We assume an estimated number of templates of  $10^5$  and perfect match between signal and template i.e.  $\Gamma_{\text{best}} = 1$ . The mean PDF includes signals ranging from  $85.5 - 88.5^\circ$  in pitch angle. There is a much larger distinction between the signal PDFs at small pitch angle compared to the power threshold indicating a higher detection efficiency for these signals.

detection. Since we are exhaustively checking the matched filter scores, the number of templates checked will be a randomly distributed variable that ranges from zero to the total number of available templates. If we assume that signals are uniformly distributed across the parameter space spanned by the template bank then on average we check  $(N_t - 1)/2 \approx N_t/2$  templates for each inference. Therefore, the estimated CDF under  $\mathcal{H}_1$  is

$$F_1(x; \mathcal{T}_{\text{best}}) = F_{\text{best}}(x; \mathcal{T}_{\text{best}}) \left(1 - e^{-x^2}\right)^{N_t/2}. \quad (4.63)$$

In Figure 4.21 we show plots of the estimated matched filter template bank classifier PDFs under both  $\mathcal{H}_0$  and  $\mathcal{H}_1$ .

#### 4.4.3.3 Machine Learning

In this paper we focus on Convolutional Neural Networks (CNN) as an example of a machine learning based signal classifier. CNNs are constructed using a series of convolutional layers, each composed of a set of filters that are convolved with the input data. The individual convolutional filters can be viewed as matched filter templates that are learned from a set of simulated data rather than being directly generated. This opens

the possibility of finding a more efficient representation of the matched filter templates during the training process that can potentially reduce computational cost at inference time while still offering good classification performance.

The machine learning approach is distinct from both the power threshold and matched filtering in that we do not attempt to manually engineer a test statistic that is computed from the data for classification. Instead, we attempt calculate the test statistic by constructing a differentiable function that maps the complex frequency series generated by the STFT to a binary classification as either signal or noise. The test statistic for the machine learning classifier can be expressed as

$$\mathcal{T} = G(\mathbf{y}; \boldsymbol{\Omega}) \quad (4.64)$$

where  $\mathbf{y}$  is the noisy data vector and  $G(\mathbf{y}; \boldsymbol{\Omega})$  is the machine learning model parameterized by the weights  $\boldsymbol{\Omega}$ . By using supervised learning on a labeled set of training signals, we can modify the function parameters to learn the mapping from the data to the likelihood of  $\mathbf{y}$  belonging to either  $\mathcal{H}_1$  or  $\mathcal{H}_0$ .

Table 4.1: A summary of the CNN model layers and parameters. The output of each 1D-Convolution and Fully Connected layer is passed through a LeakyReLU activation function and re-normalized using batch normalization before being passed to the next layer in the model. The output of the final Fully Connected layer in the model is left without activation so that the model outputs can be directly passed to the Binary Cross-entropy loss function used during training.

Layer	Type	Input Channels	Output Channels	Parameters
1	1D-Convolution	2	15	( $N_{\text{kernel}} = 4$ , $N_{\text{stride}} = 1$ )
2	Maximum Pooling	15	15	( $N_{\text{kernel}} = 4$ , $N_{\text{stride}} = 4$ )
3	1D-Convolution	15	20	( $N_{\text{kernel}} = 4$ , $N_{\text{stride}} = 1$ )
4	Maximum Pooling	20	20	( $N_{\text{kernel}} = 4$ , $N_{\text{stride}} = 4$ )
5	1D-Convolution	20	25	( $N_{\text{kernel}} = 4$ , $N_{\text{stride}} = 1$ )
6	Maximum Pooling	25	25	( $N_{\text{kernel}} = 4$ , $N_{\text{stride}} = 4$ )
7	Fully Connected	3200	512	NA
8	Fully Connected	512	64	NA
9	Fully Connected	64	2	NA

The CNN architecture used for this work is summarized by Table 4.1. No strategic hyper-parameter optimization approach was implemented beyond the manual testing of different CNN architecture variations, so this particular model is best viewed as a proof-of-concept rather than a rigorously optimized design. Numerous model variations were tested, some with significantly more layers and convolutions filters per layer, as

well as others that were even smaller than the architecture in Table 4.1. Ultimately, the model architecture choice was driven by the motivation to find the minimal model whose classification performance was still comparable to the larger CNN’s tested, because of the importance of minimizing computational cost in real-time applications. It is possible that more sophisticated machine learning models could improve upon the classification results achieved here, but we leave this investigation for future work.

#### 4.4.4 Methods

##### 4.4.4.1 Data Generation

To test the triggering performance of the classifiers, simulated CRES signals were generated using the Locust simulations package [10, 13] developed by the Project 8 collaboration. Locust uses the separately developed Kassiopeia package to calculate the magnetic fields produced by a user defined set of current carrying coils along with any specified background magnetic fields, resulting in a magnetic trap. Next, Kassiopeia calculates the trajectory of an electron in this magnetic field starting from a set of user specified initial conditions. The Locust software then uses the electron trajectories from Kassiopeia to calculate the resulting electromagnetic fields using the Liénard-Wiechert equations, and determine the voltages generated in the antenna array with the antenna transfer function. Locust then simulates the down-conversion, filtering, and digitization steps resulting in the simulated CRES signals for an electron.

The shape of the received CRES signal is determined by the initial kinematic parameters, including the starting position of the electron, the starting kinetic energy of the electron, and the pitch angle. For the studies performed here we constrain ourselves to a single initial electron position located at  $(x, y, z) = (5, 0, 0)$  mm, and using this starting position we generate two datasets by varying the initial kinetic energy and the starting pitch angle. The first dataset consists of a two-dimensional square grid of kinetic energy and pitch angle spanning an energy range from 18575-18580 eV with a spacing of 0.1 eV, and pitch angles from 85.5-88.5° with a spacing of 0.001°, resulting in 153051 signals with a unique energy-pitch angle combination. This dataset is intended to represent a matched filter template bank. The second dataset was generated by randomly sampling uniform probability distributions covering the same parameter space to produce approximately 50000 signals randomly parameterized in energy and pitch angle. This dataset provides the training and test data for the machine learning approach, and acts as a representative sample of signals to evaluate the performance of the matched filter template bank.

Each signal was simulated for a duration of  $40.96 \mu\text{s}$ , which is equivalent to 8192 samples at the FSCD digitization rate, and begins at time  $t = 0 \text{ s}$  for all simulations. This duration represents a single frequency spectrum generated by the STFT. The output of the Locust simulation is a matrix of array snapshots with size given by the number of channels times the event length ( $N_{\text{ch}} \times N_{\text{sample}}$ ), which we pre-process using the digital beamforming summation and STFT described in Section 4.4.2.2. The  $\nabla B$ -drift correction uses the exact value of  $\omega_{\nabla B}$ , obtained from the Kassiopeia simulation of that electron. In practice, an average value for  $\omega_{\nabla B}$  could be used, because there is limited variation in drift frequency across this parameter space.

#### 4.4.4.2 Template Number and Match Estimation

The estimated PDF for the matched filter template bank depends on the score of the best matching template or equivalently the match of the best template ( $\Gamma_{\text{best}}$ ) as well as the number of templates. One expects that with a higher number of templates the average value of  $\Gamma_{\text{best}}$  will increase, however, there is a point of diminishing returns at which more templates will not significantly increase match, but will still increase the likelihood of false positives. Therefore, it is desirable to use the minimum number of templates that provide an acceptable mean value of  $\Gamma_{\text{best}}$ .

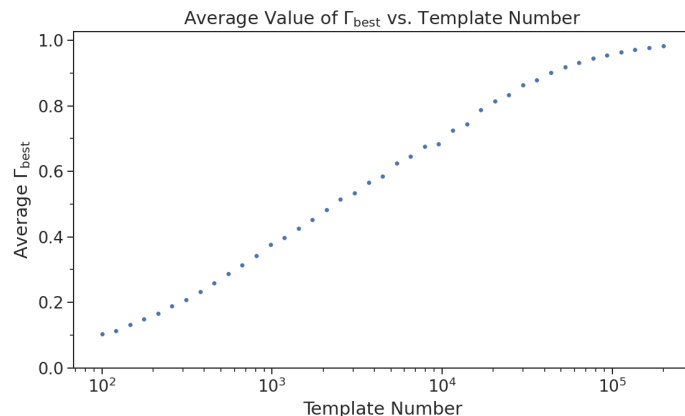


Figure 4.22: The mean match of the matched filter template bank to a test set of randomly parameterized signals as a function of the number or density of templates. The parameter space includes pitch angles from  $85.5 - 88.5^\circ$  and energies from  $18575 - 18580 \text{ eV}$ .

To quantify the relationship between match and template number, we calculated the mean match of the random dataset to a selection of templates obtained from the regularly spaced dataset. The results are shown in Figure 4.22, where we find that the

average value of  $\Gamma_{\text{best}}$  is an exponential function of the number of templates. From this plot we select the desired value of mean match at which we would like to evaluate the matched filter PDF and can infer the required number of templates.

#### 4.4.4.3 CNN Training and Data Augmentation

To prepare the data for training the model, we split the random dataset in half to create distinct training and test datasets. Additionally, a randomly selected 20% of the training data is isolated for use as a validation set during the training loop. The size of the training, validation, and test datasets are then tripled by appending two additional copies of the data to increase the sample size of the dataset after data augmentation. The data is loaded with no noise, which is added to each data batch during the training phase by generating a new noise sample from a complex WGN distribution. In order to ensure an even split between signal and noise data we append to the noise-free signals an equal number of empty signals composed of all zeros. Therefore, as the data is randomly shuffled during training, on average an equal number of empty signals will be included with the training signals. After adding the sample of WGN to the data batch, the empty signals represent the noise-only data that the model must distinguish from signal data.

As the training signals are loaded we apply a unique random phase shift as the first form of data augmentation. Since the data is generated using the same initial axial position and cyclotron orbit phase, the randomization is an attempt to prevent overtraining on these features. During each training epoch the data is randomly shuffled and split into batches of 2500 signals. Each batch of signals is then circularly shifted by a random number of frequency bins to simulate a kinetic energy shift from  $-75$  to  $20$  eV to simulate a training dataset with a larger energy range. Next, a sample of complex WGN, consistent with the expected 10 K Nyquist-Johnson noise expected for the FSCD, is generated and added to the signal, which prevents overtraining on noise features. As a final step, the data is renormalized by the standard deviation of the noise so that the range of values in the data is close to  $[-1, 1]$ , which helps ensure well-behaved back-propagation.

The Binary Cross-entropy loss function is used to compute the loss for each batch of data and the model weights are updated using the ADAM optimizer with a learning rate of  $5 \times 10^{-3}$ . After each training epoch, the loss and classification accuracy of the validation dataset are computed to monitor for overtraining. It was noticed that the relatively high noise power and the fact that a new sample of noise was used for each batch together provided a strong form of regularization, since no evidence of over-training was observed

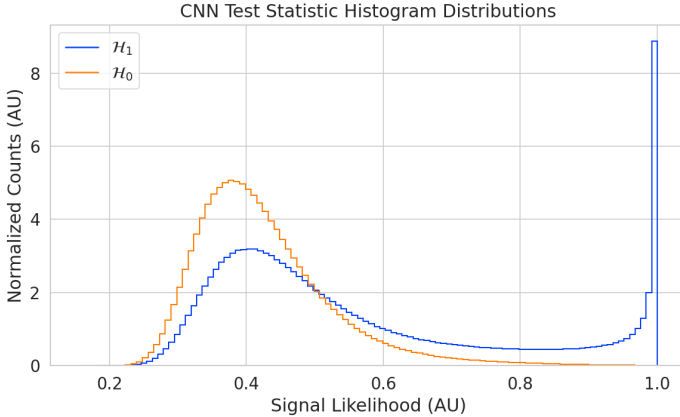


Figure 4.23: Histograms of the trained CNN model output from the test dataset. The blue histogram shows the model outputs for signal data. The oddly shaped peak near the end is the result of the softmax function mapping the long tail of the raw output distribution to the range  $[0, 1]$ .

even after several thousand epochs. Typically, the loss and classification accuracy of the model converged after a few hundred training epochs, but the training loop was extended to 3000 epochs to attempt to achieve the best possible performance. The training procedure generally took about 24 hrs using a single NVIDIA V100 GPU [14].

After training the model, we use it to classify the test dataset and generate histograms of the model outputs for both classes of data. The data augmentation procedure for the evaluation of the test data mirrors the training procedure without the validation split. Since a random circular shift and a new sample of WGN is added to each batch, the testing evaluation loop is run for 100 epochs to get a representative sample of noise and circular shifts. The model outputs for each batch are passed through a softmax activation and then combined into histograms, which we show in Figure 4.23.

## 4.4.5 Results and Discussion

### 4.4.5.1 Trigger Classification Performance

Using the matched filter and power threshold CDFs, along with the classification results from the CNN, we compare detection performance by computing receiver operating characteristic (ROC) curves. Specifically, we compare the detection performance averaged over the full signal parameter space in order to get a measure of the overall detection efficiency achieved by each algorithm. For the power threshold and matched filter algorithms, we obtain the mean ROC curve by taking the average over all signals in the

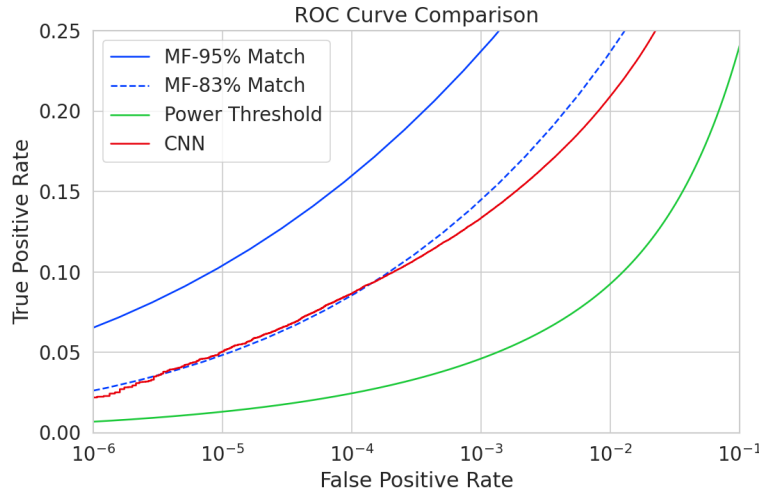


Figure 4.24: ROC curves describing the detection efficiency or true positive rates for the three signal classification algorithms examined in this paper.

regularly spaced dataset. In the case of the matched filter, we examine two cases using different numbers of templates, which have different values of mean match. The ROC curve describing the CNN is obtained by forming a histogram of the network outputs for each class of signal and from this computing the estimated CDFs and ROC curve. In Figure 4.24, we show the ROC curves obtained for each of the detection algorithms, visualized in terms of true positive rate and false positive rate.

The true positive rate of a signal classifier is equivalent to its detection efficiency, and we see that for the population of signals with pitch angles  $< 88.5^\circ$  the power threshold has a consistently lower detection efficiency than the CNN and the matched filter. This result could have been predicted from the visualization of signal spectra in Figure 4.19, where we see that there is no way to distinguish between a noise peak and a signal peak with high confidence at small pitch angles. The CNN offers a significant and consistent increase in detection efficiency over the power threshold approach, with the relative improvement in detection efficiency increasing as the false positive rate decreases. If we compare the CNN to the matched filter, we see that the performance of the tested network is roughly equivalent to a matched filter detector with an average match of about 83%, which uses approximately 20000 matched filter templates. The overall best detection efficiency is achieved by the matched filter classifier if a large enough template bank is used. We show in the plot the ROC curve for a matched filter template bank with 95% average match, which is achieved with approximately 100000 templates. Since the matched filter is known to be statistically optimal for detecting a known signal in

WGN, it is somewhat expected that this algorithm has the highest detection efficiency.

A potentially impactful difference between the matched filter and CNN algorithms is that the CNN relies upon convolutions as its fundamental calculation mechanism, whereas our implementation of a matched filter utilizes an inner product. Since convolution is a translation invariant operation, the detection performance of CNN can be extended to a wider range of CRES event kinetic energies with less cost than the matched filter, a feature that we exploited during the CNN training by including circular translations of the CRES frequency spectra in the training loop. Increasing the range of kinetic energies detectable by a matched filter requires a proportional increase in the number of templates, which directly translates into increased computational and hardware costs. From a practical perspective, the detection algorithm is always limited by the available computational hardware, so estimating the relative costs is a key factor in determining their feasibility. Below we perform a more detailed analysis of the relative costs of each of the detection algorithms.

#### 4.4.5.2 Computational Cost and Hardware Requirements

In the process of investigating triggering approaches for an antenna array CRES experiment, we have uncovered a strong tension between detection efficiency and computational resources. To relate the computational cost estimates to actual costs, we compare the theoretical amount of computer hardware required to implement the signal classifiers for real-time detection in an FSCD experiment. To do this we shall utilize order of magnitude estimates of the theoretical peak performance values for currently available Graphics Processing Units (GPUs) as a metric. This approach will underestimate the amount of required hardware, since it is unlikely that any CRES detection algorithm could reach the theoretical peak performance of the hardware.

Of the three detection algorithms tested, the power threshold classifier is the least expensive. It requires that we check whether the amplitude of each frequency bin in the STFT is below or above our decision threshold. The STFT combined with digital beamforming produces  $N_{\text{bin}}N_b$  frequency bins that must be checked every  $N_{\text{bin}}/f_s$  seconds. This requires approximately  $O(10^{10})$  FLOPS to check in real-time. Current generations of GPUs have peak theoretical performances in the range of  $O(10^{13}) - O(10^{14})$  FLOPS [15], dependent on the required floating-point precision of the computation. Therefore, the entire computational needs of a real-time triggering system using a power threshold classifier, including digital beamforming and generation of the STFT, could be met by a single high-end GPU or a small number of less powerful GPUs. Since triggering is only

one step of the full real-time signal reconstruction approach, limiting the computational cost of this stage is ideal. However, we have seen that the power threshold classifier does not provide sufficient detection efficiency across the entire range of possible signals, which is the primary motivation for exploring more complicated triggering solutions.

As discussed, the computational cost of the matched filter approach requires counting the number of templates that must be checked for each frequency spectra produced by the STFT. Computing the matched filter scores requires  $O(N_b N_t N_{\text{bin}})$  operations, since for each of the  $N_b$  beamforming positions we must multiply  $N_t$  templates with a data vector that has length  $N_{\text{bin}}$ . The time within which we must perform this calculation is equal to  $N_{\text{bin}}/f_s$  to keep up with the data generation rate. To cover the 5 eV kinetic energy range spanned by the template bank, we saw that  $10^4$  to  $10^5$  templates are required in order to match or exceed the detection efficiency of the CNN. If the number of templates scales linearly with the kinetic energy range of interest as expected, then we would require  $10^5$  to  $10^6$  matched filter templates with this more realistic range of energies. Considering this, the estimated computational cost of the matched filter is between  $O(10^{15})$  to  $O(10^{16})$  FLOPS, which is  $O(10^2)$  to  $O(10^3)$  high-end GPUs.

Lastly, we have the CNN classifier. To estimate the computational cost we simply sum the number of convolutions and matrix multiplications specified by the network architecture shown in Table 4.1. Each convolutional layer consists of  $N_{\text{in}} N_{\text{out}} N_{\text{kernel}} L_{\text{input}}$  floating-point operations, where  $N_{\text{in}}$  is the number of input channels,  $N_{\text{out}}$  is the number of output channels,  $N_{\text{kernel}}$  is the size of the convolutional kernel, and  $L_{\text{input}}$  is the length of the input vector, and the fully connected layers each contribute  $N_{\text{in}} N_{\text{out}}$  operations. Summing all the neural network layers we estimate that the CNN would require  $O(10^6)$  floating point operations for each frequency spectra; therefore, the total computation cost of the CNN trigger is this cost times the number of beamforming positions per the data acquisition time, which is  $O(10^{13})$  FLOPS or  $O(10^0)$  GPUs.

Compared with the matched filter approach the CNN requires  $O(100)$  to  $O(1000)$  fewer GPUs to implement, dependent on the exact number of templates used in the template bank. The 100 eV kinetic energy range is motivated by the application of these detection algorithms to an FSCD-like neutrino mass measurement experiment. However, if a significantly larger range of kinetic energies is required, a CNN may be the preferred detection approach despite the lower average detection efficiency due to computational cost considerations. The low estimated computational cost of the CNN is directly related to the small network size.

Additional experiments with larger CNNs, generated by increasing the depth and

width of the neural network, and we observed that these changes provided minimal ( $\lesssim 1\%$ ) improvement in the classification accuracy of the model. A potential reason for this could be the sparse nature of the signals in the frequency domain and the low SNR which makes for a challenging dataset to learn from. Future work could investigate modifications to the neural network architecture such as sparse convolutions, which may improve the classification accuracy of the model or further reduce the computational costs of this approach. Alternatively, more complicated CNN architectures such as a ResNet [16] or VGG model [17] may provide improved classification performance over a basic CNN. An additional promising area of investigation are recurrent neural networks, which may be able to exploit the time-ordered features of the STFT for more accurate signal detection if the electron signals last for multiple Fourier transform windows.

Our estimate of the computational cost of the matched filter is somewhat naive if we notice that the majority of the values that make up a CRES frequency spectra are zero (see Figure 4.19). Therefore, the majority of operations in the matched filter inner product are unnecessary, and we could instead evaluate the matched filter inner product using only the  $\lesssim 10$  frequency peaks that make up CRES signal. This optimization reduces the number of operations required to check each template by a factor of  $O(100)$  to  $O(1000)$ , which brings the estimated computational cost of the matched filter in line with the CNN. Although this level of sparsity results in a multiplication with very low arithmetic complexity, the resulting sparse matched filter algorithm is still likely to be constrained by memory access speed rather than compute speed. Ultimately, the comparison of the relative computational and hardware costs between the matched filter and CNN will depend on the efficiency of the software implementation and hardware support for neural network and sparse matrix calculations.

#### 4.4.6 Conclusion

Increasing the detection efficiency and overall event rate of the CRES technique represents a key developmental path towards new scientific results and broader applications of the CRES technique. It is what motivates both the antenna array detection approach and the development of real-time signal reconstruction algorithms. We have demonstrated that significant gains in the detection efficiency of the CRES technique are achievable by utilizing triggering algorithms that account for the specific shape of CRES signals in the detector. These algorithms emphasize the need for accurate and fast methods for CRES simulation, since they directly contribute to the success of matched filter methods by providing a way to generate expected signal templates and also serve as a source of

training data for machine learning approaches.

The improvements in detection efficiency offered by these alternative approaches to triggering are crucial to the success of efforts to develop scalable technologies for CRES measurement, since they provide a significant increase in the detectable parameter space of CRES events, which allows for a better utilization of the larger detection volume. While we have focused on the real-time detection of CRES signals from antenna arrays, these same signal classifiers could be used in CRES experiments utilizing a different detector technologies, since the same principles of signal detection will apply. For example, previous CRES measurements by the Project 8 collaboration that utilized a waveguide gas cell, could have improved their detection efficiency by employing a matched filter or neural network classifier to identify trapped electrons with pitch angles that are too small to be detected by the power threshold approach. Furthermore, alternative CRES detector technologies such as resonant cavities [5] could also see similar improvements in detection efficiency, which is of crucial importance to future efforts by the Project 8 collaboration to utilize CRES to measure the neutrino mass.

# **Chapter 5**

# **Antenna and Antenna Measurement System Development for the Project 8 Experiment**

## **5.1 Introduction**

The FSCD and antenna array CRES represent an innovative approach to beta-decay spectroscopy. While much can be learned from simulations about the systematics of CRES with antenna arrays, laboratory measurements and demonstrations provide critical inputs to sensitivity and simulation models as well as provide the means for calibration and commissioning of the experiment. Therefore, a robust program of antenna and antenna measurement hardware development is important to the success of experiments like the FSCD and the development of antenna array CRES more broadly.

In this chapter we summarize the development of an antenna measurement system at Penn State to implement and test the techniques of antenna array CRES on the bench-top, in order to support the efforts of the Project 8 collaboration. In Section 5.2 we provide an introduction to some fundamental parameters and concepts related to antenna measurements as well as an overview of the Penn State antenna measurement system hardware. In Section 5.3 we include the manuscript of a paper which details the design and characterization of a specialized antenna developed to mimic the electric fields emitted by an electron in a CRES experiment. This antenna, called the Synthetic Cyclotron Antenna (SYNCA), is intended as a calibration tool for antenna arrays developed for CRES measurements. Lastly, in Section ?? we summarize a set of prototype FSCD antenna array measurements with the SYNCA, which we use to validate the simulated performance of the antenna array and estimate systematic errors associated with the antenna array.

## 5.2 Antenna Measurements for CRES experiments

### 5.2.1 Antenna Parameters

Antenna characterization measurements will allow Project 8 to have confidence that the antenna array we use for CRES measurements will allow us to reach our neutrino mass sensitivity goals. In this section, we shall summarize a few fundamental concepts relating to antennas and antenna measurement, before introducing how Project 8 uses antenna measurement for the development of antenna array CRES.

#### 5.2.1.1 Radiation Patterns

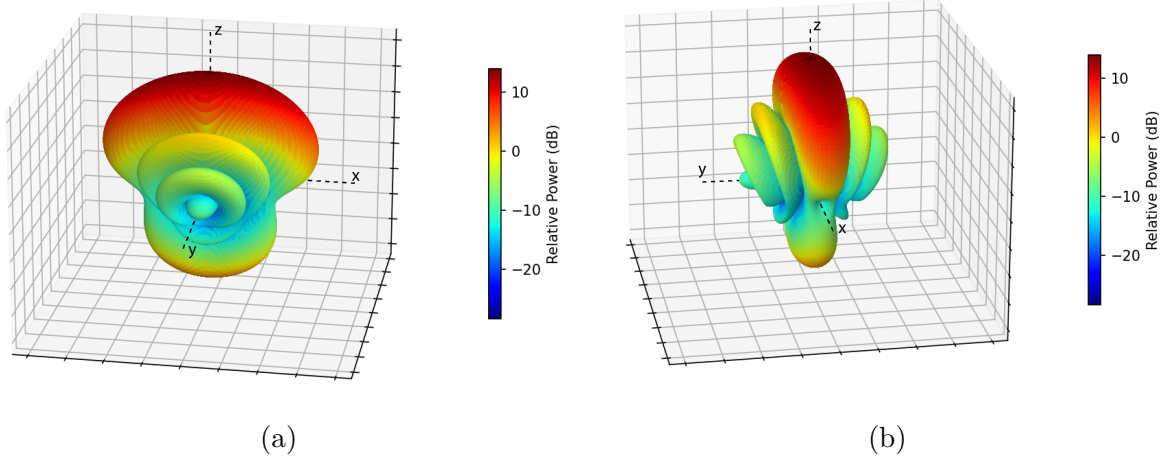


Figure 5.1: An example radiation pattern generated using HFSS simulations. The color and radial distance of the surface from the origin indicate the relative magnitude of radiation power emitted by the antenna in that direction. The primary goal of most antenna measurements is to characterize this feature of an antenna since it can be used to derive many useful quantities about the antenna. In Project 8 we are most interested in measuring the radiation pattern of the antennas used to build the array for CRES measurement in order to validate that the antenna array's performance matches simulation.

Antennas are conductive structures designed to carry alternating electric currents in order to transmit energy in the form of electro-magnetic (EM) waves. One fundamental way to characterize a particular antenna, is to map out the radiated power density as a function of position, which is called the radiation pattern 5.1). We find the radiation power density by calculating the time-averaged Poynting vector for all positions surrounding

the antenna, which in equation form is,

$$\mathbf{W}(x, y, z) = \langle \mathbf{E}(x, y, z, t) \times \mathbf{H}^*(x, y, z, t) \rangle_t, \quad (5.1)$$

where  $\mathbf{E}(x, y, z, t)$  and  $\mathbf{H}(x, y, z, t)$  are the time-dependent electric and magnetic fields produced by the antenna. The radiation power density has units of  $\text{W/m}^2$  and is more typically called the energy flux density in physics applications, since it is a measure of the amount of energy passing through a unit area over time. Because the radiation power density is a measure of power per unit area, its value in a particular direction will depend on the distance from the antenna at which we are measuring, which is not ideal for antenna characterization measurements. A related quantity is the energy flux per unit solid angle or radiation intensity which can be computed directly from the radiation power density by multiplying by the squared distance from the antenna. Specifically,

$$U = r^2 W(x, y, z), \quad (5.2)$$

where  $r$  is the distance from the antenna to the field measurement point. The radiation intensity is typically defined in regions where the Poynting vector consists only of a radial component where it is safe to treat as a scalar quantity.

### 5.2.1.2 Directivity and Gain

Since the radiation intensity is a measure of average power per unit solid angle, it is independent of distance and more useful as feature for antenna measurement. However, most antenna measurements are performed in terms of the directly related directivity and gain quantities. Directivity is defined as the ratio between the radiation intensity at particular point on the radiation pattern to the average radiation intensity computed over all solid angles. The equation that relates the radiation intensity to directivity is

$$D = \frac{U}{U_0} = \frac{4\pi U}{P_{\text{rad}}}, \quad (5.3)$$

where  $U_0$  is the average radiation intensity over all solid angles, which simply the total radiated power ( $P_{\text{rad}}$ ) divided by  $4\pi$ . Closely related to directivity is concept of gain, which accounts for energy losses that occur inside the antenna when attempting to transmit or receive a signal. The antenna gain is given by

$$G = \frac{4\pi U}{P_{\text{in}}}, \quad (5.4)$$

where  $P_{\text{in}}$  is the total power delivered to the antenna. Gain can be thought of as the ratio of the antenna's radiation intensity to that of a hypothetical isotropic, lossless radiator. The maximum values of gain and directivity exhibited by the main lobe of the antenna pattern as well as the ratio between the gain of the main lobe and any side-lobes are important figures of merit used to evaluate antenna designs.

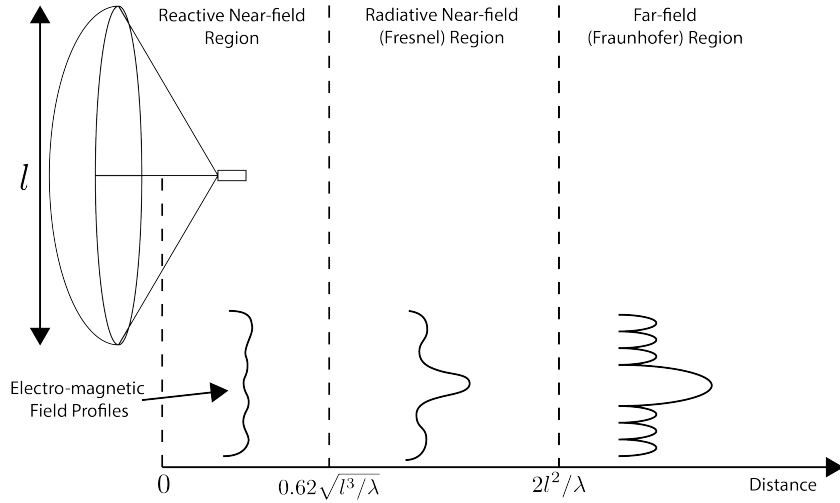


Figure 5.2: An illustration of the three field regions important for the analysis of an antenna system. Very close to the antenna the electric fields are primarily reactive so there is no radiation. If a receiving antenna were placed in this region most of the energy would be reflected back to the transmitter. Outside of the reactive near-field is the radiative near field. At these distances the antenna does radiate, but the radiation pattern is not well-defined since it changes based on the distance of the receiving antenna. It is only in the far-field region where the radiation pattern becomes constant as a function of distance, which is where the majority of antenna engineering is assumed to take place. The antenna arrays developed by Project 8 for CRES measurements operate in the radiative near-field due to the importance of limiting power loss from free-space propagation, which complicates the design of the antenna system.

### 5.2.1.3 Far-field and Near-field

Radiation patterns are typically only defined in regions where the shape of the radiation pattern is independent of distance. The region where this approximation is valid is called the far-field, and in this region we can treat the EM fields from the antenna as spherical plane waves. A rule of thumb for antennas that are larger than the wavelength of the radiation they emit is that the far-field approximation can be applied in regions where

$$R > \frac{2l^2}{\lambda}, \quad (5.5)$$

applied. In this expression,  $R$  is the distance from the antenna,  $l$  is the largest characteristic dimension of the antenna, and  $\lambda$  is the wavelength of the radiation (see Figure 5.2). The region very close to the antenna is called the reactive near-field, because in this region the reactive component of the EM field is dominant. Unlike radiative electric fields, the reactive electric and magnetic fields are out of phase from each other by  $90^\circ$ , since they are the result of electrostatic and magnetostatic effects coming from the self-capacitance and self-inductance of the antenna. The reactive fields are unable to transfer energy a significant distance from the antenna and are thus completely negligible for most antenna applications. The limit of the reactive near-field for an electrically-large antenna is typically taken to be

$$R < 0.62\sqrt{l^3/\lambda}. \quad (5.6)$$

In between the reactive near-field and the far-field is the radiative near-field region. In this region the fields are primarily radiative, however we are still too close to the antenna for the spherical plane wave approximation to apply. Therefore, interference effects between EM waves emitted from different points on the antenna occur causing the shape of the radiation pattern to change as a function of distance from the antenna. If we evaluate the far-field distance limit for the antenna array demonstrator experiment explored in Chapter ?? using the 5 cm long slotted waveguide antenna and the 26 GHz target frequency we find an estimated far-field distance of 43 cm which is a factor of four larger than the radius of the antenna array designed for the experiment. Consequently, we expect near-field effects to influence the performance of the antenna array highlighting the importance of calibration and characterization measurements.

#### 5.2.1.4 Polarization

Up to now, we have ignored the issue of polarization as it relates to antenna theory. The polarization of an EM wave defines the spatial orientation of the electric field oscillations in the plane perpendicular to the direction of the propagation, and is defined in terms of orthogonal polarization components. For antennas, we are analyzing the properties of radiation propagating along the radial ( $\hat{r}$ ) direction, which implies that the electric fields can be described as a linear combination of orthogonal polarization components such as

$$\mathbf{E}_{\text{tot}} = E_x \hat{x} + E_y \hat{y} + E_z \hat{z}, \quad (5.7)$$

in Cartesian coordinates, or

$$\mathbf{E}_{\text{tot}} = E_\theta \hat{\theta} + E_\phi \hat{\phi}, \quad (5.8)$$

in spherical coordinates. When we are dealing with an antenna that radiates with a specific polarization we define partial radiation patterns, directivities, and gains so that the performance of the antenna for the desired polarization can be analyzed. The radiation pattern defined in terms of partial patterns is

$$U_{\text{tot}} = U_\phi + U_\theta, \quad (5.9)$$

where  $U_\phi$  and  $U_\theta$  are the radiation intensities in a particular direction for the respective polarization components. Similarly, a quantity such as gain can be written in terms of partial gains,

$$G_{\text{tot}} = G_\phi + G_\theta = \frac{2\pi U_\phi}{P_{\text{in}}} + \frac{2\pi U_\theta}{P_{\text{in}}}. \quad (5.10)$$

If we view an electron performing a circular orbit in the XY-plane from the side, that is, along the X or Y axes, then we would observe the electron to be performing a linear oscillation perpendicular to the viewing axis. From this intuitive picture, we can predict that the primary polarization of electric fields from CRES events to be linearly polarized in the  $\hat{\phi}$  direction when viewed with an antenna positioned in the XY-plane, which influences the antenna array demonstrator design.

### 5.2.1.5 Antenna Factor and Effective Aperture

Oftentimes, a useful way to characterize the performance of an antenna is to measure the electric field magnitude required to produce a signal with an amplitude of one volt in the antenna terminals. This ratio between the magnitude of the incoming electric field and the magnitude of the signal produced by the antenna is called the antenna factor, which is written as

$$A_F = \frac{|\mathbf{E}_{\text{in}}|}{V_{\text{ant}}}, \quad (5.11)$$

where  $A_F$  is the antenna factor,  $E_{\text{in}}$  is the incoming electric field, and  $V_{\text{ant}}$  is the magnitude of the voltage produced by the antenna.

The antenna factor can be expressed in terms of the antenna's gain through a related quantity called the effective aperture. The effective aperture defines for a given incident radiation power density ( $\text{W/m}^2$ ) the power that is received by the antenna. Therefore, the effective aperture gives the equivalent area of the antenna, which is dependent on

the gain of the antenna and the radiation wavelength in the following way,

$$A_{\text{eff}} = \frac{P_{\text{rec}}}{P_{\text{in}}} = \frac{\lambda^2}{4\pi} G, \quad (5.12)$$

where the received power is  $P_r$  and the total incoming power is  $P_{\text{in}}$ . If we express the incident power on the antenna in terms of the magnitude of the Poynting vector

$$|\mathbf{S}_{\text{in}}| = |\mathbf{E}_{\text{in}}|^2 / \eta_0, \quad (5.13)$$

where  $\eta_0$  is the impedance of free-space, which relates the magnitudes of the electric and magnetic fields in a vacuum, and is defined by

$$\eta_0 = \frac{|\mathbf{E}|}{|\mathbf{H}|} = \sqrt{\frac{\epsilon_0}{\mu_0}}. \quad (5.14)$$

The total received power by the antenna can therefore be expressed as

$$P_{\text{rec}} = |\mathbf{S}_{\text{in}}| A_{\text{eff}} = |\mathbf{S}_{\text{in}}| \frac{\lambda^2}{4\pi} G = \frac{|\mathbf{E}_{\text{in}}|^2 \lambda^2 G}{4\pi \eta_0}. \quad (5.15)$$

To relate this to the antenna factor recall that we can relate the voltage produced by the antenna to the received power with

$$P_{\text{rec}} = \frac{V_{\text{ant}}^2}{Z} = \frac{|\mathbf{E}_{\text{in}}|^2}{A_F^2 Z}, \quad (5.16)$$

where  $Z$  is the system impedance. Setting Equations 5.15 and 5.16 equal to each other, we obtain the following expression for antenna factor in terms of gain

$$A_F = \sqrt{\frac{4\pi\eta_0}{ZG\lambda^2}} = \frac{9.73}{\lambda\sqrt{G}}. \quad (5.17)$$

The second expression in Equation 5.17 is obtained by evaluating the constant terms assuming a system impedance of  $50 \Omega$ .

We have gone through the effort of expressing the antenna factor in terms of gain to highlight that the majority of antenna parameters that we care to measure for a CRES experiment can be obtained from the radiation or gain pattern of the antenna. The antenna factor is a particularly important parameter for CRES measurements due to its relevance to antenna array simulations with the Locust software [10, 13]. Specifically, Locust simulates the trajectory of an electron in a magnetic trap by running

the Kassiopeia software package [1] and then uses the Liénard-Wiechert equations to calculate the electric fields that are incident on the antenna.

To compute the response of the antenna to the electric field, Locust relies upon linear time-invariant system theory, which computes the response of the antenna (i.e. the voltage time series generated by the antenna) using a convolution between the electric field time-series and the antenna impulse response. This approach is necessary for correctly modeling the antenna response to the electric field due to the broadband and non-stationary nature of the electric fields from CRES events. Since antenna measurements take place under steady-state conditions, parameters such as the radiation pattern, gain, and antenna factor are defined in the frequency domain. However, by performing an inverse Fourier transform on the antenna factor we can obtain the antenna impulse response, which allows us to simulate CRES events in the antenna array demonstrator experiment.

## 5.2.2 Antenna Measurement Fundamentals

### 5.2.2.1 Friis Transmission Equation

The antenna factor, sometimes called the antenna transfer function, is used to model how the antenna will respond to electric fields emitted from a CRES event. Therefore, being able to measure the antenna transfer function of the antenna array is a key step in the commissioning and calibration phases of an antenna array CRES experiment. A common approach to antenna characterization is to perform a two antenna transmit-receive measurement where an antenna with a known gain is used to characterize the unknown gain of the antenna under test (see Figure 5.3).

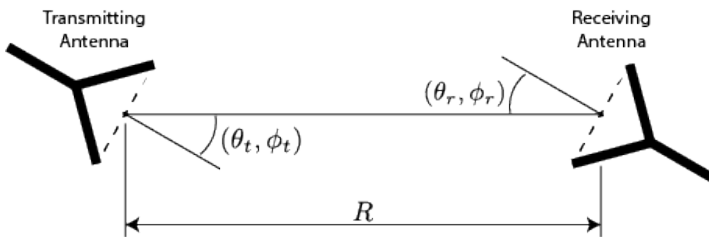


Figure 5.3: An illustration of the Friis measurement technique commonly used for antenna characterization measurements.

To analyze this two antenna setup we seek to calculate the amount of power from the transmitting antenna that we will detect with the receiving antenna. Using our understanding of antenna gain, we can calculate the power density transmitted by an

antenna in a direction  $(\theta_t, \phi_t)$  at frequency  $f$  and distance  $R$ , which is given by

$$w_t = \frac{P_t}{4\pi R^2} G_t(\theta_t, \phi_t, f). \quad (5.18)$$

Here,  $P_t$  is the total power delivered to the transmitting antenna and  $G_t(\theta_t, \phi_t, f)$  is the value of the transmitting antenna gain. The power density is the power per unit area, so to calculate the total power delivered to the receiving antenna we multiply the transmitted power density by the effective area of the receiving antenna,

$$P_r = w_t A_{eff,r} = P_t \frac{G_t(\theta_t, \phi_t, f) G_r(\theta_r, \phi_r, f) c^2}{(4\pi R f)^2}, \quad (5.19)$$

where  $G_r(\theta_r, \phi_r, f)$  is the gain of the receiving antenna. Equation 5.19 is called the Friis transmission equation, which is of fundamental importance for antenna measurements, since it allows one to measure the gain of an unknown antenna by measuring the power received from an antenna with a known gain pattern. Alternatively, if no antenna with a known gain pattern is available, two identical antennas with unknown gain patterns can be used.

### 5.2.2.2 S-Parameters and Network Analyzers

Instead of directly measuring the power received by the antenna under test, it is more common to measure the ratio of the received power to the transmitted power,

$$\frac{P_r}{P_t} = \frac{G_t(\theta_t, \phi_t, f) G_r(\theta_r, \phi_r, f) c^2}{(4\pi R f)^2}. \quad (5.20)$$

This power ratio can be easily measured using a vector network analyzer (VNA), which automates a significant fraction of the measurement process. Network analyzers are used to measure the scattering or S-parameters of a multi-port RF device, which describes how waves are scattered between the device ports. The antenna measurements we have been considering can be modeled as a two-port microwave device that we can characterize by measuring how incident voltage waves are transmitted or reflected (see Figure 5.4). We can write the scattered waves ( $V_1^-$  and  $V_2^-$ ) in terms of the incident ( $V_1^+$  and  $V_2^+$ ) waves using the scattering matrix

$$\begin{pmatrix} V_1^- \\ V_2^- \end{pmatrix} = \begin{pmatrix} S_{11} & S_{12} \\ S_{21} & S_{22} \end{pmatrix} \begin{pmatrix} V_1^+ \\ V_2^+ \end{pmatrix}, \quad (5.21)$$

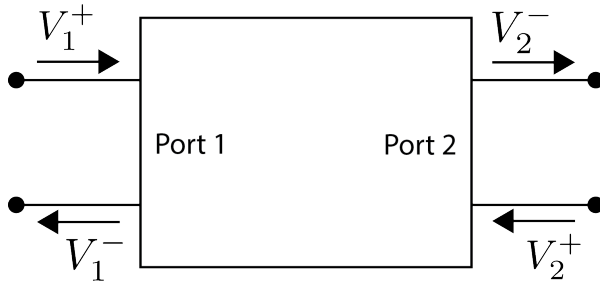


Figure 5.4: Illustration of a two-port S-parameter measurement setup. S-parameters characterize how incoming waves of voltage or power scatter off of the RF device under test. This allows you to measure important properties of the device. In particular, we can use this framework to model a two antenna radiation pattern measurement, which we can then automate using a VNA.

where the elements of the matrix are the device S-parameters. It is assumed that, when exciting the device from a particular port, that all other ports in the network are terminated at the system impedance. This ensures that the incident waves from other ports in the network are zero. Therefore, the S-parameters are the ratios between the scattered and incident waves,

$$S_{ij} = \frac{V_i^-}{V_j^+}. \quad (5.22)$$

Alternatively, S-parameters can be defined as the ratio of the scattered and incident power, which is proportional to the ratio of the squared voltage waves. Returning to our antenna measurement setup, we see that measuring the ratio of the received to the transmitted power is equivalent to measuring the ratio of power being scattered from port 1 to port 2 in a RF network. Therefore, measuring an antenna's gain can be accomplished quite easily, by using a VNA to perform a two port  $S_{21}$  measurement.

### 5.2.2.3 Antenna Array Commissioning and Calibration Measurements

Up to this point we have been discussing calibration and commissioning measurements as they apply to a single antenna. While these measurements play an important role in validating the radiation patterns of the individual array elements, the ultimate goal is to use a phased array of these antennas to do CRES, so our approach to antenna measurements applied to the whole array is potentially even more important. By measuring the gain of each individual array element we can predict the signal that antenna would during a CRES event by computing the antenna factor (see Section 5.2.1.5). However, how an array of these antennas will perform in the FSCD cannot be

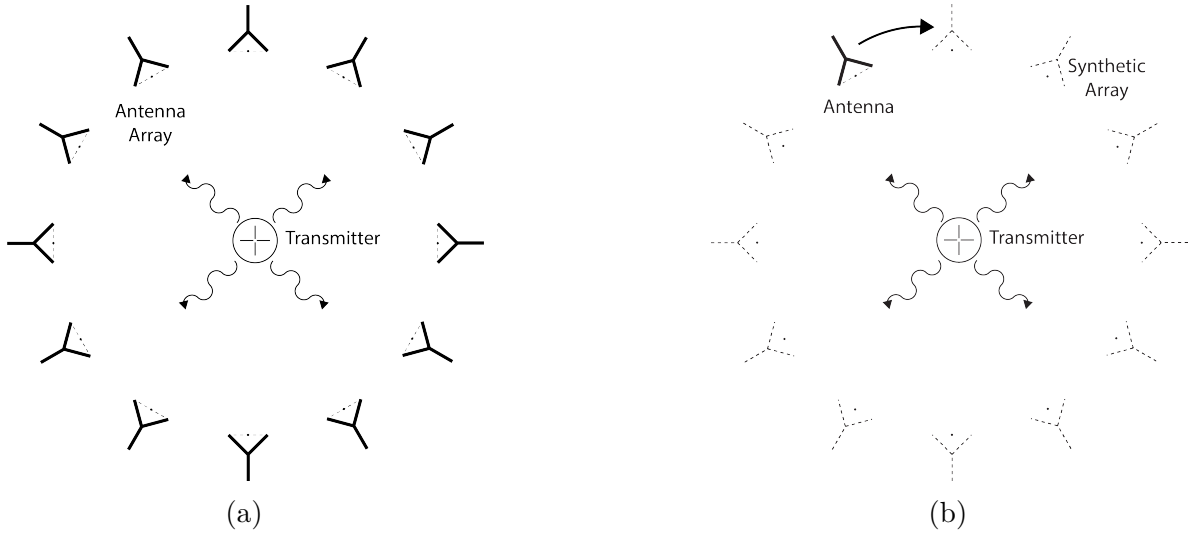


Figure 5.5: Two measurement approaches to characterizing an antenna array for CRES measurements.

calculated from the individual element radiation patterns, because we are operating in the radiative near-field. Therefore, we will need to employ both individual antenna and full-array measurements in the commissioning of the FSCD

There are two main approaches to array measurements that could be used for characterization and calibration (see Figure 5.5). One approach is to construct the complete array and use a omni-directional transmitting antenna to measure the power received by each channel in the antenna array. In Section 5.3 we describe the development of an omni-directional transmitter that also mimics the radiation phase characteristics of a CRES event, which is useful because the entire array can be tested without repositioning. Alternatively, a full antenna array can be synthesized by repeatedly moving and measuring a single array element. This approach is ideal for identifying if different channels in the antenna array are affecting each other through multi-path interference by comparing the measurement results of the synthetic array to the real array.

### 5.2.3 The Penn State Antenna Measurement System

The development of antenna array based CRES requires the capability to test and calibrate different antenna array designs to validate the performance of the as-built antenna array before and during the experiment. With these aims in mind we developed an antenna measurement system at Penn State specifically designed to mimic the characteristics of the antenna experiment designed for demonstration of the antenna array CRES technique

by the Project 8 collaboration.

The Penn State antenna measurement system utilizes a two antenna measurement configuration with a stationary reference antenna and a test antenna mounted on a set of motorized translation and rotation stages (see Figure 5.6). The antenna measurement system can be operated in two distinct modes, one focused on the characterization of the radiation patterns of prototype antennas and the other focused on the validation of data-acquisition (DAQ) and CRES signal reconstruction techniques to bridge the gap between real measurements and simulation. In both measurement configurations it is critical to isolate the antennas from the environment so that multi-path reflections do not negatively influence the measurement results. For this reason we surround the measurement volume with microwave absorber foam (AEMI AEC-1.5) specifically designed to attenuate microwave radiation near the 26 GHz measurement range of the system.

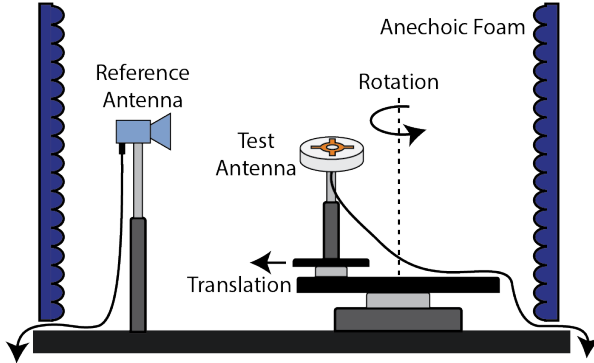


Figure 5.6: Illustration of the antenna measurement system developed for the Project 8 Collaboration. The reference and test antennas can be connected to different data acquisition configurations depending on the measurement goals.

In the first measurement configuration the reference antenna is typically a well-characterized horn antenna as pictured, since horn antennas have well-known and stable radiation patterns making them ideal as standard references. For characterization measurements, the test antenna represents the antenna-under-test whose pattern we wish to characterize. Mounting the test antenna on motorized rotation and translation stages allows us to automate the procedure significantly speeding up the radiation pattern measurement process.

In the second measurement configuration we are interested in recreating the conditions of an antenna array CRES experiment as it concerns the antenna array and DAQ system as an intermediate step towards building the full experiment. In this configuration, the

reference antenna is a prototype antenna which will be used to construct the antenna array in the FSCD experiment, and the test antenna is a specially designed synthetic cyclotron antenna (SYNCA) as picture in Figure 5.6. The SYNCA is designed such that the radiation pattern mimics that of a CRES electron so that the signals received by the prototype CRES array antenna mimic what is expected for a real CRES experiment.

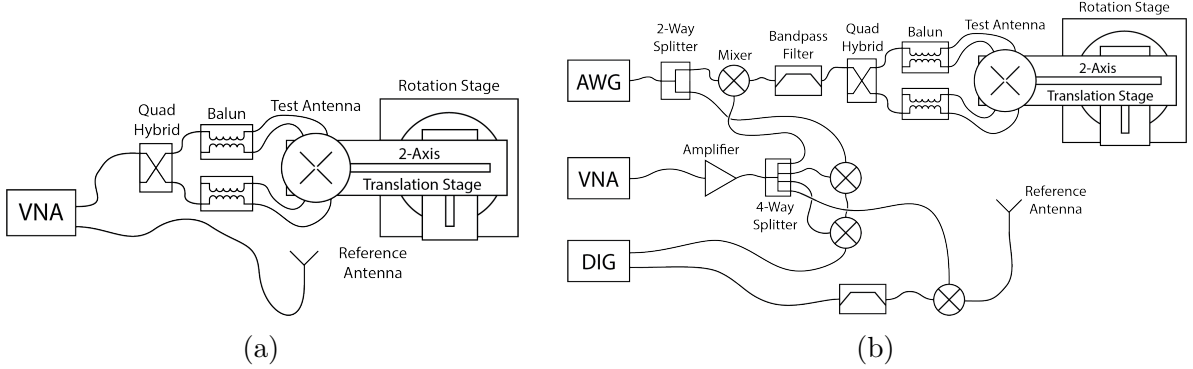


Figure 5.7: Diagrams of two measurement system configurations. Configuration (a) utilizes a VNA and is more suited to antenna characterization. Configuration (b) utilizes an AWG and VNA as a signal generation system and digitizer to collect measurement data, which is more suited to simulating CRES measurements. The transmission chain utilizes a quadrature hybrid and a pair of baluns to drive the cross-dipole variant test antenna developed for synthetic CRES measurements.

In Figure 5.7 we show two high-level system diagrams of the Penn State antenna measurement system that depict the important system components and the connections between them. The two configurations of the measurement system utilize slightly different hardware corresponding to the goals of the measurement. For characterization and radiation pattern measurements, we are mostly likely to use the configuration shown in Figure 5.7a. In this case a vector network analyzer (VNA) is used as both the transmission source and data acquisition system and it is relatively easy to calibrate over a wide range of frequencies. Whereas, if we are more interested in recreating what would take place in the FSCD experiment we would probably use the configuration shown in Figure 5.7b, since this system effectively mimics the receiver chain envisioned for the FSCD experiment.

In the characterization configuration the Penn State measurement system utilizes a network analyzer (Keysight N5222A ) with two independent sources and four measurement ports as the primary measurement tool. To one of the measurement ports, we connect a standard reference antenna (typically a Pasternack PF9851 horn antenna), and to a different port we connect the test antenna that we are attempting to characterize. In the

measurement shown the test antenna represents a SYNCA antenna, which requires a transmission chain consisting of quadrature hybrid coupler (Marki QH-0226) connected to two baluns (Marki BAL-0026) in order to operate. The purpose of these components will be explained in more detail in Section 5.3, since they are generally considered to be a part of the SYNCA rather than the measurement system. With the antennas connected to two ports the VNA measures the radiation pattern by performing a transmission S-parameter measurement, which can be used with the knowledge of the reference antenna's radiation pattern to determine the radiation pattern of the test antenna (see Section 5.2.1).

The second configuration is slightly more complicated and incorporates more hardware components in order to more closely mimic the DAQ system envisioned for the FSCD experiment. The basic approach is to produce CRES-like radiation and use an antenna combined with an RF receiver chain to acquire the signals. On the transmit side, an arbitrary waveform generator (AWG, RIGOL DG5252) is used to generate a waveform that mimics a CRES signal at a baseband frequency up to 250 MHz. This frequency is then up-converted to the CRES signal frequency band of 25.8 to 26.0 GHz using a mixer (Marki MM1-0832L) and a bandpass filter (K&L Microwave 3C62-25900/T200-K/K) to reject unwanted mixing components outside out of the 200 MHz CRES signal band. The local oscillator signal for mixing is provided by one of the VNA sources configured to run in a continuous wave setting. On the receive side, a prototype antenna is used to received the radiation emitted by the test antennas, which is down-converted and filtered using the same mixer and bandpass filter as the transmission chain. Lastly, data acquisition is performed using a 14-bit digitizer sampling at 500 MSa/s (CAEN DT530) on the down-converted signals.

In order to distribute the LO to all of the mixers in the system a 4-way power splitter (MiniCircuits ZC4PD-18263-S+) along with an amplifier (Marki APM-6848) is used to drive the four mixers used in the measurement system. A limitation of using the VNA as an LO source is that there is no control of the LO phase when a measurement is triggered by the control script, which leads to a random phase offset between acquisitions making analysis of the data impossible. In order to monitor the random phase of the LO, we use a 2-way power splitter (MiniCircuits Z99SC-62-S+) is used to split the signal from the AWG between the transmission path and a LO monitoring path. The LO monitoring path consists of an up-conversion and down conversion using two mixers connected by a coaxial cable, and we monitor the relative phase of the LO by using a channel on the digitizer to sample this path. A phase shift in the LO will lead to a proportional phase shift in the mixed signal, which we can measure and remove from datasets consisting of

a series of separate acquisitions.

The test antenna is mounted on a set of motorized stages, which are identical for both measurement configurations. We use a rotational stage (ThorLabs PRMTZ8) as the base layer and mount additional movement stages and the test antenna on top of this. The rotational stage is ideal for measuring a complete azimuthal scan of the test antenna's radiation pattern as well as for moving a SYNCA antenna in circular motion to recreate the symmetry of the FSCD antenna array. On top of the rotational stage we mount two linear translation stages (ThorLabs MTS50-Z8 and MTS25-Z8) in a cross-wise manner so that we can move the test antenna along two perpendicular axes. Using the linear stages in combination with the rotational stage allows us to fine-tune the positioning of the test antenna so that it can be perfectly aligned with the axis of the rotation stage. To control the movement of the test antenna as well as the VNA or DAQ hardware we developed a LabView script that automates the measurement of a full 360° radiation pattern and saves the data to cloud storage for offsite analysis.

## 5.3 Development of a Synthetic Cyclotron Antenna (SYNCA) for Antenna Array Calibration

This section is the manuscript of the publication [11] detailing the development of a Synthetic Cyclotron Antenna (SYNCA) for antenna array characterization measurements by the Project 8 collaboration.

### 5.3.1 Introduction

Neutrinos are the most abundant standard model fermions in our universe, but due to weak interaction cross-sections with other particles, neutrinos are particularly difficult to study. Consequently, many fundamental properties of neutrinos are still unknown including the absolute scale of the neutrino mass [18]. Direct, kinematic measurements of the neutrino mass are particularly valuable due to their model independent nature [19]. To date the most sensitive direct neutrino mass measurements have been performed by the KATRIN collaboration [20], which measures the molecular tritium  $\beta$ -decay spectrum to infer the neutrino mass. Current data from neutrino oscillation measurements [18] allow for neutrino masses significantly smaller than the design sensitivity of the KATRIN experiment; therefore, there is a need for new technologies for performing direct neutrino mass measurements to probe lower neutrino masses.

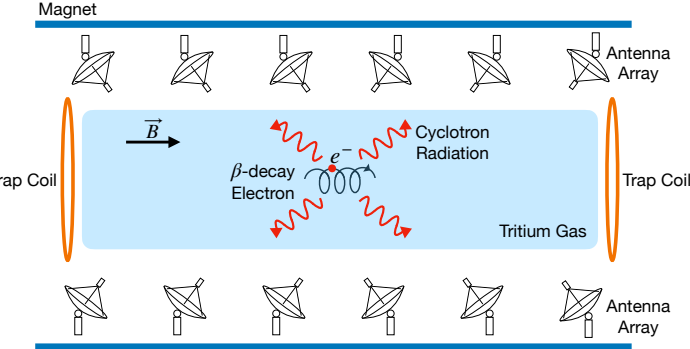


Figure 5.8: A sketch of an antenna array large-volume CRES experiment. Electrons from  $\beta$ -decays are confined in a magnetic field using a set of trap coils. The cyclotron radiation produced by the motion of the trapped electrons can be detected by a surrounding antenna array to determine the electron energies. Measuring the energies of many electrons produces a  $\beta$ -decay spectrum.

The Project 8 collaboration is developing new methods for neutrino mass measurement based on Cyclotron Radiation Emission Spectroscopy (CRES) [21–24], with the goal of measuring the absolute scale of the neutrino mass with a  $40 \text{ meV}/c^2$  sensitivity [19, 25]. This sensitivity goal will require the development of two separate technical capabilities. First is the development of an atomic tritium source, which avoids significant spectral broadening due to molecular final states [26]. Second is the technology for performing CRES in a multi-cubic-meter experimental volume with high combined detection and reconstruction efficiency, which is required in order to obtain sufficient event statistics near the tritium spectrum endpoint.

One approach for a large-volume CRES experiment is to use an array of antennas, which surrounds a volume of tritium gas, to detect the cyclotron radiation produced by the  $\beta$ -decay electrons when they are trapped in a background magnetic field using a set of magnetic trapping coils (see Figure 5.8). Project 8 has developed a conceptual experiment design to study the feasibility of this approach. The design consists of a single circular array of antennas with a radius of 10 cm and 60 independent channels positioned around the center of the magnetic trap. The motivation behind this antenna array design is to first develop an understanding of the antenna array approach to CRES with a small scale experiment before attempting to scale the technique to large volumes by using multiple antenna rings to construct the full cylindrical array. The development of the antenna array approach to CRES has largely proceeded through simulations using the Locust software package [10, 27], which is used to model the fields emitted by CRES events and predict the signals received by the surrounding antenna array. To validate

these simulations, a dedicated test stand is being constructed to perform characterization measurements of the prototype antenna array developed by Project 8 (see Figure 5.9) and benchmark signal reconstruction methods using a specially designed transmitting calibration probe antenna.

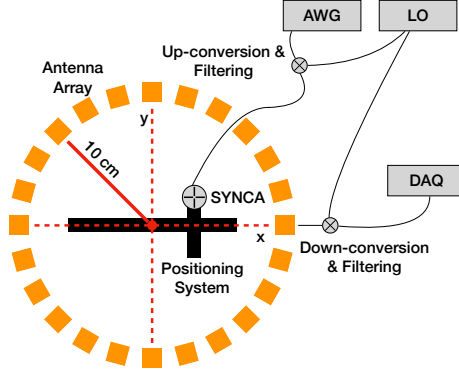


Figure 5.9: A schematic of the antenna array test stand. The circular antenna array has a radius of 10 cm with 60 independent channels (limited number shown for clarity). The test stand includes an arbitrary waveform generator (AWG), local oscillator (LO), and data acquisition (DAQ) hardware. Finally, a specialized Synthetic Cyclotron Antenna (SYNCA) is used to inject signals to test the antenna array.

We call this probe antenna the Synthetic Cyclotron Antenna or SYNCA. The SYNCA is a novel antenna design that mimics the cyclotron radiation generated by individual charged particles trapped in a magnetic field, which will be used in the antenna test stand to perform characterization measurements, simulation validation, and reconstruction benchmarking. This paper provides an overview of the design, construction, and characterization measurements of the SYNCA performed in preparation for its usage as a transmitting calibration probe.

In Section 5.3.2 we provide a description of the cyclotron radiation field characteristics that we recreate with the SYNCA. In Section 5.3.3 we give an overview of the simulations performed to develop an antenna design that mimics the characteristics of cyclotron radiation. In Section 5.3.4 we outline characterization measurements to validate that the fields generated by the SYNCA match simulation, and finally in Section 5.3.5 we demonstrate an application of the SYNCA to test phased array reconstruction techniques on the bench-top.

### 5.3.2 Cyclotron Radiation Phenomenology

To understand the cyclotron radiation phenomenology that the SYNCA should mimic, we consider a charged particle moving at relativistic speed in the presence of an external magnetic field (see Figure 5.10). In the special case we shall examine, the entirety of the electron's momentum is directed perpendicular to the magnetic field; therefore, the trajectory of the electron is confined to the cyclotron orbit plane. Because the momentum vector is oriented perpendicular to the magnetic field, electrons with these trajectories are said to have pitch angles of 90°.

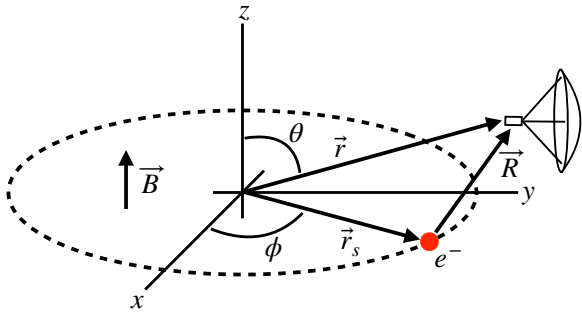


Figure 5.10: An electron (red dot) performing cyclotron motion in the x-y plane. The resulting cyclotron radiation is observed by an antenna located at the field point of interest.

The cyclotron radiation fields generated by this circular trajectory are those which we aim to reproduce with the SYNCA. We can describe the electromagnetic (EM) fields using the Liénard-Wiechert equations [10, 28], which in non-covariant form express the electric field as

$$\vec{E} = e \left[ \frac{\hat{n} - \vec{\beta}}{\gamma^2(1 - \vec{\beta} \cdot \hat{n})^3 |\vec{R}|^2} \right]_{t_r} + \frac{e}{c} \left[ \frac{\hat{n} \times [(\hat{n} - \vec{\beta}) \times \dot{\vec{\beta}}]}{(1 - \vec{\beta} \cdot \hat{n})^3 |\vec{R}|} \right]_{t_r}, \quad (5.23)$$

where  $e$  is the particle's charge,  $\hat{n} = (\vec{r} - \vec{r}_s)/|\vec{r} - \vec{r}_s|$  is the unit vector pointing from the electron to the field measurement point,  $\vec{\beta} = \dot{\vec{r}}_s/c$  is the velocity of the particle divided by the speed of light, and  $\gamma$  is the relativistic Lorentz factor. The equation is meant to be evaluated at the retarded time as indicated by  $t_r = t - |\vec{R}|/c$ , which accounts for the time delay due to the finite speed of light between the point where the field was emitted and the point where the field is detected.

We would like to simplify Equation 5.23 it at all possible. As a first step we analyze the relative magnitudes of the electric field polarization components. Consider an electron

following a circular cyclotron orbit in a uniform magnetic field whose guiding center is positioned at the origin of the coordinate system. The equation of motion can be expressed as

$$\vec{r}_s = (r_c \cos \omega_c t_r) \hat{x} + (r_c \sin \omega_c t_r) \hat{y}. \quad (5.24)$$

For single antenna located along the  $y$ -axis at position  $\vec{r} = r_a \hat{y}$  we are interested in the incident electric fields from the electron. The electric field is given by Equation 5.23, which we evaluate in the regime where  $r_a \gg r_c$ . This limit can be justified by comparing the radius of the cyclotron orbit for an electron with the tritium beta-spectrum endpoint energy of 18.6 keV in a 1 T magnetic field to the typical ( $r_a \simeq 100$  mm) radial position of the receiving antenna. We find that the cyclotron orbit has a radius of 0.46 mm which is approximately a factor of 200 smaller than the typical antenna radial position. In this regime we can make the approximation  $\vec{R} \simeq r_a \hat{y}$  and the expression for the electric field at the antenna's position becomes

$$\vec{E} = \frac{e}{\gamma^2 r_a^2} \frac{\hat{x} \left( \frac{r_c \omega_c}{c} \sin \omega_c t_r \right) + \hat{y} \left( 1 - \frac{r_c \omega_c}{c} \cos \omega_c t_r \right)}{(1 - \frac{r_c \omega_c}{c} \cos \omega_c t_r)^3} - \frac{e}{c r_a} \frac{\hat{x} \left( \frac{r_c^2 \omega_c^3}{c^2} - \frac{r_c \omega_c^2}{c} \cos \omega_c t_r \right)}{(1 - \frac{r_c \omega_c}{c} \cos \omega_c t_r)^3}. \quad (5.25)$$

Since the receiving antenna is part of a circular array of antennas, it is useful to rewrite Equation 5.25 in terms of the azimuthal ( $\hat{\phi}$ ) and radial ( $\hat{r}$ ) polarizations. Making use of the fact that for an antenna located at  $R = r_a \hat{y}$  that  $\hat{\phi} = -\hat{x}$  and  $\hat{r} = \hat{y}$  we find

$$\vec{E} = \hat{\phi} E_\phi + \hat{r} E_r \quad (5.26)$$

$$E_\phi = \frac{e}{(1 - \frac{r_c \omega_c}{c} \cos \omega_c t_r)^3} \left[ -\frac{\frac{r_c \omega_c}{c} \sin \omega_c t_r}{\gamma^2 r_a^2} + \frac{\omega_c \left( \frac{r_c^2 \omega_c^2}{c^2} - \frac{r_c \omega_c}{c} \cos \omega_c t_r \right)}{c r_a} \right] \quad (5.27)$$

$$E_r = \frac{e \left( 1 - \frac{r_c \omega_c}{c} \sin \omega_c t_r \right)}{\gamma^2 r_a^2 (1 - \frac{r_c \omega_c}{c} \cos \omega_c t_r)^3}. \quad (5.28)$$

For the purposes of designing a synthetic cyclotron radiation antenna we are interested in the dominant electric field polarization emitted by the electron. The antenna is being designed to mimic the cyclotron radiation produced by electrons with kinetic energies of approximately 18.6 keV in a 1 T magnetic field [26]. Since the relativistic beta factor for an electron with this kinetic energy is  $|\vec{\beta}| \simeq \frac{1}{4}$ , the approximations  $\gamma \simeq 1$  and  $\frac{r_c \omega_c}{c} \simeq \frac{1}{4}$  are justified. Inserting these expressions into the equations for the electric field components above simplifies the comparison of the magnitudes of the two components. Additionally, we compare the time-averaged magnitudes to evaluate the root mean squared electric

field ratio. The time-averaged ratio of the radial and azimuthally polarized electric fields with the above simplifications is given by

$$\frac{\langle |E_r| \rangle}{\langle |E_\phi| \rangle} = \frac{8 - \sqrt{2}}{\left| 1 - \frac{r_a}{r_c} \frac{1-2\sqrt{2}}{8} \right|} \simeq \frac{r_c}{r_a} \frac{8(8 - \sqrt{2})}{2\sqrt{2} - 1} = 0.13, \quad (5.29)$$

where we have made use of the fact that for these magnetic fields and kinetic energies the cyclotron radius is much smaller than the radius of the antenna array.

From Equation 5.29 we see that the time-averaged azimuthal polarization is larger than the radial polarization by about a factor of 8, which makes it the dominant contribution to the electric fields at the position of the antenna. We must also consider the directivity of the receiving antenna which can have a gain that is disproportionately large for a specific polarization component. Because the  $E_\phi$  component is dominant, the receiving antenna array is designed with an azimuthal polarization, which negates the voltages induced in the antenna from the radially polarized fields. Therefore, we conclude that for the purpose of designing the SYNCA antenna it is acceptable to approximate the electric fields from Equation 5.23 as purely azimuthally or  $\phi$ -polarized. The simplified expression for the electric field received by an antenna becomes

$$\vec{E} = E_\phi \hat{\phi} = \frac{e \frac{r_c \omega_c}{c}}{4r_a r_c} \left[ \frac{\frac{r_c \omega_c}{c} - \cos \omega_c t - \frac{4r_c}{r_a} \sin \omega_c t}{(1 - \frac{r_c \omega_c}{c} \cos \omega_c t)^3} \right]_{t_r} \hat{\phi}, \quad (5.30)$$

where the radius of the cyclotron orbit is called  $r_c$ , the cyclotron frequency is called  $\omega_c$ , and the radial position of the receiving antenna is called  $r_a$ . Equation 5.30 has been evaluated in the non-relativistic limit where  $\gamma \simeq 1$ , which is justified by the fact that  $|\vec{\beta}| \simeq \frac{c}{4}$  for an electron with an 18.6 keV kinetic energy in a 1 T magnetic field.

This rather complicated expression can be simplified using Fourier analysis. Assuming a background magnetic field of 1 T and a kinetic energy of 18.6 keV we calculate numerically the electric field using Equation 5.30 and apply a discrete Fourier Transform to visualize the frequency spectrum (see Figure 5.11).

We observe that the azimuthally polarized electric field is periodic with a base cyclotron frequency of 25.898 GHz corresponding to the highest power frequency component in Figure 5.11. The frequency spectrum reveals that the signal is composed of a constant term with zero frequency and a series of harmonics separated by 25.898 GHz. Therefore, we can represent the azimuthal electric fields from the electron as a linear combination of pure sinusoids with frequencies given by  $\omega_k = k\omega_c$  ( $k \in 0, 1, 2, \dots$ ) and amplitudes

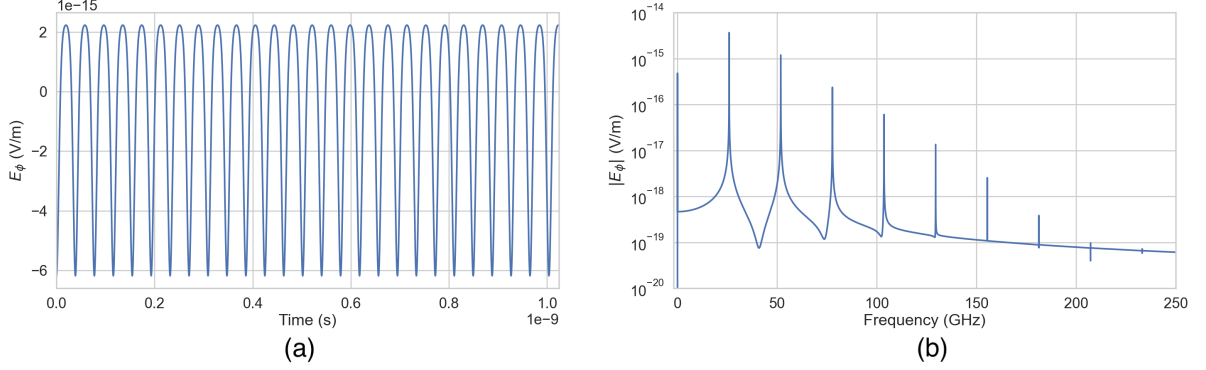


Figure 5.11: A plot of the numeric solution to Equation 5.31. The time-domain representation of the signal (a) is composed of a zero frequency term and a series of harmonics separated by the main cyclotron frequency as shown in the plot of the frequency spectrum (b). We can see that the relative amplitude of the harmonics beyond  $k = 7$  are smaller than the main carrier by a factor of about  $10^{-5}$  and are completely negligible.

extracted from the Fourier representation. Using this representation we can transform the equation for the azimuthally polarized electric fields in Equation 5.30 into

$$E_\phi = \frac{e \frac{r_c \omega_c}{c}}{4r_a r_c} \sum_{k=0}^7 A_k e^{i\omega_k t_r}, \quad (5.31)$$

where we have truncated the sum over harmonics at the 7th order for completeness. The amplitudes  $A_k$  are dimensionless complex numbers, which encode the relative powers of the harmonics as well as the starting overall phase of the cyclotron radiation. Because magnitude of the relative amplitudes exponentially decreases for higher harmonics, it is usually sufficient to consider only the terms up to  $k = 4$  where the relative amplitude of the harmonics has decreased from the main carrier by a factor of approximately 100. However, for completeness we include harmonics up to 7th order in Equation 5.31. The range of frequencies to which the receiving antenna array in the antenna test stand is sensitive is defined by the antenna's transfer function. The receptive bandwidth for the antennas used in the test stand is a range of frequencies with a bandwidth on the order of a few GHz centered around the main cyclotron carrier frequency of 25.898 GHz. Therefore, the higher order harmonics as well as the zero frequency term can be ignored when considering only the signals that will be received by the antenna array.

Considering only the 1st order harmonic term from Equation 5.31, which represents the portion of the electric field that will be detected by the array, and evaluating this at

the retarded time we obtain the following for the  $\phi$ -polarized electric fields

$$E_\phi \propto \cos \left( \omega_c \left( t - |\vec{R}|/c \right) - \Delta \right), \quad (5.32)$$

where the arbitrary phase  $\Delta$  is defined by  $A_k = |A_k|e^{i\Delta}$ . We are interested in the characteristics of the amplitude of the electric field as a function of the radial distance component ( $|\vec{R}|$ ) of the retarded time. In particular, the maximum of  $E_\phi$  occurs when the argument of the cosine function is equal  $n\pi$  where  $n \in \{0, \pm 2, \pm 4, \dots\}$ ; however, the solutions where  $n$  is negative can be discarded since they represent unphysical negative overall phases. Applying this condition to Equation 5.32 gives a condition on the radial position of the maximum of  $E_\phi$

$$\omega_c(t - |\vec{R}|/c) - \Delta = n\pi, \quad (5.33a)$$

$$|\vec{R}| = \frac{c}{\omega_c} ((\omega_c t - \Delta) - n\pi), \quad (5.33b)$$

which is a function of time in the frame of the moving electron ( $t$ ). Equation 5.33 can be further simplified by noticing that the azimuthal position of the electron ( $\phi_e(t)$ ) as a function of time is defined by  $\phi_e(t) = \omega_c t - \Delta$  which reduces Equation 5.33 to

$$|\vec{R}| = \frac{c}{\omega_c} (\phi_e(t) - n\pi). \quad (5.34)$$

Equation 5.34 represents an archimedean spiral which is formed when plotting the amplitude of  $E_\phi$  in the x-y plane. The solution where  $n = 0$  represents the leading edge of the radiation spiral which propagates outward from the electron at the speed of light. The additional solutions for  $n > 0$  represent the persistent spiral at radii inside the leading edge of the radiated fields that have not yet been detected by the receiver at the current time. In Figure 5.12a we show the expected spiral pattern for the maxima of the cyclotron radiation.

In particular, we note that for the circular array geometry of the test stand, depicted as the series of circles in Figure 5.12a, each antenna receives a linearly polarized wave with a phase offset that corresponds to the azimuthal angle for that antenna element. Therefore, as we show in Figure 5.12b, when the relative phase of the received signal is plotted as a function of the receiving antenna's azimuthal position the result is also an Archimedean spiral.

Based on these analytical calculations we can characterize the magnitude, polarization, and phase of the signals received by the antenna array using three criteria. These criteria

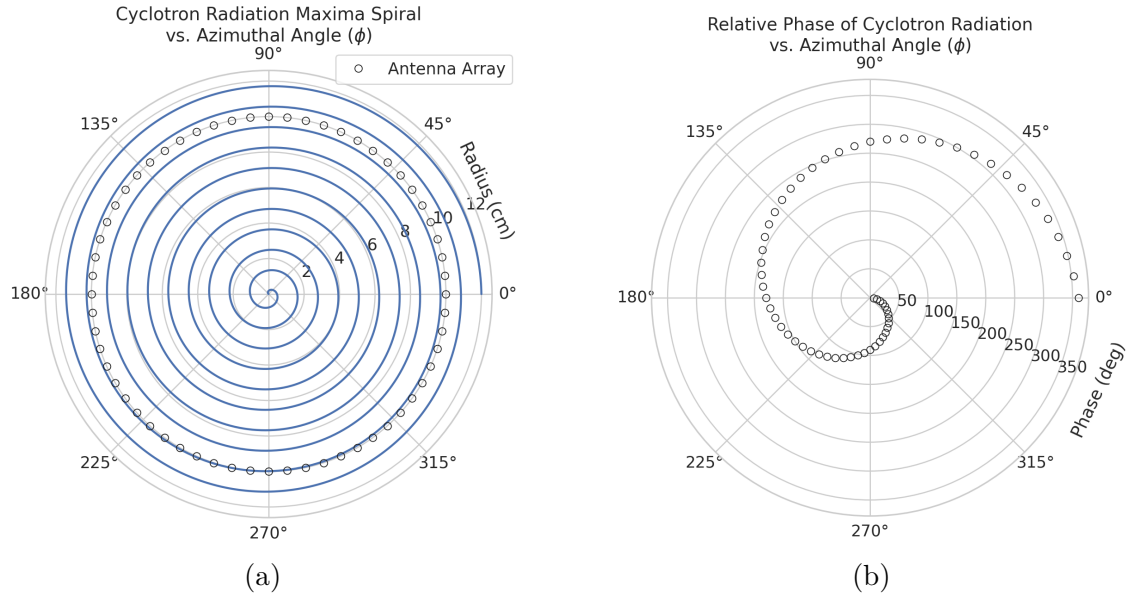


Figure 5.12: The amplitude maxima of the cyclotron radiation form an Archimedean spiral as the radiation propagates outward from the cyclotron orbit center (a). A circular antenna array located at a fixed radius from the orbit center will receive electric fields with equal magnitude in each of its channels, but the phase of the electric field incident on each array channel will be linearly out of phase from its neighbor antennas by an amount equal to the angular separation of the two channels (b).

are the basis of comparison for the radiation produced by the SYNCA and cyclotron radiation emitted by electrons and will be used to evaluate the performance of antenna designs. The criteria are:

1. Electric fields that are  $\phi$ -polarized near  $\theta = 90^\circ$
2. Uniform time-averaged electric field magnitudes around the circumference of a circle centered on the antenna
3. Electric fields whose phase is equal to the azimuthal angle at the point of measurement plus a constant

The Locust simulation package [27] can be used to directly simulate the EM fields generated by electrons performing cyclotron motion to validate the analytical calculations. Locust simulates the EM fields by first calculating the trajectory of the electrons in the magnetic trap using the Kassiopeia software package [29]. The trajectory can then be used to solve for the EM fields using the Liénard-Wiechert equations directly with no approximations. The resulting electric field solutions drive a receiving antenna by

convolving the time-domain fields with the finite-impulse response filter of the antenna or they can be examined directly to study the field characteristics that the SYNCA must reproduce. In the next section we compare the radiation field patterns for electrons simulated with Locust to patterns from a SYNCA antenna design.

### 5.3.3 SYNCA Simulations and Design

One potential SYNCA design is the crossed-dipole antenna [30]. A crossed-dipole antenna consists of two dipole antennas, one of which is rotated 90° with respect to the other, which are fed with signals that are out of phase from the opposite dipole by 90° (see Figure 5.13). This arrangement causes the signals fed to each arm of the dipole to be

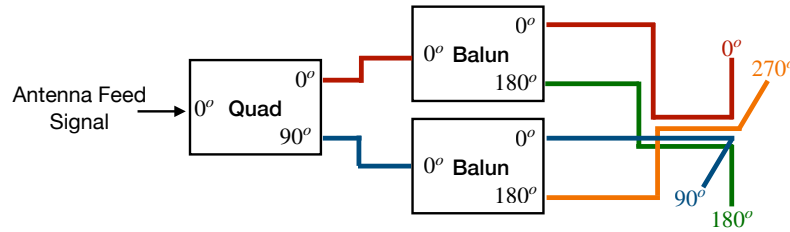


Figure 5.13: An idealized crossed-dipole antenna consists of two electric dipole antennas oriented perpendicular to each other and is fed with four signals with a quadrature phase relationship. An example antenna feed circuit is shown which is composed of a chained combination of a quadrature hybrid-coupler (Quad) and two baluns.

out of phase from each of the neighboring arms by 90°, which mirrors the spatial phase relationship of cyclotron radiation fields.

A potential drawback of this design is that standard crossed-dipole antennas do not radiate uniform electric fields near the  $\theta = \pi/2$  plane. Typical crossed-dipole antennas use dipole arm lengths equal to  $\lambda/4$  or larger [30], where  $\lambda$  is the wavelength at the desired operating frequency. Such large arm lengths cause the electric field magnitude to vary significantly around the circumference of the antenna. However, making the antenna electrically small by shrinking the arm length can improve the antenna pattern uniformity.

In general, the criterion for an electrically small antenna is that the largest dimension of the antenna ( $D$ ) obey  $D \lesssim \lambda/10$  [31]. In our application, we are attempting to mimic the cyclotron radiation emitted by electrons produced from tritium  $\beta$ -decay with energies near the spectrum endpoint. For a background magnetic field of 1 T, the corresponding

cyclotron frequency of tritium endpoint electrons is approximately 26 GHz. Therefore, the electrically small condition would require that the largest dimension of the crossed-dipole antenna be smaller than 1.2 mm.

A crossed-dipole antenna with an overall size of 1.2 mm is challenging to fabricate due to the small dimensions of the dipole arms that, in practice, are fragile and unsuitable for use as a calibration probe. To mitigate some of the challenges with the fabrication of such a small antenna, a variant crossed-dipole antenna design using printed circuit board (PCB) technology (see Figure 5.14) was developed in partnership with an antenna prototyping company, Field Theory Consulting <sup>1</sup>.

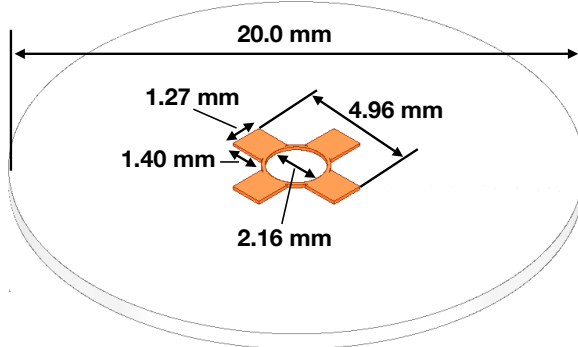


Figure 5.14: A model of the PCB crossed-dipole antenna with dimensions. The design has an inside diameter of 2.16 mm for the central circular trace, which is 0.13 mm wide. The dipole arms each have a width of 1.27 mm and protrude beyond the circular trace by 1.40 mm, which gives an overall width of 4.96 mm for the length of the antenna PCB trace from end-to-end. The overall size of the antenna is 20.0 mm the majority of which is the PCB dielectric material. This design was observed in simulation to maintain the field characteristics of the idealized crossed-dipole while being simpler to fabricate due to the increased size of the antenna.

The PCB crossed-dipole design uses four rectangular pads to represent the dipole arms, which are connected by a thin circular trace. The circular trace both adds mechanical stability to the antenna and improves the azimuthal uniformity of the electric fields compared to a more standard crossed-dipole geometry. Furthermore, the circular trace allows for a greater separation between dipole arms than standard crossed-dipoles, which is required to accommodate the coaxial connections to each pad. The pads each contain a through-hole solder joint to connect coaxial transmission lines using hand soldering. The antenna PCB has no ground plane on the bottom layer as this was observed in simulation to significantly distort the radiation pattern in the plane of the PCB. The

---

<sup>1</sup><https://fieldtheoryinc.com/>

only ground planes present in the model are the outer conductors of the four coaxial transmission lines which feed the antenna. These are left unterminated on the bottom of the PCB dielectric material.

The antenna design development utilized a combination of Locust electron simulations and antenna simulations using ANSYS HFSS [32], a commercial finite-element electromagnetic simulation software. Two antenna designs were simulated: an idealized electrically small crossed-dipole antenna with an arm length of 0.40 mm and an arm separation of 0.05 mm, as well as a PCB crossed-dipole antenna with the dimensions shown in Figure 5.14. Plotting the magnitude of the electric fields generated by the antennas across a 10 cm square located in the same plane as the respective antennas reveals the expected cyclotron spiral pattern (see Figure 5.15) which closely matches the prediction for simulated electrons. The spiral pattern demonstrates that the electric fields have the appropriate phases to mimic cyclotron radiation, which fulfills SYNCA criterion 3 identified in Section 5.3.2.

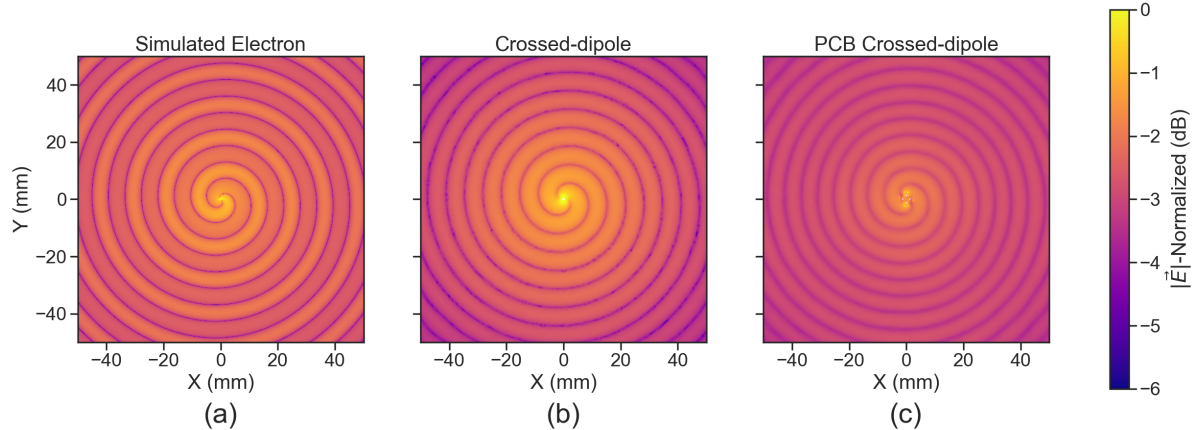


Figure 5.15: A comparison of the electric field magnitudes, normalized by the maximum value of the electric field in each simulation, plotted on a 10 cm square to visualize the Archimedean spirals formed by the electron (a), the crossed-dipole antenna (b), and a PCB crossed-dipole antenna (c). The matching patterns indicate that the electric fields have similar phase characteristics. These images were generated using Locust simulations for the electron and ANSYS HFSS for both antennas.

As we can see from Figure 5.16, the crossed-dipole antenna, which uses an idealized geometry, exhibits good agreement with simulation. The antenna has a maximum deviation from a simulated electron of approximately 0.5 dB in the total electric field, 1 dB for the  $\phi$ -polarized electric field and 1 dB for the  $\theta$ -polarized electric field.

In comparison, the pattern of the PCB crossed-dipole antenna, because the simulation

incorporates the geometry of the coax transmission lines, exhibits some distortion from the idealized cross-dipole simulations. The vertically oriented ground planes of the coax lines introduce more  $\theta$ -polarized electric fields than are observed for simulated electrons near  $\theta = 90^\circ$ . The significant  $\theta$ -polarized field minimum is still present but shifted to approximately  $\theta = 65^\circ$ . The  $\theta$ -polarized field deviations of the PCB crossed-dipole

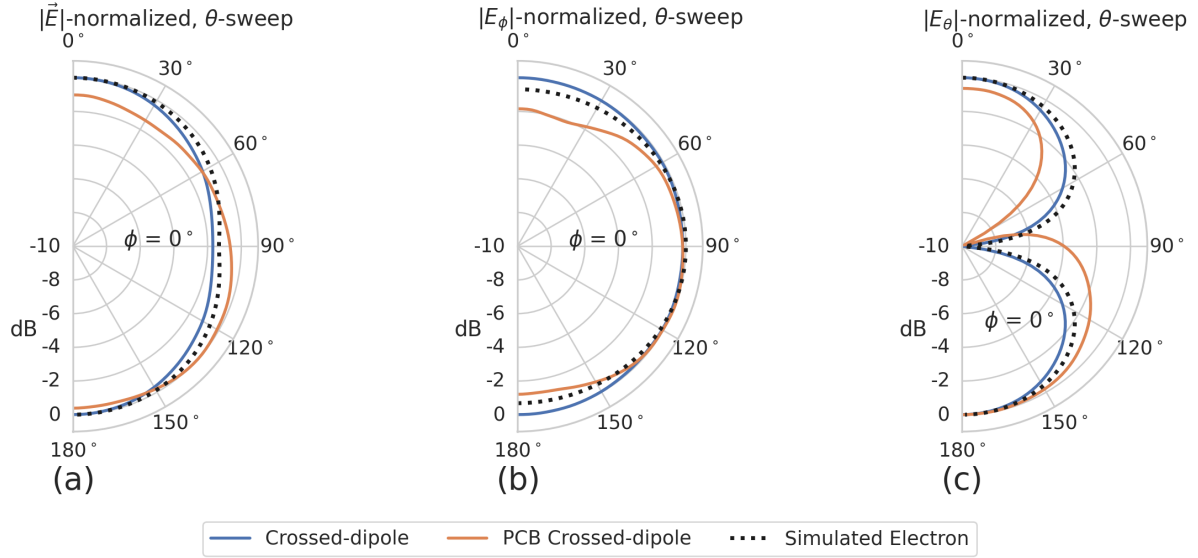


Figure 5.16: A comparison of the normalized electric field magnitudes for the ideal crossed-dipole, PCB crossed-dipole, and a simulated electron as a function of the polar angle ( $\theta$ ). (a) Shows the total electric field, (b) shows the  $\phi$ -polarized electric field component, and (c) shows the  $\theta$ -polarized electric field component. These images were generated using Locust simulations for the electron and ANSYS HFSS for both antennas.

antenna should not greatly impact the performance of the antenna because the receiving antenna array is primarily  $\phi$ -polarized. Therefore deviations in the  $\theta$ -polarized fields will be suppressed due to the polarization mismatch. More importantly, the  $\phi$ -polarized electric field pattern generated by the PCB crossed-dipole closely matches simulated electrons across the polar angle range of  $50^\circ < \theta < 150^\circ$ . In this region the PCB crossed-dipole differs by less than 0.5 dB from simulated electrons. This range greatly exceeds the beamwidth of the receiving antenna array which is designed to be most sensitive to fields produced near  $\theta = 90^\circ$ . Therefore, we conclude that the PCB crossed-dipole antenna generates a  $\phi$ -polarized radiation pattern that fulfills SYNCA criterion 1 from Section 5.3.2.

The final SYNCA criterion is related to the uniformity of the electric fields when measured azimuthally around the antenna. As we saw for real electrons in Section 5.3.2 it is expected that the magnitude of the electric field be completely uniform as a function

of the azimuthal angle due to the symmetry of the cyclotron orbit. In Figure 5.17 we plot the total electric field as a function of azimuthal angle for an electron, the crossed-dipole antenna, and the PCB crossed-dipole antenna. The crossed-dipole antenna exhibits

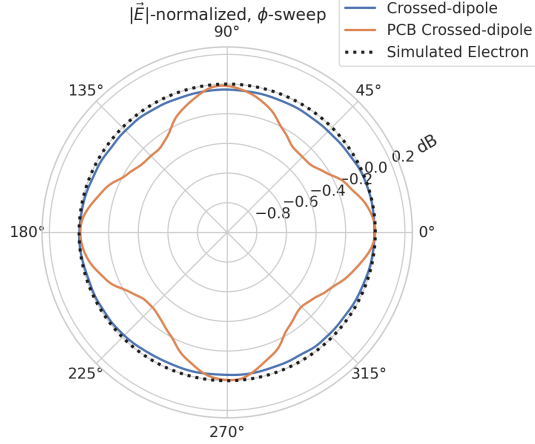


Figure 5.17: A comparison of the normalized electric field magnitudes for the crossed-dipole, PCB crossed-dipole, and a simulated electron as a function of the azimuthal angle ( $\phi$ ) evaluated at  $\theta = 90^\circ$ . This image was generated using Locust simulations for the electron and ANSYS HFSS for both antennas.

perfect uniformity around the azimuthal angle, whereas the PCB crossed-dipole has a small periodic deviation with a maximum difference of 0.3 dB caused by the coaxial transmission lines below the PCB. Such a small deviation from uniformity is acceptable since it is smaller than the expected variation in uniformity caused by imperfections in the antenna fabrication process, which modifies the antenna shape in an uncontrolled manner by introducing solder blobs with a typical size of a few tenths of a millimeter on the dipole arms (see Figure 5.18). Additionally, the SYNCA will be separately calibrated to account for azimuthal differences in the electric field magnitude. Therefore we see from the simulated performance of the PCB crossed-dipole antenna that this antenna design meets all three of the SYNCA criteria.

### 5.3.4 Characterization of the SYNCA

Two SYNCAs were manufactured using the PCB crossed-dipole design (see Figure 5.18). The antenna PCB (Matrix Circuit Board Materials, MEGTRON 6) is connected to four 2.92 mm coaxial connectors (Fairview Microwave, SC5843) using semi-rigid coax (Fairview Microwave, FMBC002), which also physically support the antenna PCB. The antenna PCB consists only of two layers which correspond to the copper antenna trace

and the PCB dielectric. Each coax line is connected to the associated dipole arm using through-hole soldering and phase matched to ensure that the electrical length of each of the transmission lines is identical at the operating frequency. The antenna PCB is further reinforced using custom cut polystyrene foam blocks, which have an electrical permittivity nearly identical to air. A custom 3D printed mount is included at the base of the antenna to support the coax connectors and to provide a sturdy mounting base.

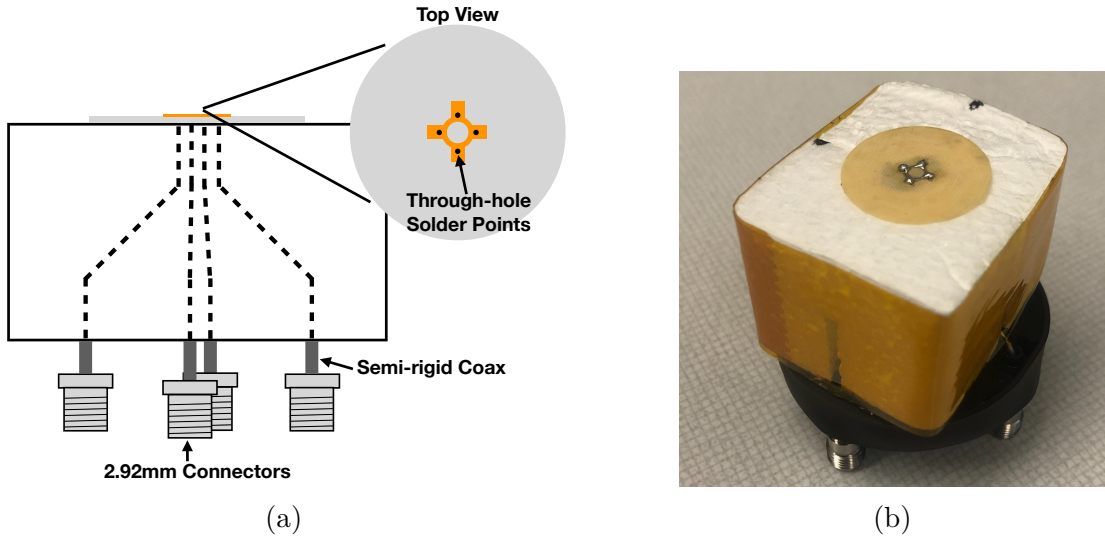


Figure 5.18: (a) A cartoon schematic which highlights the routing of the semi-rigid coax transmission lines. (b) A photograph of a SYNCA constructed using the modified crossed-dipole PCB antenna design. Visible in the photograph of the SYNCA are four blobs of solder which are an artifact of the SYNCA’s hand-soldered construction. These solder blobs are the most significant deviation from the SYNCA design shown in Figure 5.14 and are responsible for a significant fraction of the irregularities seen in the antenna pattern.

Characterization measurements were performed using a Vector Network Analyzer (VNA) to measure the electric field magnitude and phase radiated by the SYNCA to verify the radiation pattern (see Figure 5.19). The VNA is connected to the SYNCA at one port through a hybrid-coupler whose outputs are connected to two baluns to generate the signals with the appropriate phases to feed the SYNCA (see Figure 5.13). The other port of the VNA is connected to a single reference horn antenna that serves as a field probe. To position the SYNCA, a combination of translation and rotation stages are used to characterize the antenna’s fields across the entire radiation pattern circumference. This measurement scheme is equivalent to measuring the fields generated by the SYNCA using a full circular array of probe antennas.



Figure 5.19: A schematic of the VNA characterization measurements (a). This setup allows for antenna gain and phase measurements across a full  $360^\circ$  of azimuthal angles using a motorized rotation stage and control of the radial position of the SYNCA using a translation stage. A photo of the setup in the lab is shown in (b).

The antenna measurement space is surrounded by RF anti-reflective foam to isolate the measurements from the lab environment (see Figure 5.19b) and remaining reflections are removed using the VNA’s time-gating feature. The SYNCA is affixed to the stages by a custom RF transparent mount made of polystyrene foam. The coaxial cables deliver the antenna feed signals generated by the VNA to the SYNCA while still allowing unrestricted rotation. The horn antenna probe is nominally positioned in the plane formed by the antenna PCB ( $\theta = 90^\circ$  or  $z = 0$  mm) at a distance of 10 cm from the SYNCA, to match the expected position of the antenna array relative to the SYNCA in the antenna array test stand. The horn antenna can be manually raised or lowered to different relative vertical positions to characterize the radiation pattern at different polar angles.

Several  $360^\circ$  scans were performed with probe vertical offsets of -10.0 mm, -5.0 mm, 0.0 mm, 5.0 mm, and 10.0 mm relative to the antenna PCB plane. These probe offsets cover a 2 cm wide vertical region centered on the SYNCA PCB, approximately equal to  $\pm 6$  degrees of polar angle. The measurements show that the SYNCA is generating fields with nearly isotropic magnitude across the probed region. The standard deviation of the electric field magnitude measured around the antenna circumference is approximately 2.9 dB for a typical rotational scan. The presence of a significant pattern null is noted near  $45^\circ$  (see Figure 5.20), which we attribute to small imperfections in the antenna PCB that could be introduced from the hand soldered terminations connecting the coax

cables to the antenna. There is no significant difference in the radiation pattern when measured across the 2 cm vertical range. The measured relative phases closely follow the expectation for an electron, being linear with the measurement rotation angle and forming the expected spiral pattern. Other than the small phase imperfections there is a slight sinusoidal bias to the phase data, which we determined is the result of a small ( $\lesssim 1$  mm) offset of the antenna's phase center from the rotation axis of the automated stages.

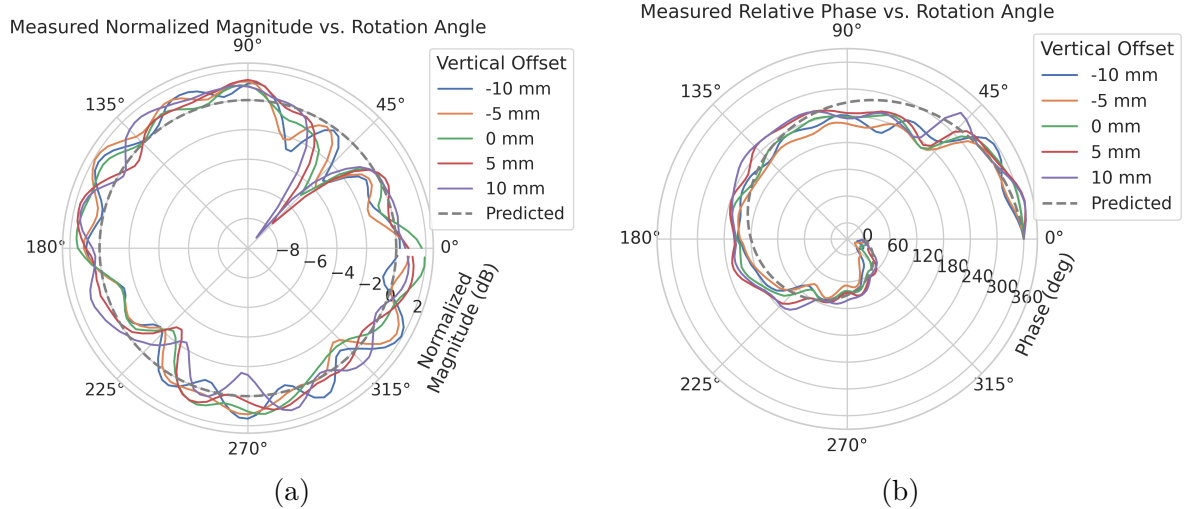


Figure 5.20: Linear interpolations of the measured electric field magnitude (a) and phase (b). The data was acquired using a VNA at 120 points spaced by 3 degrees from 0 to 357 degrees of azimuthal angle. The different color lines indicate the vertical offset of the horn antenna relative to the SYNCA PCB and the dashed line shows the expected shape from electron simulations. No significant difference in the antenna pattern is observed for the measured vertical offsets.

The characterization measurements confirm the simulated performance of the SYNCA. As expected the fields generated by the antenna are nearly isotropic in magnitude,  $\phi$ -polarized, and are linearly out of phase around the circumference of the antenna as predicted for cyclotron radiation in Section 5.3.2. Small imperfections in the magnitude and phase of the antenna are expected, particularly at the antenna's high operating frequency of 26 GHz where small geometric changes can have significant impacts on electrical properties. However, calibration through careful characterization measurements can be used to remove the majority of these pattern imperfections, including the relatively large pattern null near 45°, which will allow for the usage of the SYNCA as a test source for free-space CRES experiments utilizing antenna arrays. In the next section we use the

VNA measurements obtained here as a calibration for signal reconstruction using digital beamforming.

### 5.3.5 Beamforming Measurements with the SYNCA

Digital beamforming is a standard technique for signal reconstruction using a phased array [33]. The SYNCA, since it exhibits the same cyclotron phases as a trapped electron, can be used to perform simulated CRES digital beamforming reconstruction experiments on the bench-top without the need for the magnet, cryogenics, and vacuum systems required by a full CRES experiment. The fields received by the individual elements of the antenna array will have phases dependent on the spatial position of the source relative to the antennas. Therefore, a simple summation of the received signals will fail to reconstruct the signal due to destructive interference between the individual channels in the array. However, applying a phase shift associated with the source's spatial position removes phase differences and results in a constructive summation of the channel signals (see Figure 5.21). We can summarize the digital beamforming operation succinctly using the following equation

$$y[t_n] = \sum_{m=0}^{N-1} x_m[t_n] A_m e^{i\phi_m}, \quad (5.35)$$

where  $y[t_n]$  represents the summed array signal at time  $t_n$ ,  $x_m[t_n]$  is the signal received by channel  $m$  at time  $t_n$ ,  $\phi_m$  is the phase shift applied to the signal received at channel

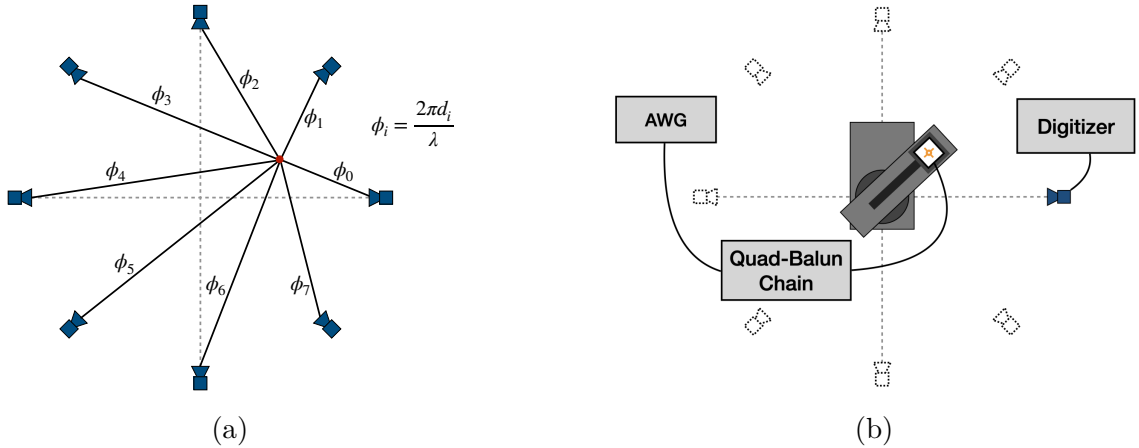


Figure 5.21: (a) A depiction of the relative phase differences for signals received by a circular antenna array from an isotropic source. The phases correspond to a unique spatial position. (b) A schematic of the setup used to perform digital beamforming.

$m$ , and  $A_m$  is an amplitude weighting factor that accounts for the different signal power received by individual channels. By changing the digital beamforming phases, the point of constructive interference can be scanned across the sensitive region of the array to search for the location of a radiating source, which is identified as the point of maximum summed signal power above a specified threshold. The digital beamforming phases consist of two components,

$$\phi_m = 2\pi d_m/\lambda + \theta_m, \quad (5.36)$$

where  $d_m$  is the distance from the  $m$ -th array element to the source, and  $\theta_m$  is the relative angle between the source position and the  $m$ -th antenna. The first component is the standard digital beamforming phase that corresponds to the spatial position of the source, and the second component is the cyclotron phase that corresponds to the relative azimuthal phase offset.

With a small modification to the hardware used to characterize the SYNCA (see Figure 5.19), we can perform a digital beamforming reconstruction of a synthetic CRES event. By replacing the VNA with an arbitrary waveform generator (AWG), the SYNCA can be used to generate cyclotron radiation with an arbitrary signal structure, which can then be detected by digitizing the signals received by the horn antenna. Rotational symmetry allows us to use the rotational stage of the positioning system to rotate the SYNCA to recreate the signals that would have been received by a complete circular array of antennas.

Using this setup, signals from a 60 channel circular array of equally spaced horn antennas were generated with the SYNCA positioned 10 mm off the central array axis, reconstructed using digital beamforming, and compared to Locust simulation (see Figure 5.22). When the cyclotron spiral phases are not used, which is equivalent to setting  $\theta_m$  in Equation 5.36 to zero, the SYNCA's position is reconstructed as a relatively faint ring as predicted by simulation. However, when the appropriate cyclotron phases are used during the beamforming procedure, both the simulated electron and the SYNCA appear as a single peak of high relative power corresponding to the source position. Therefore, we observe good agreement between the simulated and SYNCA reconstructions. While it may seem that for the case with no cyclotron phase corrections the ring reconstructs the position of the electron as effectively as beamforming with the cyclotron phase corrections, it is important to note that the simulations and measurements were generated without a realistic level of thermal noise. The larger maxima region and lower signal power, which occurs without the cyclotron phase corrections, significantly reduce the probability of detecting an electron in a realistic noise background.

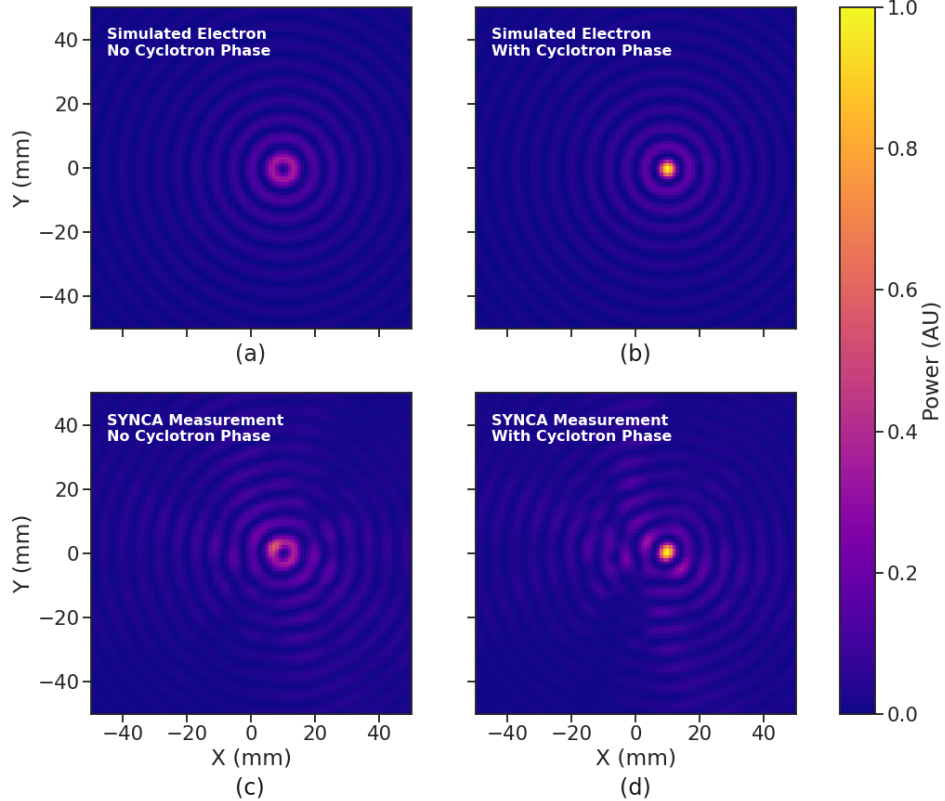


Figure 5.22: Digital beamforming maps generated using a simulated 60 channel array and electron simulated using the Locust package. (a) and (b) show the beamforming maps for simulated electrons without the cyclotron spiral phases and with the cyclotron spiral phases respectively. (c) and (d) show the beamforming maps produced from SYNCA measurements. We observe good agreement between simulated electrons and the SYNCA measurements.

To bound the beamforming capabilities of the synthetic array of horn antennas, we performed a series of beamforming reconstructions where the SYNCA was progressively moved off the central axis of the array (see Figure 5.23). To extract an estimate of the position of the SYNCA using the digital beamforming image we apply a 2-dimensional (2D) Gaussian fit to the image data and extract the estimated centroid value. We find that the synthetic horn antenna array reconstructs the position of the SYNCA with a  $1\sigma$ -error of 0.3 mm with no apparent trend across the 30 mm measurement range. This reconstruction error is an order of magnitude larger than mean fit position uncertainty of 0.02 mm indicating that systematic effects related to the SYNCA positioning system could be contributing additional uncertainty to the measurements. Note that the current mean reconstruction error of 0.3 mm is a factor of 20 smaller than the full width at half

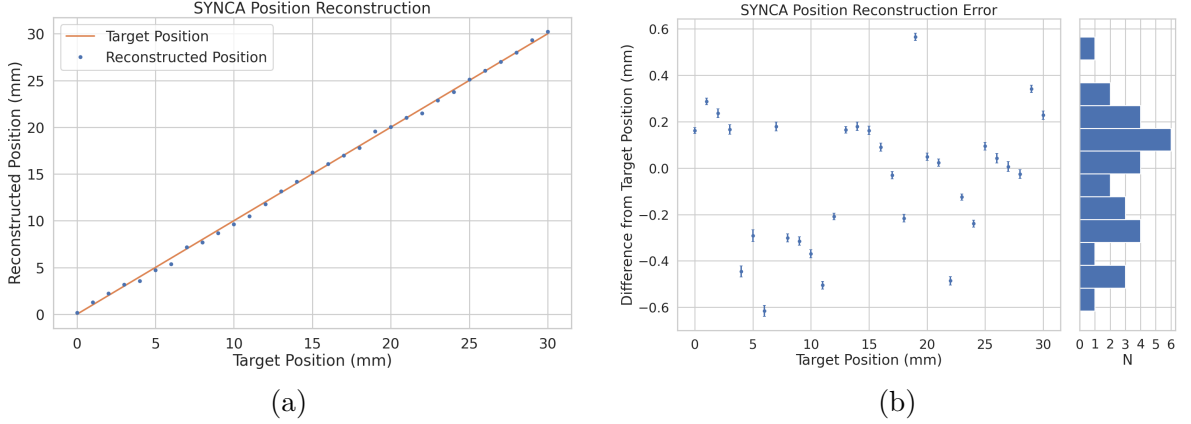


Figure 5.23: A plot of the SYNCA’s reconstructed position using the synthesized horn-antenna array and digital beamforming. (a) Shows the reconstructed position of the SYNCA compared with the target position indicated by the positioning system readout. (b) Shows the reconstruction error, which is the difference between the target and reconstructed positions. The error bars in (b) are the uncertainty in the mean position of the 2D Gaussian used to fit the digital beamforming reconstruction peak obtained from the fit covariance matrix. The mean fit position uncertainty of 0.02 mm is an order of magnitude smaller than the typical reconstruction error of 0.3 mm obtained by calculating the standard deviation of the difference between the reconstructed and target position.

maximum of the digital beamforming peak (6 mm), which could be interpreted as a naive estimate of the position reconstruction performance of this technique. Because these measurements are intended as a proof-of-principle demonstration, we do not investigate potential sources of systematic errors further; however, we expect that a similar and more thorough investigation will be performed using the Project 8 antenna array test stand, where typical reconstruction errors can be used to estimate the energy resolution limits of antenna array designs.

### **5.3.6 Conclusions**

In this paper we have introduced the SYNCA, which is a novel antenna design that emits radiation that mimics the unique properties of the cyclotron radiation generated by charged particles moving in a magnetic field. The characterization measurements of the SYNCA validated the simulated performance of the PCB crossed-dipole antenna design. Additionally, the SYNCA was used to estimate the position reconstruction capabilities of a synthesized array of horn antennas and experimentally reproduced the simulated digital beamforming reconstruction of electrons.

While the SYNCA performs well, there exist discrepancies in the phase and magnitude of the radiation pattern compared to the simulated SYNCA design that are related to the small geometric differences in the soldered connections. Future design iterations that replace the soldered connections with a fully surface mount design could improve the radiation pattern at the cost of some complexity and expense. Furthermore, improving the design of the antenna PCB and mounting system would allow the antenna to be inserted into a cryogenic and vacuum environment where in-situ antenna measurement calibrations could be performed.

The discrepancies in the radiation pattern and phases exhibited by the as-built SYNCA should not greatly impact its performance as a calibration probe. Both magnitude and phase variations can be accounted by applying the SYNCA characterization measurements as a calibration to the data collected by the antenna array test stand. The separate calibration of the SYNCA radiation does not impact the primary goals for the antenna array test stand which are array calibration and signal reconstruction algorithm performance characterization, because it can be performed with standard reference horn antennas with well understood characteristics.

The SYNCA antenna technology advances the CRES technique by providing a mechanism to characterize free-space antenna arrays for CRES measurements without the need for a magnet and cryogenics system, which would be required for calibration using electron sources. Both the Project 8 collaboration as well as future collaborations which are developing antenna array based CRES experiments can make use of SYNCA antennas as an important component of their calibration and commissioning phases.

## 5.4 FSCD Antenna Array Measurements with the SYNCA

### 5.4.1 Introduction

Using the SYNCA we can perform full-array measurements of prototype versions of the FSCD antenna array to test its performance with a realistic cyclotron radiation source (see Figure 5.24). The goal is to check how the measured power received by the array compares to FSCD simulations as a function of the radial and axial position of the SYNCA. These measurements are intended to validate the antenna research and development by Project 8, which has been driven primarily by simulations with Locust and CRESana, and identify any serious discrepancies in these simulations tools. This knowledge will provide confidence in the simulations necessary for the analysis of the

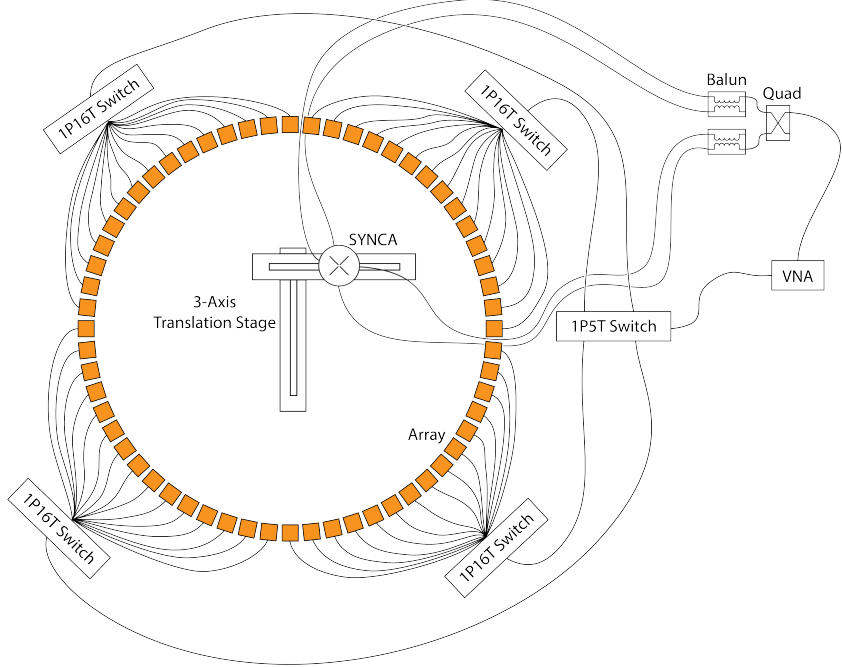


Figure 5.24: A diagram of the array measurement system used to test the prototype FSCD antenna array. A VNA is used as the primary measurement tool, which is connected to the array through a series of switches. The other port of the VNA connects to the SYNCA through the quad-balun chain used to provide the SYNCA feed signals. During measurements the SYNCA is positioned inside the center of the antenna array and translated to different radial and axial positions using a 3-axis manual translation stage setup.

sensitivity of larger antenna array based CRES experiment designs to the neutrino mass.

As we saw in Section 5.3, the SYNCA does have some radiation pattern imperfections that could complicate the comparison between measurement data and simulation data making it impossible to distinguish between errors from the SYNCA and errors from the antenna array. One way to disentangle some of these effects is to perform an additional set of measurements using a synthetic antenna array setup along with the SYNCA antenna. Since the synthetic array setup uses only a single array antenna, the data should be free of errors associated with antenna differences in the array and multipath interference between array channels, which are two error sources that may not be modeled correctly in simulations. Comparing the synthetic array data to the FSCD array data as well as the simulation data will allow us to evaluate the significance of these effects compared to errors introduced by SYNCA imperfections. Below we provide an overview of the full array and synthetic array measurement setups used to collect the data.

## 5.4.2 Measurement Setups

### 5.4.2.1 FSCD Array Setup

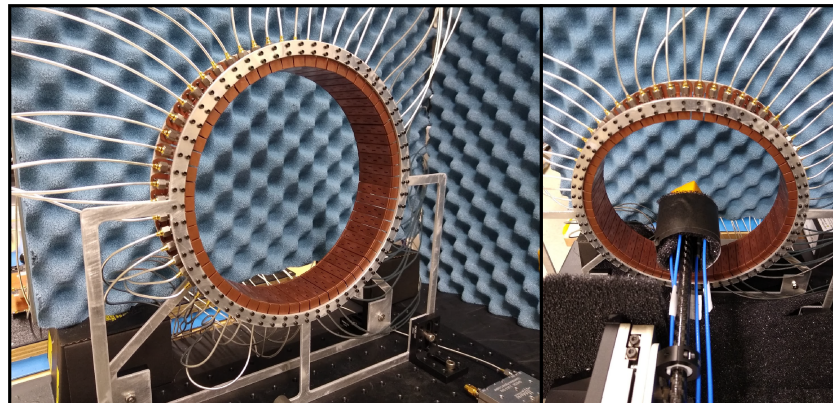
The antenna design used to construct the array is a 5-slot waveguide antenna developed for the FSCD experiment (see Figure 5.25a). The antenna is 5 cm long and is constructed out of WR-34 waveguide with a 2.92 mm coax connector located at the center of the antenna. Copper flanges located on both ends of the antenna are used to mount the antenna in the array support structure. The antenna array is supported by two circular steel brackets that can be bolted to both ends of the waveguide antennas to construct the circular antenna array (see Figure 5.25b). The antenna array is constructed using sixty identical waveguide antennas arranged in a circular pattern with a radius of 10 cm. Using the steel brackets the circular antenna array is mounted perpendicular to an optical breadboard surface, which provides sufficient space for the coaxial cable connections for each antenna and allows for easy positioning of the SYNCA antenna. The SYNCA antenna is mounted on the end of a carbon fiber rod that is attached to a set of manual translation stages, which are used to move the SYNCA antenna to different positions inside the array (see Figure 5.25c). The stages allow for independent motion in three different axes and can position the SYNCA at radial distances up to 5 cm from the center.

Data acquisition is accomplished using a two-port VNA in combination with a series of microwave switches that allow the VNA to connect to each channel in the array . The first port of the VNA is connected to the quad-balun chain used to feed the SYNCA (see Section 5.3), and the second port of the VNA connects to a 1P5T microwave switch. The 1P5T switch is connected to four separate 1P16T switch boards that connect directly to the array. The data acquisition is controlled by a python script running on a lab computer which, is connected to the VNA and an Arduino board programmed to control the microwave switches. The script uses the switches to iteratively connect each of the antennas in the array to the VNA, which loads the calibration file for the appropriate channel and performs the measurements for all S-parameters.

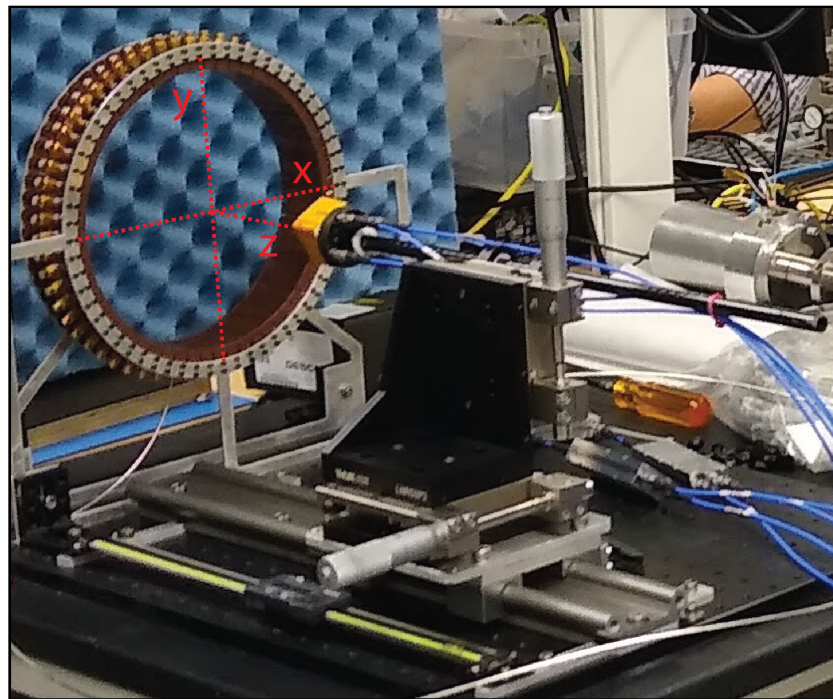
Array measurements were performed for the set of SYNCA positions consisting of radial (x-axis) positions from 0 to 50 mm in 5 mm steps and axial (z-axis) positions from 0 to 50 mm in 5 mm steps resulting in 121 array measurements. At each SYNCA position we measured the two-port S-parameter matrix using a linear frequency sweep from 25.1 to 26.1 GHz with 101 discrete frequencies. For each antenna in the array the VNA uses a separate calibration file so that errors arising from path differences in the



(a)



(b)



(c)

Figure 5.25: Photos of the prototype FSCD antenna (a), the FSCD array and SYNCA (b), and the translation stages and coordinate system used to position the SYNCA (c).

RF switches are effectively removed.

#### 5.4.2.2 Synthetic Array Setup

The setup used to perform the synthetic array measurements is shown in Figure 5.7b. The notable difference between this setup and the FSCD array setup is that the synthetic array measurements were performed with a waveform generator and digitizer instead of a VNA. However, we are still be able to compare the measured phases of the synthetic array and the relative magnitude of the power, since the digitized signal power is directly proportional to S21.

The arbitrary waveform generator is configured to produce a 64 MHz sine wave signal that is upconverted to 25.864 GHz using the a mixer and the VNA source configured to output a 25.8 GHz continuous wave. This signal is passed through a filter and fed to the SYNCA quad-balun chain. A single FSCD antenna is positioned 10 cm from the SYNCA and aligned vertically so that the center of the 5-slot waveguide is in the plane of the SYNCA PCB (see Figure 5.26). This position corresponds to  $z = 0$  in Figure 5.25c. The SYNCA is rotated in three degree steps to synthesize an antenna array with

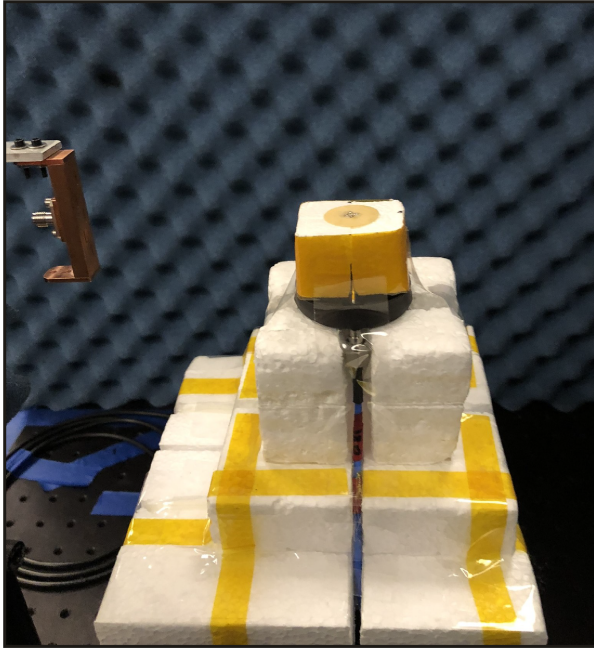


Figure 5.26: A photo of the FSCD antenna and the SYNCA in the synthetic array measurement setup at Penn State.

120 channels, which is more than could physically fit in a 10 cm radius array, to check of the smoothness of the antenna array radiation pattern. The signals from the FSCD

antenna are downconverted using another mixer connected to the VNA source before being digitized at 250 MHz and saved to disk. Several synthetic array measurement scans were performed by using the linear translation stage to change the radial position of the SYNCA. In total eight scans were taken from 0 to 35 mm using a radial position step size of 5 mm.

### 5.4.3 Simulations, Analysis, and Results

The Locust and CRESana simulation packages utilize the antenna transfer functions to calculate the amount of power that would be received by each antenna in the array from the electric fields produced by a trapped electron. For our VNA array setup the quantity that is directly proportional to this is the S21 matrix element, which indicates the ratio of the power received by an antenna in the array to the amount of power delivered to the SYNCA. Therefore, our analysis will focus on comparing the relative magnitude and phase of the the S21 parameters measured by the VNA as a function of the array channel and the SYNCA position. Additionally, we apply a beamforming reconstruction to the S21 data to evaluate how the summed power and beamforming images change as a function of the position of the SYNCA.

#### 5.4.3.1 Simulations

Simulations for the FSCD array measurements were performed using CRESana, which performs analytical calculations of the EM-fields produced by an electron at the position of the antennas. At each sampled time CRESana computes the electric field vector at the antenna positions, which is projected onto the antenna polarization axis to obtain the copolar electric field. The magnitude of the copolar electric field is then multiplied by a flat antenna transfer function to calculate the voltage signal produced by the antenna. CRESana simulations exploit the flat transfer functions of the FSCD antennas, which allows the electric field to be multiplied by the antenna transfer function rather than performing the full FIR calculation. These calculations produce a voltage time-series for each of the antennas in the array which can be analyzed in terms of the power in each antenna channel and the relative phase between channels to compare to the laboratory measurements.

CRESana was configured to simulate a 90° electron in a constant background magnetic field of  $\approx 0.958$  T with a kinetic energy of 18.6 keV. These parameters were chosen in order to mimic a possible CRES event near the tritium beta-decay spectrum endpoint

in the FSCD experiment. The constant background magnetic field guarantees that the guiding center of the electron is stationary across the duration of the simulation which is consistent with the SYNCA in the laboratory measurements. Simulations were performed with the electron's guiding center at radial positions from 0 to 45 mm in steps of 1 mm and axial positions from 0 to 30 mm in steps of 1 mm. The simulations generated time series consisting of 8192 samples at 200 MHz for the sixty channel FSCD antenna array geometry.

#### 5.4.3.2 Phase Analysis

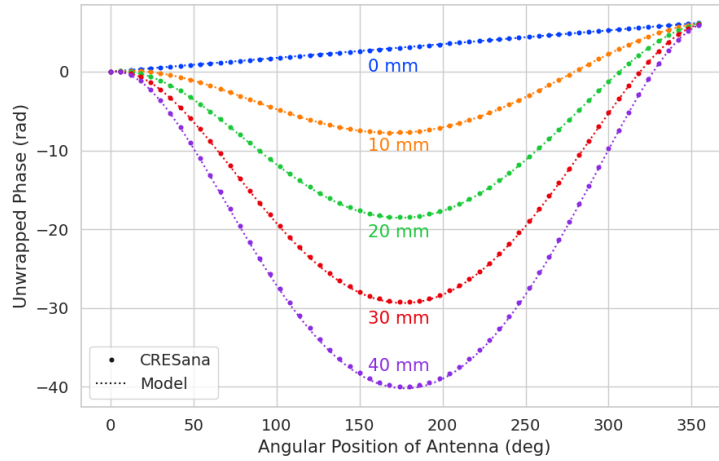


Figure 5.27: The unwrapped phases of signals received by the FSCD antenna array from an electron with a  $90^\circ$  pitch angle located in the plane of the antenna array. The data points indicated the phases extracted from simulation and the dashed lines show the model predictions.

The first part of our analysis examines the phases of the signals received by each channel in the antenna array since these features are fundamental to performing a beamforming reconstruction of the array signals as well as constructing accurate matched filter templates. Using simulations we have developed a beamforming phase model that allows us to predict the correct beamforming phases for a specific magnetic trap and assumed electron position. The equation for the model is

$$\phi_{ij}(t) = \frac{2\pi d_{ij}(t)}{\lambda} + \theta_{ij}(t), \quad (5.37)$$

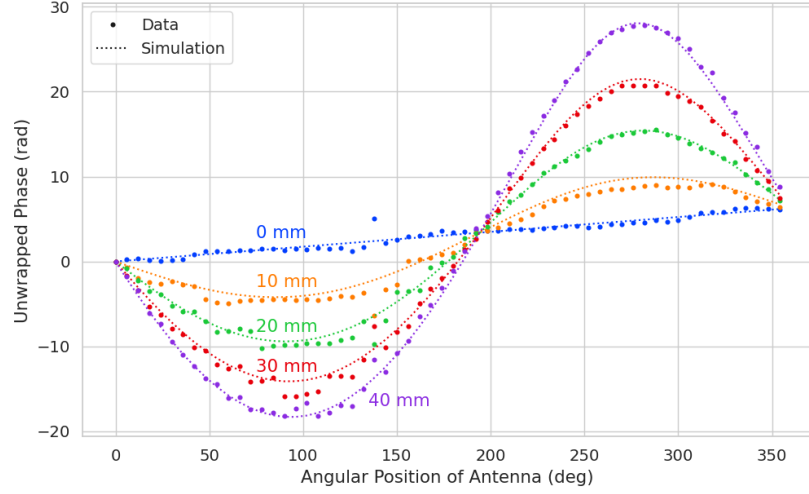
where  $d_{ij}(t)$  is distance between the assumed electron position and the antenna position,

and  $\theta_{ij}(t)$  is the angular separation between the electron and antenna positions. For more details on the components of the phase model see Section 5.3.2. In Figure 5.27 we compare the phases predicted by Equation 5.37 to phases extracted from CREsana simulations of an electron located in the plane of the antenna array at a series of radial positions and observe excellent agreement between the model and simulation.

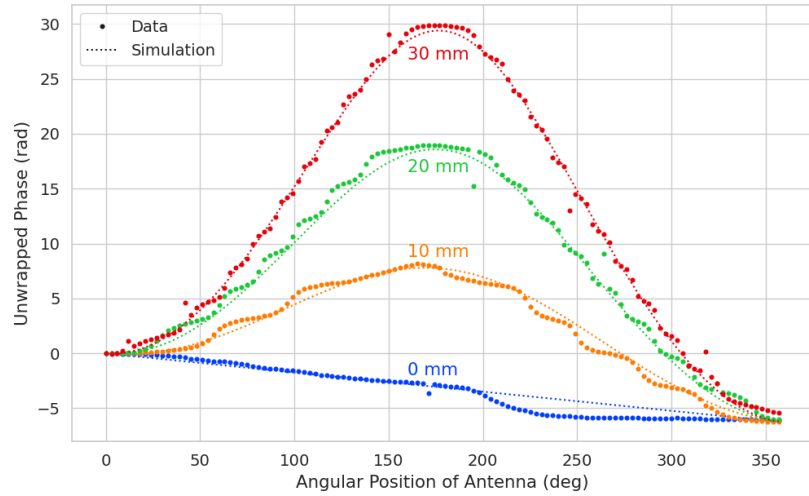
In Figures 5.28a and 5.28b we compare the phases measured in the FSCD array setup and the synthetic array setup to the phase model for a set of SYNCA radial positions. The axial position of the SYNCA in both plots is  $z = 0$  mm, such that the plane of the PCB is aligned with the center of the FSCD antenna. The data shown in Figure 5.28a corresponds to the S-parameters measured at 25.80 GHz which is the frequency closest to the one used in the synthetic array setup. The different slope and sinusoidal phases exhibited by Figure 5.28a and 5.28b reflects differences in the coordinate system for each setup. In general, we see that the phase model predicts the large scale features of the phases quite well, but there are some small scale deviations or errors from the phase model that do not appear to be present in simulation.

We are interested in examining the differences between the data and model more closely, so in Figure 5.29 we plot comparisons between the phase errors of the synthetic array data and the FSCD array data (labeled JUGAAD in the legend) as a function of the radial position of the SYNCA. Focusing on the trend for the synthetic array phase error data in Figure 5.29 we see that at  $R = 0$  mm the phase error forms a relatively smooth curve with the exception of an outlier data point caused by an unintended error in the data acquisition script. Since the position of the SYNCA antenna is stationary at  $R = 0$  mm, we attribute the observed phase errors to imperfections in the antenna pattern of the SYNCA that cause it to emit a radiation pattern whose phases do not perfectly match the beamforming phase model in Equation 5.37. As the SYNCA is moved away from  $R = 0$  mm in the synthetic array data we see that the phase error exhibits oscillations whose frequency increases as a function of the radial position of the SYNCA. These oscillations have the appearance of a diffraction pattern, which is particularly obvious for radii  $\geq 15$  mm, due to the bilateral symmetry of the phase error peaks around  $180^\circ$ .

Comparing the phase errors measured in the FSCD array to the synthetic array we see that there is a higher average variance in the phase error. This is best seen by comparing the curves at  $R \leq 15$  mm where the smooth synthetic array curves are distinct from the relatively noisy FSCD array errors. The extra noise in the FSCD array is most likely caused by differences in the radiation patterns of the antennas that make up the array



(a)



(b)

Figure 5.28: Plots of the measured unwrapped phases from the FSCD array (a) and the synthetic array (b) compared to the model predictions for a series of radial positions. The different phases of the sinusoidal phase oscillations in the two plots reflects differences in the coordinate systems of the measurements.

as well as differences in the transmission lines through the switch network that introduce additional phase errors into the measurement. Since the synthetic array measurements use only a single antenna, these extra error terms are not present, which explains the relatively smoother phase error curves. Despite the extra phase errors in the FSCD array, it is still possible to observe a similar phase error oscillation effect as the SYNCA is moved away from  $R = 0$  mm.

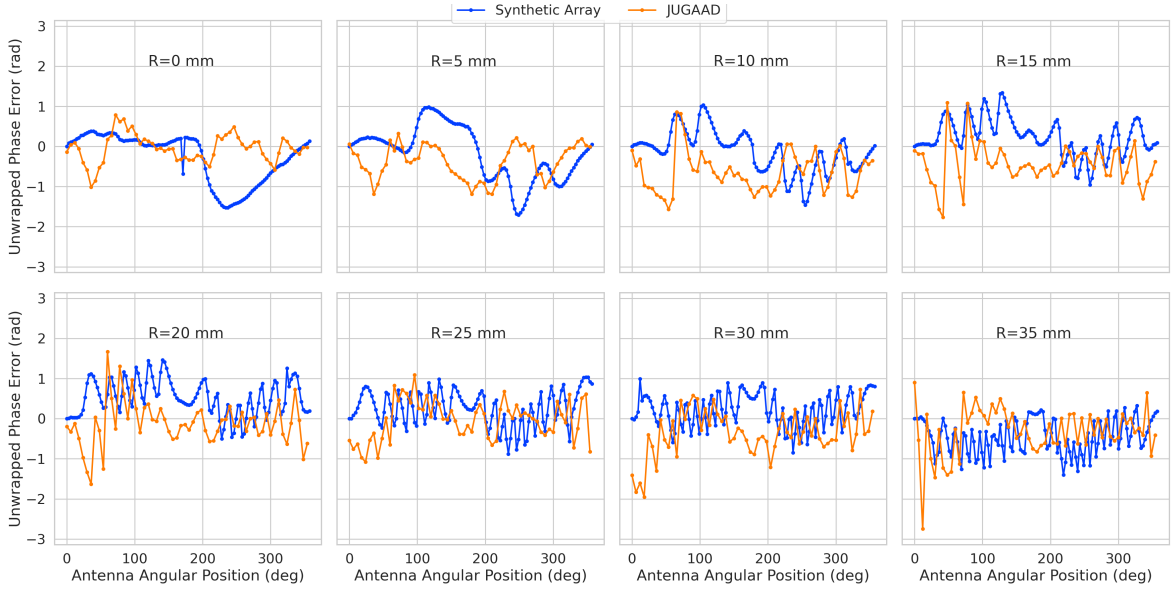
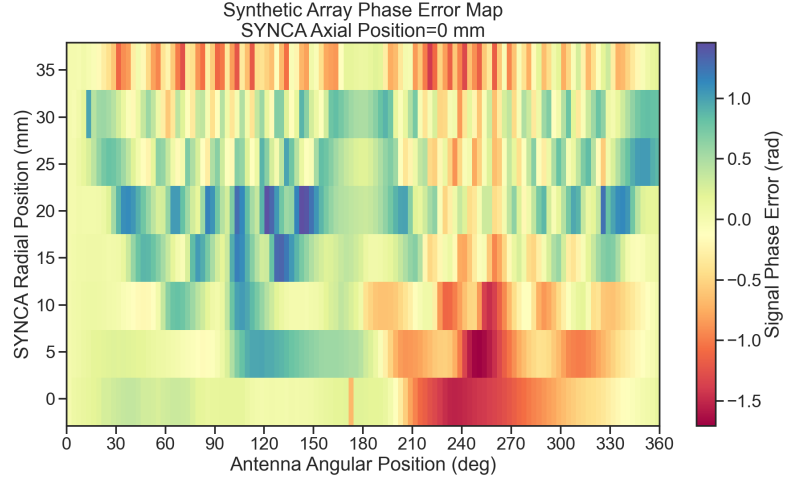


Figure 5.29: The phase errors between the measurement and model for the synthetic array (blue) and the FSCD array (orange) for a series of radial positions.

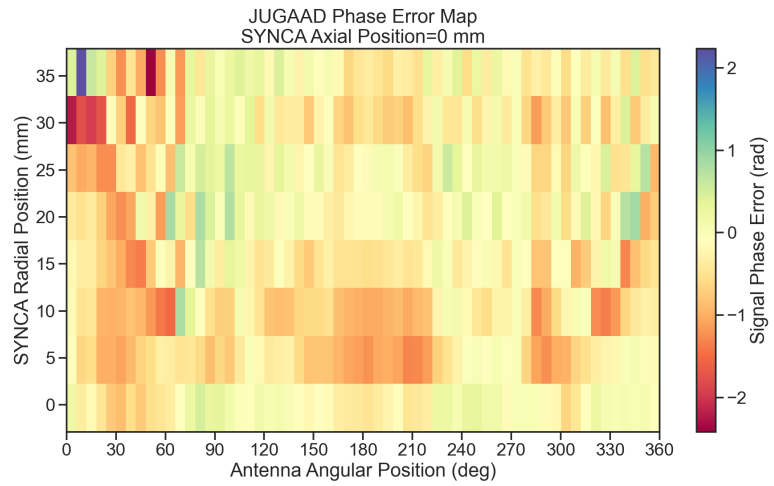
The diffraction pattern exhibited by the phase error oscillations is more easily observed by plotting the phase errors in a two-dimensional map, which we do in Figures 5.30a and 5.30b. For the synthetic array data we observe a relatively clear diffraction pattern that emerges as the SYNCA is moved radially. The bilateral symmetry of the diffraction patterns is due to the bilateral symmetry of the circular synthetic array around the translation axis of the SYNCA. A similar pattern is also visible in the FSCD array data although it is obscured by the additional phase error that results from the multi-channel array.

The physical origin of the phase error diffraction pattern is interference effects arising from path-length differences between the individual slots in the FSCD antenna and the SYNCA transmitter. Since we are operating in the radiative near-field of the FSCD antenna, the path length differences between the slots introduces a significant change in the summation of the signals that occurs inside the waveguide, which causes the radiation pattern of the antenna to change as a function of distance. Therefore, when the SYNCA is positioned off-axis the different path-lengths from the SYNCA to each antenna in the array results in different radiation patterns for each of the array antennas producing the observed diffraction pattern.

This near-field effect is not present in simulations, because in order to simplify the calculations we assume that the far-field approximation can be applied to the FSCD



(a)



(b)

Figure 5.30: Two dimensional plots of the phase errors for the synthetic array (a) and the FSCD (JUGAAD) array (b). In both plots we observe evidence of a similar diffraction pattern with bilateral symmetry, but the FSCD array measurements have an additional phase error contribution from the different antennas and paths through the switch network.

antennas. This means that the radiation pattern and antenna transfer functions are independent of the distance between the transmitter and the receiving antenna. In principle, we can account for these near-field effects with a more detailed simulation of the FSCD antennas either in CRESana or Locust, which would result in an additional term in the beamforming phase model. In the next section we briefly discuss the impact

of these near-field effects on the measured magnitude of the signals.

#### 5.4.3.3 Magnitude Analysis

In addition to phase, magnitude is the second component necessary to fully describe the radiation pattern and performance of the antenna array. However, it is not the dominant component from the perspective of beamforming and signal reconstruction. In many cases it is safe to approximate the relative amplitudes of the signals received by each channel as equal with minimal loss in detection efficiency. Therefore, our analysis of the magnitudes from CRESana, the FSCD array, and the synthetic array is less complete and serves mostly to reinforce the conclusions of the phase analysis.

We can use simulations to construct a model that describes the magnitude of the signals received by each channel in the antenna array. By examining the results of simulations or by analyzing the Liénard-Wiechert equation one can show that radiation pattern from a  $90^\circ$  pitch angle electron in a magnetic field is omni-directional. Therefore the relative magnitudes of the signals received by each channel will be determined by the free-space power loss, which is proportional to the inverse distance between the assumed electron position and the antenna. A consequence of this is that the signals produced in the array for electrons off the central axis will have larger amplitudes for the antennas closer to the electron compared to those which are further away. In Figure 5.31 we plot the amplitudes of the signals received by each antenna in the array from an electron located at a series of radial positions.

We expect to see a similar trend in the signal magnitudes in both the FSCD and synthetic arrays. In Figure 5.32 we plot the normalized signal magnitudes extracted from the VNA and digitizer measurements for a series of radial SYNCA positions. We use the data collected at the SYNCA axial position of  $z = 0$  mm for both the FSCD and synthetic arrays and show the S-parameters measured by the VNA at 25.86 GHz. A complication with these measurements is that the radiation pattern of the SYNCA is not perfectly omni-directional, which causes the measured magnitudes at  $R = 0$  mm to diverge from the perfectly flat behavior exhibited by electrons. As the SYNCA is moved away from  $R = 0$  mm in the synthetic array we observe a similar increase in the number of magnitude peaks that we would expect in a diffraction pattern, though this trend is less obvious than the phase data. Noticeably, there does not appear to be a set of channels with disproportionately larger amplitude at large  $R$ , which would be expected based on the trend from simulation.

Comparing the magnitudes of the synthetic array to the FSCD array in Figure 5.32

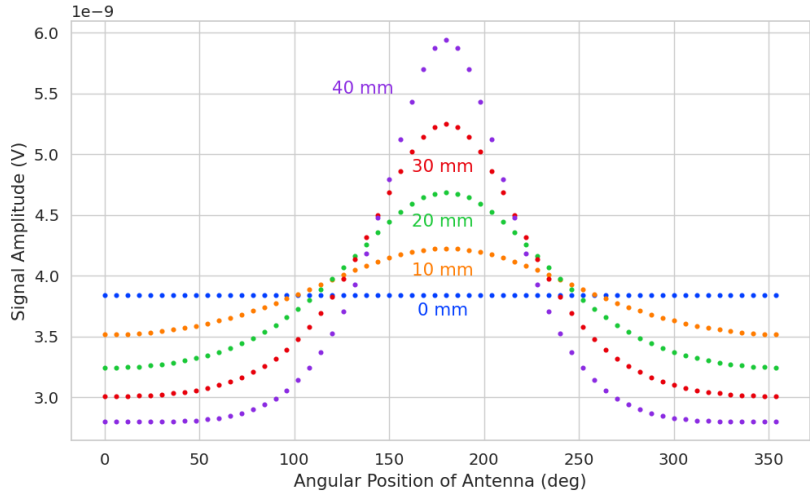


Figure 5.31: The amplitude of the signals from CREsana for the FSCD array from a  $90^\circ$  electron. As the electron is moved from  $R = 0$  the signals begin to have unequal amplitudes depending on the distance from the electron to the antenna.

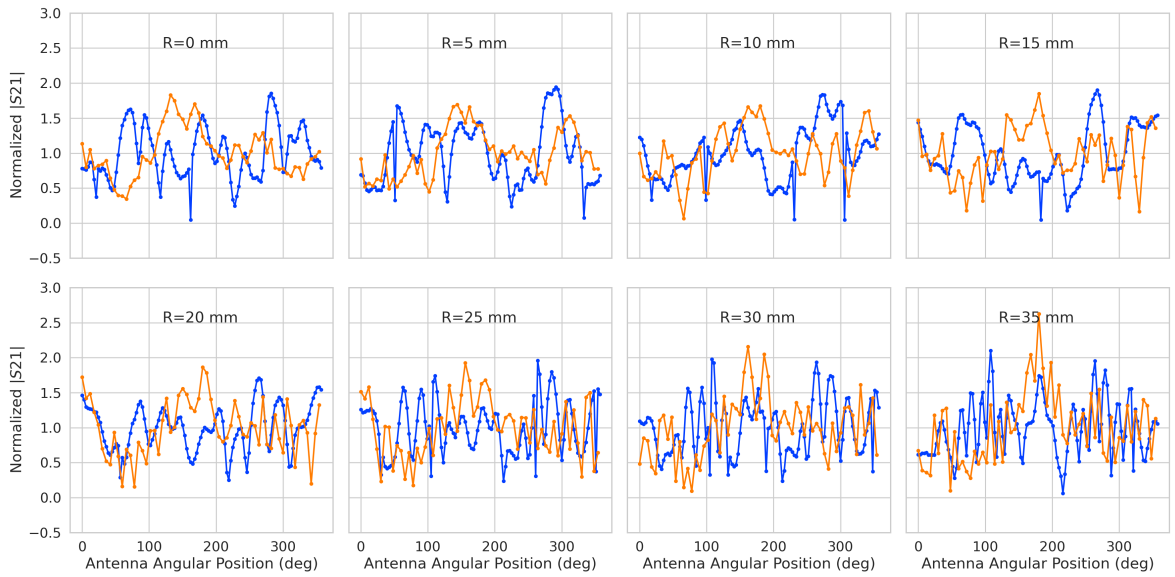
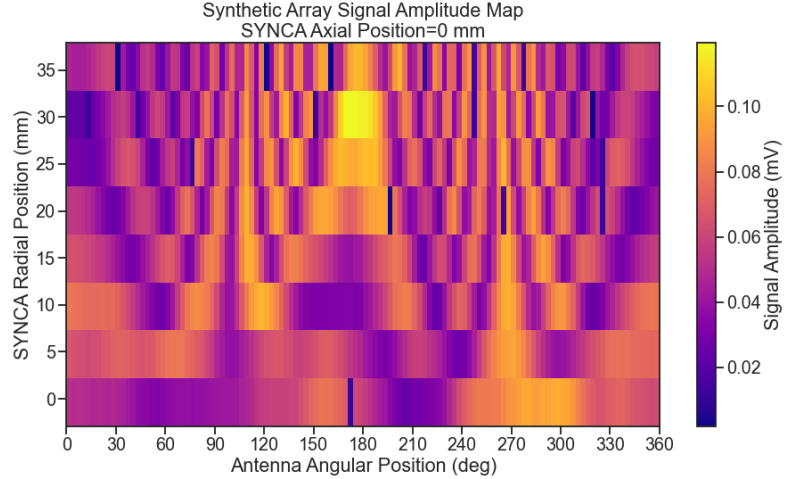
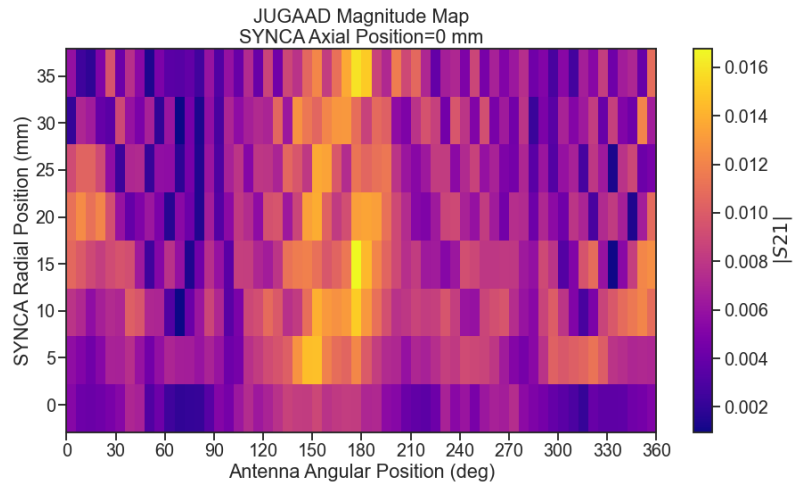


Figure 5.32: The normalized magnitudes of the S21 parameters measured in the FSCD (orange) and synthetic array (blue) setups. The dominant observed behavior as a function of radius is the increase in the number of magnitude peaks, which was noted in the phase error curves. There does not appear to be a strong change in the relative amplitude of a group of antennas as predicted by CREsana.



(a)



(b) The two-dimensional maps showing the diffractive pattern exhibited by the FSCD and synthetic array signal magnitudes.

Figure 5.33

we see that there is a similar amount of variability in the magnitudes at  $R = 0$  mm, although there is potentially more small scale error in the magnitude curve caused by channel differences in the FSCD array. We observe a similar trend in the number of magnitude error peaks in the FSCD array data to the synthetic array data, which mirrors the diffraction effect observed in the phase data. The diffraction effect can be visualized more clearly by plotting a similar two-dimensional map of the magnitudes (see Figure 5.33).

Observing a similar diffractive pattern in the signal magnitudes as a function the

SYNCA position reinforces our conclusions from the phase analysis that near-field effects are having a significant impact on the radiation pattern of the FSCD array. These near-field effects lead to changes in the magnitude and phase of the radiation pattern of the FSCD antenna as a function of distance. If left uncorrected these errors reduce detection efficiency by causing power loss in the beamforming or matched filter reconstruction due to phase mismatch. We explore the impact of these phase and magnitude errors on beamforming in the next section.

#### 5.4.3.4 Beamforming Characterization

The errors in the magnitude and phase of the FSCD array radiation pattern lead to errors in the signal reconstruction. For example, a matched filter reconstruction requires accurate knowledge of the relative phases and magnitudes of the signals in each channel to achieve optimal performance. Uncorrected errors here leads to mismatch between the template and signal, which reduces detection efficiency and introduces uncertainty in the parameter estimation. In this section, we analyze the beamformed signal amplitude as a function of the position of the SYNCA to quantify the impact of the phase and magnitude errors on signal reconstruction. Because of the imperfections in the SYNCA source, it is inappropriate to directly compare the beamformed signal amplitude of the FSCD array or synthetic array. Such a comparison would not allow us to disentangle losses that occur because of the antenna array from those that occur because of the source. Therefore, we focus on comparing the beamforming of the FSCD array to the synthetic array.

Our first method of comparison is to analyze the images generated by applying the beamforming reconstruction specified in Section 4.3.1 to the FSCD and synthetic array data (see Figure ??). We use a beamforming grid consisting of a square  $121 \times 121$  grid spanning a range of -60-mm to 60 mm in the x and y dimensions. The beamforming images formed from the synthetic array produces a three-dimensional matrix where each grid position contains a summed time series. We form a single beamforming image from this matrix by taking the average over the time dimension. Applying beamforming to the FSCD array data also produces a three-dimensional matrix, but in this case each grid position contains a summed frequency series produced by the VNA sweep. In order to generate a clearer beamforming image we average over the entire frequency sweep.

There is a clear difference between the synthetic and FSCD array beamforming images, which is the additional faint beamforming maxima located directly opposite the maxima corresponding to the SYNCA position. The images in Figure 5.34 were generated with

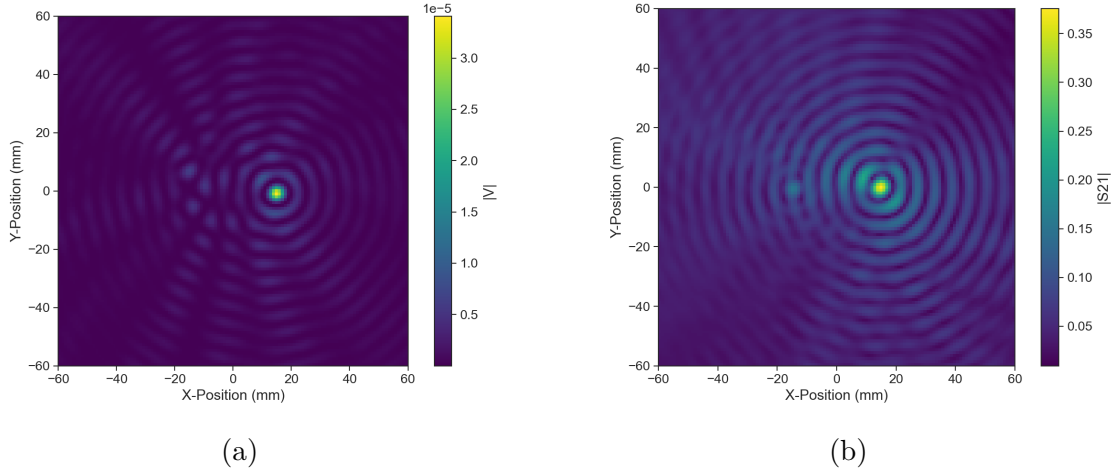


Figure 5.34: Beamforming images from the synthetic array (a) and FSCD array (b) setups with the SYNCA positioned 15 mm off the central axis. In both images we see a clear maxima that corresponds to the true SYNCA position. However, in the FSCD array there is an additional faint peak located at the opposite position of the beamforming maximum. This additional peak is the mirror of the true peak and is the result of reflections between antennas in the FSCD array.

data collected at a SYNCA radial position of 15 mm, which agrees well with the observed beamforming maximum in both images. We observe that the faint beamforming peak is located directly opposite of the true beamforming maximum similar to a mirror image. Therefore, the origin of this additional feature appears to be reflections between the two sides of the circular antenna array that are not present for the synthetic array since only a single physical antenna is used.

From the beamforming images we extract the maximum amplitude, which we plot as a function of the radial position of the SYNCA (see Figure 5.35). The phase errors we observed in the FSCD and synthetic arrays leads to power loss at the beamforming stage due to phase mismatches between the signals at different channels. This power loss can be quantified by comparing the signal amplitude obtained from beamforming to the amplitude which would be obtained from an ideal summation. We perform the ideal summation by phase shifting each array channel to the same phase and then summing. The comparison between the beamforming and ideal sums is shown in Figure 5.35, where we observe that both the synthetic and FSCD arrays experience power losses from the beamforming summation.

The beamforming power loss can be quantified using the ratio of the beamforming to ideal signal amplitudes. Computing this ratio as a function of SYNCA radial position radius for the FSCD and synthetic arrays we find that the FSCD array has a uniformly

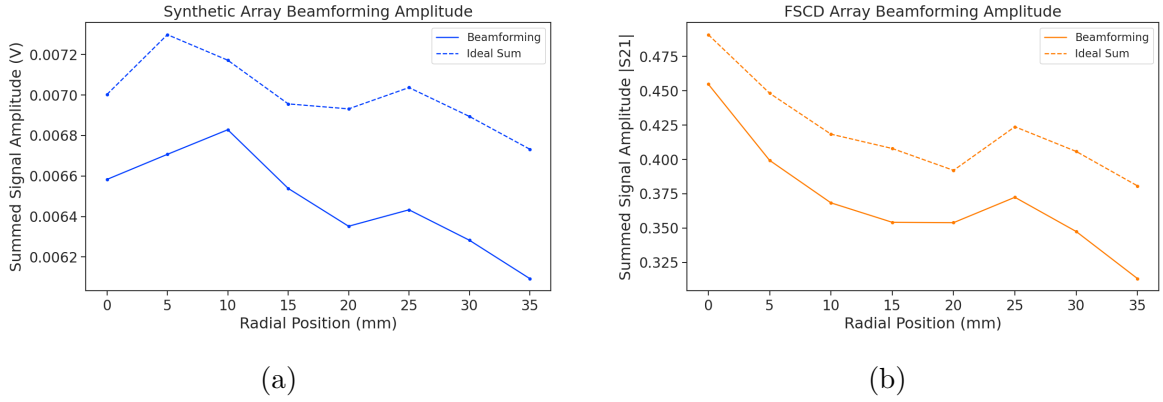


Figure 5.35: A comparison of the maximum signal amplitude obtained by beamforming to the signal amplitude obtained with an ideal summation as a function of the radial position of the SYNCA. The amplitudes for the synthetic array are shown in (a) and the FSCD array are shown in (b). In both setups we observe that the signal amplitudes obtained from beamforming are smaller than the signal amplitude that could be attained with the ideal summation without phase mismatch.

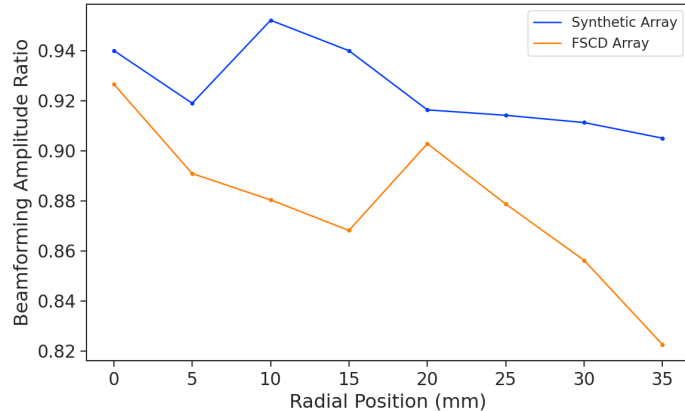


Figure 5.36: The ratio of the beamforming signal amplitude to the ideal signal amplitude for the FSCD and synthetic arrays. We see that the FSCD array has a larger power loss from phase error compare to the synthetic array which indicates that calibration errors associated with the multiple channels as well as reflections are impacting the signal reconstruction.

smaller beamforming amplitude ratio, which means that the FSCD array has a larger beamforming power loss (see Figure 5.36). The primary contributions to the beamforming power loss in the synthetic array are phase errors from the SYNCA and phase errors from the FSCD antenna near-field. Both of these phase errors contribute to beamforming losses in the FSCD array, but there are clearly additional phase errors in the FSCD array

measurements contributing to the smaller ratio. Two potential error sources include phase differences in the different antenna channels that could not be corrected by calibration as well as reflections between antennas in the array. The total effect of these additional phase errors is to reduce the beamforming amplitude ratio by about 5% from the beamforming ratio of the synthetic array. Therefore, we estimate that if no effort is made to correct these phase errors in an FSCD-like experiment, then we expect approximately a 10% total signal amplitude loss from a beamforming signal reconstruction.

#### 5.4.4 Conclusions

The estimated power loss of a beamforming reconstruction obtained from this analysis provides valuable inputs to sensitivity calculations of a FSCD-like antenna array experiment to measure the neutrino mass, since it helps to bound systematic uncertainties from the antenna array and reconstruction pipeline. This power loss lowers the estimated detection efficiency of the experiment since some of the signal power is lost due to improper combining between channels and also increases the uncertainty in the electron's kinetic energy by contributing to errors in the estimation of the electron's cyclotron frequency.

If these reconstruction losses prove unacceptable there are steps that can be taken to mitigate their effects. Some examples include the development of a more accurate antenna simulation approach that can reproduce the observed near-field interference patterns of the FSCD antennas and the implementation of a calibration approach that allows for the relative phase delays of the array to be measured without changing or disconnecting the antenna array configuration.

# **Chapter 6 |**

# **Development of Resonant Cavities for Large Volume CRES Measurements**

## **6.1 Introduction**

The cavity approach is an alternative CRES measurement technology under consideration by the Project 8 collaboration for a neutrino mass measurement experiment with 40 meV sensitivity. After pursuing an antenna array based CRES demonstrator design for several years the increasing costs and complexity of the antenna arrays led to a reexamination of resonant cavities for a large scale experiment. Currently, a cavity based CRES experiment is the preferred technology for the Project 8 neutrino mass measurement goal with antennas as a fall-back approach.

In this chapter we provide a brief summary of resonant cavities and sketch out the key features of a cavity based CRES experiment. In Section 6.2 we provide a brief introduction to cylindrical resonant cavities and the solutions for the electromagnetic fields in the cavity volume.

In Section 6.3 we describe the main components of a cavity based CRES experiment. Including the background and trap magnets, cavity geometry and design, and cavity coupling considerations. We also discuss some relevant trade-offs between an antenna array and cavity CRES experiment, and highlight some reasons for the transition of Project 8 to the development of a cavity based experiment.

Finally, in Sections 6.4 and 6.5 I present the design and development of an open, mode-filtered cavity that could be used in a cavity based CRES experiment. The results of the cavity simulations are confirmed by laboratory measurements of a proof-of-principle prototype cavity intended to demonstrate key features of the design.

## 6.2 Cylindrical Resonant Cavities

Resonant cavities are essentially sealed conductive containers, which allows us to describe the electromagnetic (EM) fields as a superposition of resonant modes. The field shapes of the resonant modes are determined by Maxwell's equations and the boundary conditions enforced by the cavity geometry. Of interest to Project 8 for CRES measurements are cylindrical cavities due to their ease of construction and integration with atom and electron trapping magnets.

### 6.2.1 General Field Solutions

Consider a long segment of conducting material with a cylindrical cross-section (see Figure 6.1). A geometry such as this can be used as a waveguide transmission line to transfer EM energy from point to point, or, if conducting shorts are inserted on both ends of the cylinder, the waveguide becomes a resonant cavity.

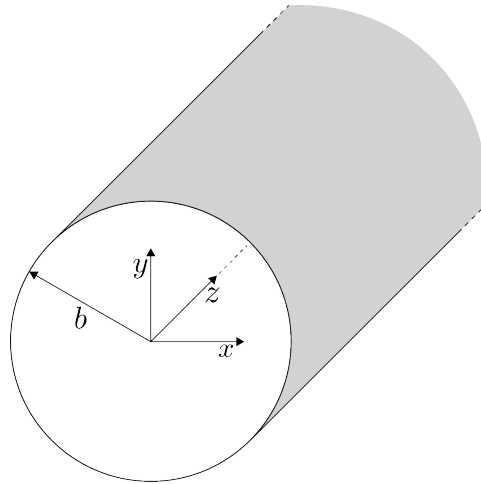


Figure 6.1: Geometry of a cylindrical waveguide with radius  $b$ .

The fields allowed inside a cylindrical cavity are determined by the boundary conditions of the cylindrical geometry. The general approach to solving for the fields begins by assuming solutions to Maxwell's equations of the form

$$\mathbf{E}(x, y, z) = (\mathbf{e}(x, y) + \hat{z}e_z(x, y))e^{-i\beta z}, \quad (6.1)$$

$$\mathbf{H}(x, y, z) = (\mathbf{h}(x, y) + \hat{z}h_z(x, y))e^{-i\beta z}. \quad (6.2)$$

The solutions assume a harmonic time dependence of the form  $e^{i\omega t}$  and propagation

along the positive z-axis. The functions  $\mathbf{e}(x, y)$  and  $\mathbf{h}(x, y)$  represent the transverse  $(\hat{x}, \hat{y})$  components of the electric and magnetic fields respectively, and  $e_z(x, y)$ ,  $h_z(x, y)$  are the longitudinal components. The version of Maxwell's equations in the case where there are no source terms can be written as a pair of coupled differential equations,

$$\nabla \times \mathbf{E} = -i\omega\mu\mathbf{H}, \quad (6.3)$$

$$\nabla \times \mathbf{H} = i\omega\epsilon\mathbf{E}, \quad (6.4)$$

where  $\epsilon$  and  $\mu$  are the permittivity and permeability of the material inside the waveguide or cavity. Using the field solutions from Equations 6.1 and 6.2 one can solve for the transverse components of the fields in terms of the longitudinal fields. Because we are interested in cylindrical cavities it is advantageous to write the field solutions in cylindrical coordinates. After performing this transformation the set of four equations for the transverse field components are,

$$H_\rho = \frac{i}{k_c^2} \left( \frac{\omega\epsilon}{\rho} \frac{\partial E_z}{\partial\phi} - \beta \frac{\partial H_z}{\partial\rho} \right), \quad (6.5)$$

$$H_\phi = \frac{-i}{k_c^2} \left( \omega\epsilon \frac{\partial E_z}{\partial\rho} + \frac{\beta}{\rho} \frac{\partial H_z}{\partial\phi} \right), \quad (6.6)$$

$$E_\rho = \frac{-i}{k_c^2} \left( \beta \frac{\partial E_z}{\partial\rho} + \frac{\omega\mu}{\rho} \frac{\partial H_z}{\partial\phi} \right), \quad (6.7)$$

$$E_\phi = \frac{i}{k_c^2} \left( -\beta \frac{\partial E_z}{\partial\phi} + \omega\mu \frac{\partial H_z}{\partial\rho} \right), \quad (6.8)$$

where  $k_c$  is the cutoff wavenumber defined by  $k_c^2 = k^2 - \beta^2$  with  $k = \omega\sqrt{\mu\epsilon}$  being the wavenumber of the EM radiation.

This set of equations can be used to solve for a variety of different modes that can be obtained by setting conditions on  $E_z$  and  $H_z$ . For cylindrical cavities two types of modes are allowed, which correspond to solutions where  $E_z = 0$  and  $H_z = 0$  respectively.

### 6.2.2 TE and TM Modes

The TE family of modes corresponds to the case where  $E_z = 0$ . This implies that  $H_z$  is a solution to the Helmholtz wave equation

$$(\nabla^2 + k^2)H_z = 0. \quad (6.9)$$

For solutions of the form  $H_z(\rho, \phi, z) = h_z(\rho, \phi)e^{-i\beta z}$ , Equation 6.9 can be solved using the standard technique of separation of variables. Rather than reproduce the derivation here we shall simply quote the solutions for the transverse fields, which are

$$H_\rho = \frac{-i\beta}{k_{c_{nm}}} (A \sin n\phi + B \cos n\phi) J'_n(k_{c_{nm}}\rho) e^{-i\beta_{nm}z}, \quad (6.10)$$

$$H_\phi = \frac{-i\beta n}{k_{c_{nm}}^2 \rho} (A \cos n\phi - B \sin n\phi) J_n(k_{c_{nm}}\rho) e^{-i\beta_{nm}z}, \quad (6.11)$$

$$E_\rho = \frac{-i\omega\mu n}{k_{c_{nm}}^2 \rho} (A \cos n\phi - B \sin n\phi) J_n(k_{c_{nm}}\rho) e^{-i\beta_{nm}z}, \quad (6.12)$$

$$E_\phi = \frac{i\omega\mu}{k_{c_{nm}}} (A \sin n\phi + B \cos n\phi) J'_n(k_{c_{nm}}\rho) e^{-i\beta_{nm}z}. \quad (6.13)$$

One can observe that the solutions have a periodic dependence on  $\phi$ , and radial profiles given by the Bessel functions of the first kind. The integer indices  $n$  and  $m$  arise from continuity conditions on the EM fields in the azimuthal and radial directions. For the TE modes  $n \geq 0$  and  $m \geq 1$ .  $k_{c_{nm}}$  is the cutoff wavenumber for the  $\text{TE}_{nm}$  mode given by

$$k_{c_{nm}} = \frac{p'_{nm}}{b}, \quad (6.14)$$

where  $b$  is the radius of the cavity or waveguide and  $p'_{nm}$  is the  $m$ -th root of the derivative of the  $n$ -th order Bessel function (see Table 6.1).

Table 6.1: A table of the values of  $p'_{nm}$ .

$n$	$p'_{n1}$	$p'_{n2}$	$p'_{n3}$
0	3.832	7.016	10.174
1	1.841	5.331	8.536
2	3.054	6.706	9.970

The TM mode family corresponds to the case where  $H_z = 0$ , and  $(\nabla^2 + k^2)E_z = 0$ . Again, we assume solutions of the form  $E_z(\rho, \phi, z) = e_z(\rho, \phi)e^{-i\beta z}$ , for which the general form of the solutions is the same as for the TE modes. However, the different boundary conditions for the TM modes results in particular solutions with a different form, which we shall quote here without derivation. The transverse fields of the TM modes are given by

$$H_\rho = \frac{-i\omega\epsilon n}{k_{c_{nm}}^2 \rho} (A \cos n\phi - B \sin n\phi) J_n(k_{c_{nm}}\rho) e^{-i\beta_{nm}z}, \quad (6.15)$$

$$H_\phi = \frac{-i\omega\epsilon}{k_{c_{nm}}}(A \sin n\phi + B \cos n\phi) J'_n(k_{c_{nm}}\rho) e^{-i\beta_{nm}z} \quad (6.16)$$

$$E_\rho = \frac{-i\beta}{k_{c_{nm}}}(A \sin n\phi + B \cos n\phi) J'_n(k_{c_{nm}}\rho) e^{-i\beta_{nm}z}, \quad (6.17)$$

$$E_\phi = \frac{-i\beta n}{k_{c_{nm}}^2 \rho}(A \cos n\phi - B \sin n\phi) J_n(k_{c_{nm}}\rho) e^{-i\beta_{nm}z}, \quad (6.18)$$

which one may notice are the same solutions as the TE modes with  $H$  and  $E$  flipped. The cutoff wavenumber for the TM modes is given by,  $k_{c_{nm}} = p_{nm}/b$ , where the values of  $p_{nm}$  correspond to the  $m$ -th zero of the  $n$ -th order Bessel function (see Table 6.2).

Table 6.2: A table of the values of  $p_{nm}$ .

$n$	$p_{n1}$	$p_{n2}$	$p_{n3}$
0	2.405	5.520	8.654
1	3.832	7.016	10.174
2	5.135	8.417	11.620

### 6.2.3 Resonant Frequencies of a Cylindrical Cavity

A cylindrical cavity is essentially constructed by taking a section of cylindrical waveguide and shorting both ends with conductive material. This means that the electric fields inside a cylindrical cavity are exactly those we derived in Section 6.2.2 with the additional condition that the electric fields must go to zero at  $z = 0$  and  $z = L$  (see Figure 6.2).

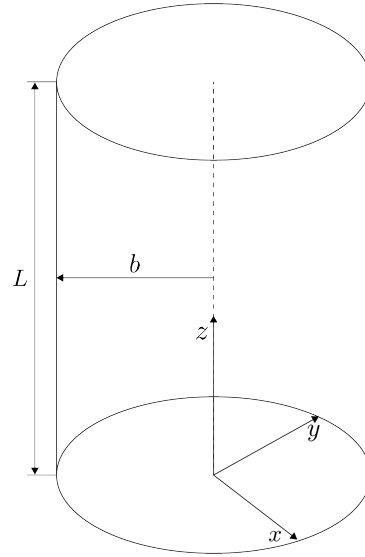


Figure 6.2: The geometry of a cylindrical cavity with length  $L$  and radius  $b$ .

The transverse electric field solutions for a cylindrical waveguide are of the form

$$\mathbf{E}(\rho, \phi, z) = \mathbf{e}(\rho, \phi) (A_+ e^{-i\beta_{nm}z} + A_- e^{i\beta_{nm}z}), \quad (6.19)$$

where  $A_+$  and  $A_-$  are arbitrary amplitudes of forward and backward propagating waves. In order to enforce that  $\mathbf{E}$  is zero at both ends of the cavity we require that

$$\beta_{nm}L = 2\pi\ell, \quad (6.20)$$

where  $\ell = 0, 1, 2, 3, \dots$ . Using this constraint on the propagation constant we can solve for the resonant frequencies of the  $\text{TE}_{nml}$  and the  $\text{TM}_{nml}$  modes in a cylindrical cavity. For the TE modes the resonant frequencies are

$$f_{nml} = \frac{c}{2\pi\sqrt{\mu_r\epsilon_r}} \sqrt{\left(\frac{p'_{nm}}{b}\right)^2 + \left(\frac{\ell\pi}{L}\right)^2}, \quad (6.21)$$

and the frequencies of the TM modes are

$$f_{nml} = \frac{c}{2\pi\sqrt{\mu_r\epsilon_r}} \sqrt{\left(\frac{p_{nm}}{b}\right)^2 + \left(\frac{\ell\pi}{L}\right)^2}. \quad (6.22)$$

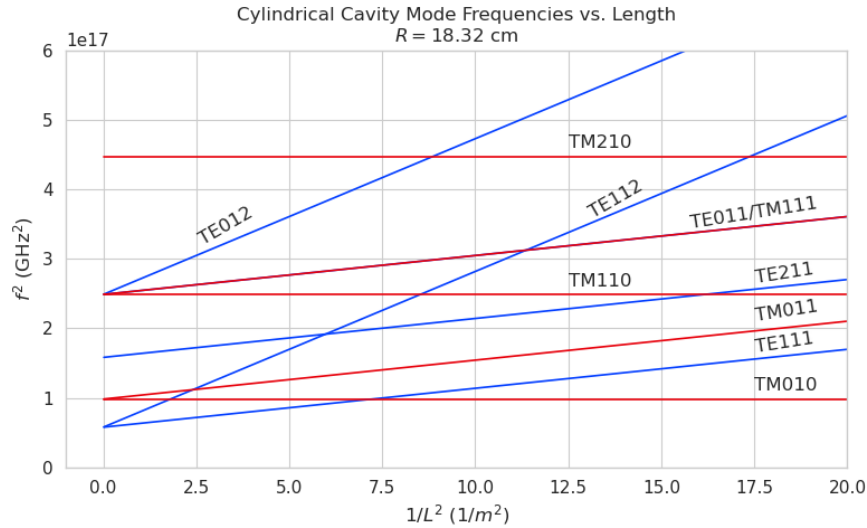


Figure 6.3: Relation of mode frequency to cavity length for a cylindrical cavity with a radius of 18.32 cm.

### 6.2.4 Cavity Q-factors

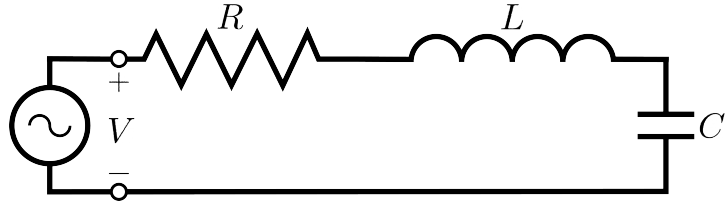


Figure 6.4: A series RLC circuit.

The resonant behavior of cylindrical cavities can be modeled as a series RLC circuit (see figure 6.4). The input impedance of the circuit can be obtained by applying Kirchhoff's laws to calculate the impedance of the equivalent circuit. For a series RLC circuit the input impedance is

$$Z_{\text{in}} = \left( \frac{1}{R} + \frac{1}{i\omega L} + i\omega C \right). \quad (6.23)$$

The resistance in the circuit represents all sources of loss in the cavity, which is primarily caused by the finite conductivity of the cavity walls, and the inductor and capacitor represent the energy stored in the cavity in the form of electric and magnetic fields. If the circuit is being driven by an external power source we can write the input power in terms of the circuit input impedance and the source voltage

$$P_{\text{in}} = \frac{1}{2} Z_{\text{in}} |I|^2 = \frac{1}{2} |I|^2 \left( \frac{1}{R} + \frac{1}{i\omega L} + i\omega C \right). \quad (6.24)$$

The resistor introduces a loss into the system with a power given by

$$P_{\text{loss}} = \frac{1}{2} |I|^2 R, \quad (6.25)$$

and the capacitor and inductor store energies given by

$$W_e = \frac{1}{4} \frac{|I|^2}{\omega^2 C}, \quad (6.26)$$

$$W_m = \frac{1}{4} |I|^2 L, \quad (6.27)$$

respectively. Using these expressions we can write the input power and input impedance

expressions in terms of the lost power and stored energy

$$P_{\text{in}} = P_{\text{loss}} + 2i\omega(W_m - W_e), \quad (6.28)$$

$$Z_{\text{in}} = \frac{P_{\text{loss}} + 2i\omega(W_m - W_e)}{\frac{1}{2}|I|^2}. \quad (6.29)$$

The condition for resonance in the RLC circuit is that the stored magnetic energy is equal to the stored electric energy ( $W_e = W_m$ ). When this occurs  $Z_{\text{in}} = R$ , which is a purely real impedance, and  $P_{\text{in}} = P_{\text{loss}}$ . The resonant frequency of the circuit can be determined from the condition  $W_e = W_m$  from which one finds that

$$\omega_0 = \frac{1}{\sqrt{LC}}. \quad (6.30)$$

An important performance parameter for any resonant system is the Q-factor, which quantifies the quality of the resonator as the ratio of the stored energy multiplied by the resonant frequency to the average energy lost per second. For the series RLC circuit, the Q-factor is given by the expression

$$Q_0 = \omega \frac{W_e + W_m}{P_{\text{loss}}} = \frac{1}{\omega_0 RC}, \quad (6.31)$$

from which one observes that as the resistance of the RLC circuit is decreased the quality factor of the resonator increases. From the perspective of cylindrical cavities this implies that as one decreases the resistance of the cavity walls it is expected that the Q-factor of the cavity should increase, which is indeed the case. In certain applications where a high Q is desireable it is possible to manufacture a cavity out of superconducting materials in order to minimize the power losses of the system.

The Q-factor of the resonator also determines with bandwidth (BW) of the system. A cavity with a high Q-factor will resonant with a smaller range of frequencies than a cavity with a low Q-factor. To see this we can examine the behavior of the RLC circuit when driven by frequencies near the resonance. For a frequency  $\omega = \omega_0 + \Delta\omega$ , where  $\Delta\omega = \omega - \omega_0 \ll \omega_0$ , we can write the input impedance as

$$Z_{\text{in}} = R + i\omega L \left( \frac{\omega^2 - \omega_0^2}{\omega^2} \right), \quad (6.32)$$

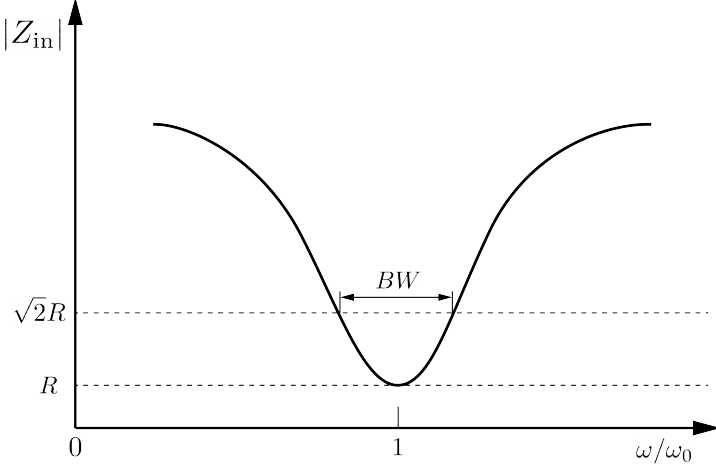


Figure 6.5: Illustration of the behavior of the input impedance of the series RLC circuit as a function of the driving frequency. The BW is proportion to the width of the resonance, which is inversely proportional to Q.

and by expanding  $(\omega^2 - \omega_0^2)/\omega^2$  to first order in  $\Delta\omega$ , we obtain

$$Z_{\text{in}} \approx R + i \frac{2RQ_0\Delta\omega}{\omega_0}. \quad (6.33)$$

Therefore, the magnitude of the input impedance near the resonance is given by

$$|Z_{\text{in}}| = R \sqrt{1 + 4Q_0^2 \frac{\Delta\omega^2}{\omega^2}}, \quad (6.34)$$

from which we observe that for the series RLC circuit the input impedance is minimized at the resonant frequency, which corresponds to the maximum input power (see Figure ??). The half-power BW is the range of frequencies over which the input power drops to half the input power on resonance. This occurs when  $|Z_{\text{in}}| = \sqrt{2}R$ , which corresponds to  $\Delta\omega/\omega = \text{BW}/2$ . Using Equation 6.34 one can find that

$$2R^2 = R^2(1 + Q_0^2\text{BW}^2), \quad (6.35)$$

which implies

$$\text{BW} = \frac{1}{Q_0} \quad (6.36)$$

It is important to emphasize that the Q-factor defined here,  $Q_0$ , is technically the unloaded Q. It reflects the quality of the cavity or resonant circuit without the influence of any external circuitry. In practice, however, a cavity is invariably coupled to an

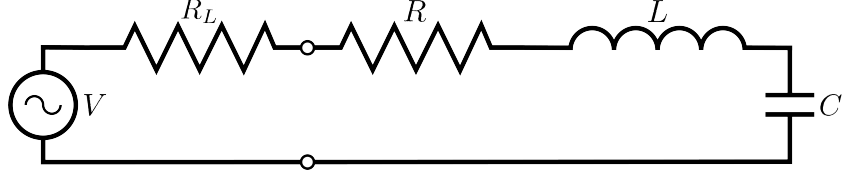


Figure 6.6: A series RLC circuit coupled to an external circuit with input impedance  $R_L$ .

external circuit to drive a cavity resonance or to measure the energy of a resonant mode. Coupling a cavity to an external circuit changes the Q by loading the equivalent cavity RLC circuit (see Figure 6.6). The Q-factor of the cavity when it is loaded by an external circuit is called the loaded Q, which is the quantity that one actually measures when exciting a resonance in the cavity. Using the series RLC circuit model one can see that the load resistor in Figure 6.6 will add in series with the resistor in the circuit for a total equivalent resistance of  $R + R_L$ . Therefore, the loaded Q is given by

$$Q_L = \frac{1}{\omega_0(R + R_L)C}, \quad (6.37)$$

from which one observes that the loaded Q is always less than the intrinsic Q of the cavity.

The amount of coupling that is desireable depends on the specific application of the resonator. If one wants a resonator that is particular frequency selective than it makes sense to limit the amount of coupling to the cavity to maintain a small BW, alternatively, if a larger BW is need one can increase the cavity coupling by tuning the input impedance of the external circuit. The critical point, where maximum power is transferred between the cavity and the external circuit, occurs when the input impedance of the cavity matches the input impedance of the external transmission line. For the series RLC circuit on resonance, this matching condition corresponds to

$$Z_0 = Z_{\text{in}} = R, \quad (6.38)$$

where  $Z_0$  is the impedance of the transmission line. The loaded Q at this critical point is, therefore,

$$Q_L = \frac{1}{2\omega_0 Z_0 C} = \frac{Q_0}{2}. \quad (6.39)$$

One can described the degree of coupling between the cavity and an external circuit by

defining a coupling factor,  $g$ , such that,

$$g = \frac{Q_0}{Q_L} - 1. \quad (6.40)$$

When  $g = 1$  then  $Q_L = Q_0/2$ , and the cavity is said to be critically coupled as we described. If  $Q_L < Q_0/2$ , then the cavity is undercoupled to the transmission line, corresponding to  $g < 1$ . Alternatively, if  $Q_L > Q_0/2$ , then  $g > 1$ , and the cavity is overcoupled to the transmission line. Various specialized circuits can be used to tune the input impedance of the external circuit as seen by the cavity to achieve a wide range of different coupling factors based on the desired application of the cavity.

## 6.3 The Cavity Approach to CRES

### 6.3.1 A Sketch of a Molecular Tritium Cavity CRES Experiment

Resonant cavities can be used to perform CRES measurements, and they represent the current preferred technology by the Project 8 collaboration for the ultimate goal of a 40 meV neutrino mass measurement using CRES. The basic approach to a neutrino mass measurement using a resonant cavity and molecular tritium beta-decay source is illustrated by Figure 6.7.

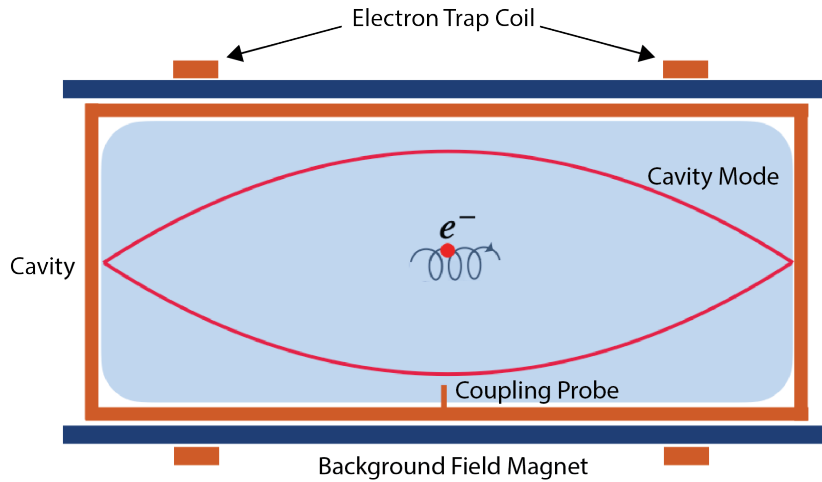


Figure 6.7: Cartoon depiction of a cavity CRES experiment.

At the core of the experiment is a large resonant cavity filled with tritium gas. In principle a sealed metallic cavity serves a dual purpose as the tritium containment vessel although the risks of exposure to radioactive tritium may necessitate a secondary

dielectric containment vessel (such as fused scilica) inside the cavity volume. The filled cavity is then placed in a uniform magnetic field provided by a primary magnet that sets the values of the cyclotron frequencies for electrons emitted with energies near the tritium spectrum endpoint. When a beta-decay electron is produced in the cavity it is trapped using an additional set of magnetic coils that prevents the electrons from running into the cavity walls.

Electrons trapped inside the cavity volume do not radiate in the same way as electron in free-space. Effectively, the same boundary conditions that were used to derive the resonant modes of a cylindrical cavity in Section 6.2 apply to the radiation of the electron as well. If an electron is emitted with a kinetic energy that corresponds to a cyclotron frequency that matches a resonant frequency of the cavity, then the power radiated by the electron excites the corresponding resonance in the cavity. The strength of the electron's coupling to the cavity is given by the dot product between the electrons trajectory and the electric field vector of the resonant mode. However, if an electron is moving with a cyclotron frequency that is far from any resonant modes in the cavity, then radiation from the electron is suppressed. One can interpret this somewhat surprising effect as the metallic walls of the cavity reflecting the radiated energy back into the electron.

To detect the electron the cavity is coupled to an external transmission line that leads to an amplifier and RF receiver chain similar to an antenna array based experiment. The coupling of the cavity resonance to the amplifier occurs through a coupling probe designed to resonate with the same mode or modes excited by the electron. In other resonant cavity systems this is often accomplished using a simple wire antenna, which could be connected to the amplifier through a segment of coaxial cable. Alternatively, cavities are oftentimes coupled to waveguides or smaller external cavities using small holes or apertures cut into the main cavity wall. For CRES measurements, the placement of a wire coupling probe inside the cavity volume leads to additional scattering of electrons and eventually tritium atoms, therefore, the apertures are the preferred coupling method for cavity CRES experiments.

One of the attractive features of the CRES technique for neutrino mass measurement is the gain in statistics that comes from the differential nature of the tritium spectrum measurement. Initially, this seems incompatible with cavities, due to the narrow resonances of cavity modes giving relatively small bandwidth. However, by intentionally overcoupling to a single cavity mode one can achieve bandwidths of a few 10's of MHz, which is sufficient for a measurement of the tritium spectrum endpoint region.

### 6.3.2 Magnetic Field, Cavity Geometry, and Resonant Modes

#### Magnetic Field and Volume Scaling

For a CRES experiment, cylindrical cavities are a natural choice since they match the geometry of standard solenoid magnets, which are needed in order to produce the background magnetic field for CRES measurements. Furthermore, the cylindrical shape is compatible with a Halbach array, which is the leading choice of atom trapping technology for future atomic tritium experiments by the Project 8 collaboration. Cylindrical cavities also benefit from well-established machining practices that are able to achieve high geometric precision at large lengths scales. Currently, a cylindrical cavity is the preferred cavity shape for CRES measurements by Project 8, although, there are on-going efforts to investigate more complicated cavity designs that may offer advantages over the more standard geometry.

As we saw in Section 6.2, the physical dimensions of the cavity are directly coupled to the resonant frequencies of the cavity. This dependency links the size of the cavity to the magnitude of the background magnetic field, because the magnetic field determines the cyclotron frequencies of trapped electrons. Specifically, as the size of the cavity is increased to accommodate larger volumes of tritium gas, the wavelengths and frequencies of the resonant modes increase and decrease respectively. This requires that the magnetic field also decrease in order to maintain coupling between electrons and the desired cavity mode.

The required cavity size is ultimately determined by the required statistics in the tritium spectrum endpoint region. Because the gas density must be kept below a certain level to ensure that electrons have sufficient time to radiate before scattering, larger volumes become the only way to achieve higher event statistics. To achieve the sensitivity goals of Phase III and IV cavity volumes on the order of several cubic-meters are required, which pushes one towards frequencies in the range of 100's of MHz.

#### Single-mode Cavity CRES

It is tempting to consider maintaining a high magnetic field while increasing the size of the cavity in order to increase the radiated power from trapped electrons for a potentially better SNR. However, if one were to maintain the same magnetic field while increasing the size of the cavity, the electrons would begin to couple to higher order modes with more complicated transverse geometries. The danger with this approach is that a complicated mode structure could introduce systematic errors into the CRES signals, for example

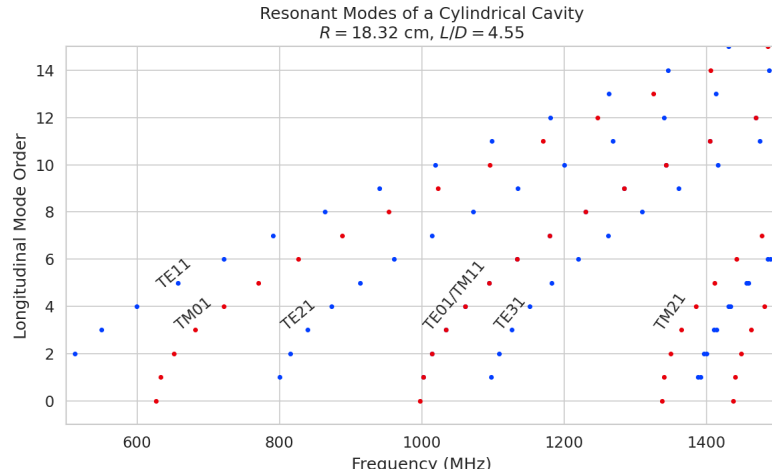
by unpredicted mode hybridization or changes in the mode shapes from imperfections in the cavity construction, that would prevent reconstruction of the electron's starting kinetic energies with adequate resolution. For this reason, it may be ideal to operate with magnetic fields that give cyclotron frequencies near the fundamental frequency of the cavity, where the mode structure is relatively simple. In this frequency region it may be possible to perform CRES by coupling to only a single resonant mode, however, it is currently an open question if a single mode measurement will provide enough information about an individual electron to reconstruct the full event. Regardless, developing a solid understanding of the CRES phenomenology when an electron is coupling to a single mode will be a necessary step towards a future multi-mode cavity experiment.

### Considerations for Resonant Mode Selection

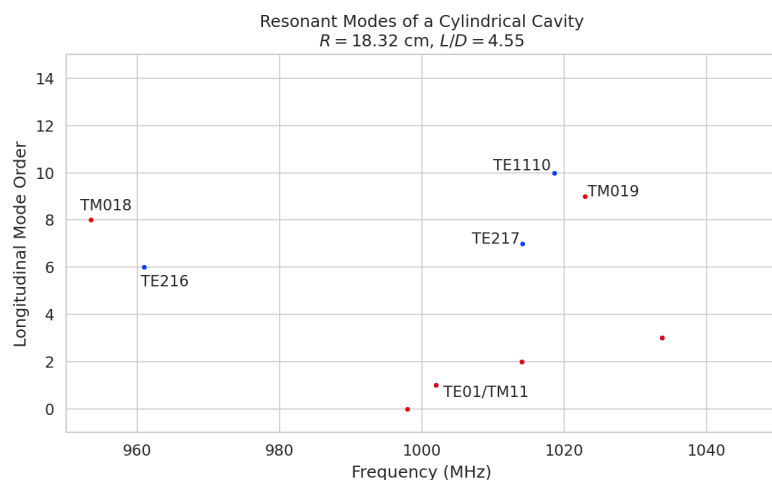
The design of a single-mode cavity experiment begs the question of which resonant mode is best for CRES measurements. There is an immediate bias towards low order  $\text{TE}_{nm}$  and  $\text{TM}_{nm}$  modes due to the multi-mode considerations discussed above. Additionally, there is a preference towards modes with longitudinal index  $\ell = 1$  with a single antinode along the vertical axis of the cylindrical cavity. The reason for this is that there is a phase change in the electric fields between antinodes that could lead to interference effects that destroy signal information when an electron is moving between antinodes.

A second consideration for mode selection is the volumetric efficiency of the mode. Volumetric efficiency can be thought of as an integral over the volume of the cavity weighted by the relative amplitude of the mode. From the perspective of simply maximizing the volume useable for CRES measurements this integral would be as close to unity as possible. However, there is a requirement to reconstruct the position of the electrons inside the cavity volume so that the local magnetic fields can be used to convert the measured cyclotron frequency to a kinetic energy. With a single mode this necessarily requires a variable transverse mode amplitude, which lowers the volumetric efficiency, so that position of the electron in the cavity can be estimated from the average amplitude of the CRES signal. Longitudinal indices of  $\ell = 1$  have an advantage in volumetric efficiency over higher order  $\ell$  modes, since there are only two longitudinal nodes, one at each end of the cavity. Therefore, the average coupling strength of trapped electrons as they oscillate axially is higher for  $\ell = 1$  modes.

The longitudinal variation in the mode strength is ultimately critical for achieving the energy resolution required for neutrino mass measurements. Correcting for the change in the average magnetic fields experienced by electrons with different pitch angles requires



(a)



(b)

Figure 6.8: Examples of the resonant mode frequencies of a cylindrical cavity.

that information on the axial motion of the electron be encoded into the CRE signal. The longitudinal variation in the mode amplitude leads to amplitude modulation of the CRE signal with a frequency proportional to the electron's pitch angle.

An additional factor for mode selection is the intrinsic or unloaded  $Q$  of the mode. In terms of SNR it is advantageous to use a mode with a very high  $Q_0$ , which is then highly overcoupled to achieve the necessary bandwidth to cover the tritium endpoint spectrum. This scheme leads to a decoupling of the physical cavity temperature from the effective noise temperature after the amplifier, which allows us to achieve adequate SNR without the requirement of cooling the entire cavity to single Kelvin temperatures.

An example of a resonant mode that exhibits these traits is the  $\text{TE}_{01}$  mode. At present

the  $\text{TE}_{011}$  mode is the preferred resonance for a single-mode cavity CRES experiment by the Project 8 collaboration.  $\text{TE}_{011}$  is a low order mode located in a region relatively far from other cavity modes. Furthermore, the separation of the  $\text{TE}_{011}$  mode can be improved by various mode-filtering techniques discussed in Section 6.4.2 below.  $\text{TE}_{011}$  consists of a single longitudinal antinode that can provide pitch angle information in the form of amplitude modulation, and has an electric field with a radial profile given by the  $J'_0$  Bessel function allowing for radial position estimation. Lastly, the  $\text{TE}_{011}$  mode has a relatively high intrinsic Q compared to nearby modes, which helps with SNR. Unloaded Q's greater than 80000 are achievable for a 1 GHz  $\text{TE}_{011}$  resonance using a copper walled cavity.

### 6.3.3 Trade-offs Between the Antenna and Cavity Approaches

The choice between cavities and antennas for large-scale CRES measurements is not without trade-offs. While both the antenna array and cavity approach are in their technical infancy, at present there are no known obstacles that would prevent either approach from being used for a large scale neutrino mass measurement. The emergent preference for cavities is partly driven by important practical considerations that could make a cavity based experiment significantly cheaper than an antenna experiment of similar size and scope. However, the switch to cavities also introduces new challenges less relevant to the antenna array, which must be solved in order for Project 8 to achieve its neutrino mass measurement goals.

One of the major drawbacks of the antenna array approach compared with the cavity is the size and complexity of the data-acquisition system. A large-scale antenna array experiment would require  $O(100)$  antennas all independently digitized at rates of  $O(10)$  to  $O(100)$  MHz. Since there is insufficient information in a single antenna channel to detect or reconstruct the CRES signal, the entire array output must be processed during the signal reconstruction. Because data storage becomes an issue with these data volumes, there is a requirement for some form of real-time signal reconstruction capable of detecting CRES signals buried in the thermal noise. As we discuss in Section 4.4, the computational cost of these real-time detection algorithms are potentially quite large for even a small scale antenna array experiment. However, the operating principle of a cavity experiment allows the CRES signal to be detected using only a single read-out channel digitized at rates of  $O(10)$  MHz, which reduces the cost of the data acquisition system by many orders of magnitude.

From an engineering perspective, the simple geometry and thin-walls of a cylindri-

cal cavity are much simpler to interface with the cryogenic and magnetic subsystems required for a CRES experiment. Whereas, the antenna array requires careful design and engineering to accommodate the antenna array and receiver electronics in proximity to the electron and eventually atom trapping magnets. Additionally, due to near-field interference effects the antenna array is unable to reconstruct CRES events within the reactive near-field distance of the antennas. Because atom trapping requirements require magnetic fields which correspond to cyclotron frequencies for endpoint electrons less than 1 GHz, the required stand-off distance leads to a significant loss in useable experiment volume, necessitating larger and more expensive magnets.

Another advantage to the cavity approach is the relatively compact sideband structure, which is a result of the low modulation index for cavity CRES signals. The axial motion in an antenna array experiment leads to frequency modulation and sidebands. The shape of the sideband structure is determined by the modulation index,  $h = \frac{\Delta f}{f_a}$ , where  $\Delta f$  is the size of the frequency deviation and  $f_a$  is the axial frequency. The large electron traps required for a cubic-meter-scale experiment leads to high modulation indices, which causes the signal spectrum to be made up of numerous low power sidebands that make reconstruction and detection challenging. This behavior was observed in simulations of the FSCD in which carrier power decreased with pitch angle due to the increase in modulation index (see Figure 4.19). For cavities, however, the modulation index remains near  $h = 1$  even for very long magnetic traps due to the high phase velocity in cavities relative to the axial velocity of the electron. This results in an almost ideal spectrum shape that has a strong carrier frequency with a few sidebands whose relative amplitudes encode pitch angle information.

A potential downside of the cavity approach is the apparent difficulty of estimating the position of the electron using only the coupling of the electron to a single mode. The amplitude of the  $TE_{011}$  mode is completely independent of the azimuthal coordinate, therefore, position reconstruction using the  $TE_{011}$  mode is only able to estimate the radial position of the electron. This position degeneracy may lead to magnetic field uniformity requirements that are extremely challenging to meet due to mechanical uncertainties in cavity and magnet construction, as well as uncertainties caused by nuisance external magnetic fields such as the Earth's field and magnetic fields from building materials. A multi-mode cavity experiment may provide a way to extract more precise information on the position of the electron by analyzing the coupling of the electron to several modes that overlap in different ways.

## 6.4 Single-mode Resonant Cavity Design and Simulations

The single-mode cylindrical cavities envisioned for the Phase III and IV experiments must be carefully engineered in order to measure the neutrino mass with the desired sensitivity. In this section I summarize some simulation studies performed to analyze early design concepts for a single-mode cavity. The primary tool for these investigations was Ansys HFSS, which was also used for the development of the SYNCA antenna described in Section 5.3.

### 6.4.1 Open Cylindrical Cavities with Coaxial Terminations

#### Design Concept

A basic cavity design question relevant to Project 8's ultimate goal of an atomic tritium CRES experiment is how to build a cavity that can be efficiently filled with atomic tritium. To keep the rate of atom loss from recombination on surfaces it is ideal if the ends of the cylindrical cavity are as open as possible so that tritium atoms can flow inside unimpeded. Additionally, one of the primary calibration techniques planned for future CRES experiments involves CRES measurements using electrons injected from an electron gun source, which also requires an openings at the cavity ends. Cylindrical cavities with open ends can be manufactured, however, the intrinsic Q-factors of these cavities are orders of magnitude less than their sealed counterparts, which reduces the signal-to-noise ratio when that cavity is used for CRES measurement.

Cylindrical cavities with mostly open ends that also exhibit Q values for the  $TE_{01\ell}$  modes similar to sealed cavities can be built by using coaxial endcaps to terminate the cavity. Cavities of this type have been manufactured for specialized applications related to the measurements of the dielectric constants of liquefied gasses (see Figure 6.9). This cavity design leaves the ends of the cavity wide open, but retains high Q-values for the  $TE_{01\ell}$  modes due to the coaxial endcap, which are designed to perfectly reflect the electric fields of  $TE_{01\ell}$  modes. Coupling to the  $TE_{01\ell}$  mode is achieved via an aperture located at the center of the cavity wall.

A cavity similar to Figure 6.9 is a candidate design for the future CRES experiments by Project 8, since it appears to elegantly solve many practical issues that arise when combining cavity CRES and atomic tritium. The coaxial endcaps leave significant regions of the cavity ends completely open, which allows for the entrance of atomic tritium as well as the pumping away of molecular tritium that has recombined on the cavity walls.

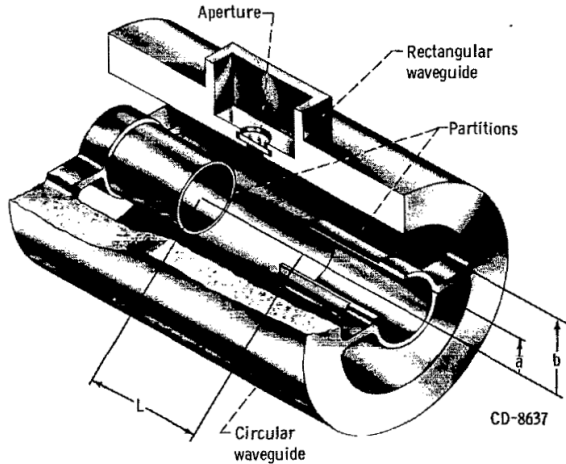


Figure 6.9: An image of an open cavity with coaxial terminations used for dielectric constant measurements. Figure from ??

These open ends are achieved while preserving the high Q-values of the  $\text{TE}_{01\ell}$  modes, which is important for extracting as much signal power from the electron as possible. In subsequent sections we shall analyze this cavity design in more detail, primarily by using HFSS simulations to analyze the resonant mode structure of this cavity geometry.

### Coaxial Terminator Constraints

The reason that coaxial endcaps can be used to achieve high Q-values for the  $\text{TE}_{01\ell}$  modes is that the electric fields for these modes are purely azimuthally polarized (see Equations 6.12 and 6.13). Therefore, the boundary conditions that require the electric field to go to zero at the cavity ends can be supplied using a coaxial partition of the correct radius (see Figure 6.10). Because the cylindrical shape enforced by the partition does not match the boundary conditions of other cavity modes, these terminations also significantly suppress the Q-factors of non- $\text{TE}_{01\ell}$  modes, which is potentially beneficial for a single-mode cavity CRES experiment.

The correct radius of the cylindrical partition can be derived by setting up the boundary value problem in Figure 6.10, and analyzing the reflection and transmission coefficients for waves incident on the coaxial terminators. The basic problem is to identify the radius  $a$  at which the reflection coefficient for the  $\text{TE}_{01\ell}$  modes is equal to 1. One can show that if the coaxial partitions are made sufficiently long relative to the wavelength of the  $\text{TE}_{01}$  modes than perfect reflection can be achieved. This derivation is quite lengthy and complex and is presented in full in reference ?. Here, we shall simply explain the

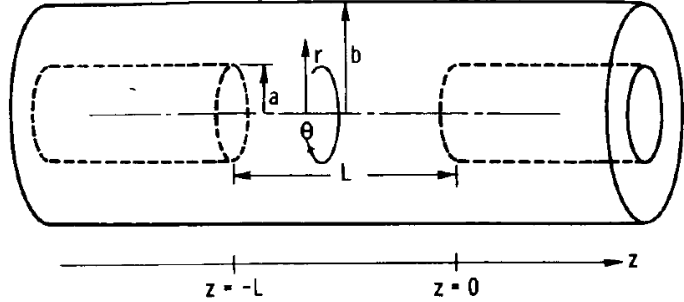


Figure 6.10: The simplified geometry of an open cavity with coaxial terminations. Figure from ??

resulting conditions on the partition radius for perfect reflection.

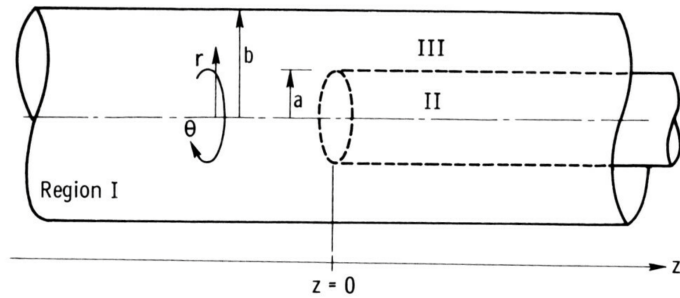


Figure 6.11: Electric field regions for the open cavity boundary value problem.

The open cavity boundary value problem is solved by expressing the forms of the electric fields in the different regions of the cavity and requiring that the electric fields are continuous. There are effectively three distinct regions in the open cavity corresponding to the central cavity volume, the inner coaxial volume, and the outer coaxial volume (see Figure 6.11).

In Region I the boundary conditions are those of a cylindrical waveguide, and we require that  $E_\phi$  for the  $\text{TE}_{0m}$  modes go to zero at the cavity wall ( $r = b$ ). This requires that  $J'_{0m}(k_{c0m} b) = 0$ . We aim to solve for the radius  $a$  in the specific situation where the  $\text{TE}_{01}$  mode can propagate but all other  $\text{TE}_{0m}$  modes are below the cutoff frequency for the circular waveguide. This is equivalent to requiring

$$3.832 < k_{c0m} b < 7.016, \quad (6.41)$$

where the numbers 3.832 and 7.016 correspond to the first and second zeros of the Bessel function (see Table 6.1).

In Region II the boundary conditions are also those of a cylindrical waveguide, but with a new, smaller radius. The condition that  $E_\phi = 0$  at the cylindrical partition radius is that  $J'_{0m}(k_{c0m}a) = 0$ . To ensure perfect reflection we want all modes in Region 1 of the cavity to be below the cutoff frequency of the circular waveguide formed by the inner volume of the coaxial terminator. Therefore, we consider the solutions where

$$k_{c0m}a < 3.832. \quad (6.42)$$

Finally, in Region III the boundary condition are those of a coaxial waveguide. We need to guarantee that  $E_\phi = 0$  at both  $r = b$  and  $r = a$ , which involves finding the eigenvalues of the following equation

$$J'_0(k_{c0m}a)Y'_0(k_{c0m}b) - J'_0(k_{c0m}b)Y'_0(k_{c0m}a) = 0, \quad (6.43)$$

where  $Y'_0$  the zeroth-order derivatives of the Bessel function of the second kind. The solutions to this equation depend on the value of the ratio  $b/a$ . The approximate solution is given by

$$\delta_n a \simeq \frac{n\pi}{b/a - 1}, \quad (6.44)$$

where  $\delta_n$  are eigenvalues of Equation 6.43. Similar to Region II, we are interested in solutions for which the TE<sub>01</sub> modes of Region I are below the cutoff of Region III. Therefore, we require that

$$k_{c0m} < \delta_1. \quad (6.45)$$

In general, one has some freedom in specifying the value of  $b/a$ . A value typically used in practice is  $b/a = 2.082$ , which corresponds to positioning the radius of the cylindrical partition at the maxima of the TE<sub>01</sub> electrical fields.

Using the constraints from the three field regions one can develop a coaxial terminator that acts as a virtual perfectly conducting surface for the TE<sub>01</sub> modes. The only required inputs are the desired frequency of the TE<sub>011</sub> mode and a choice for the value of  $b/a$ .

### 6.4.2 Mode Filtering

The general case of an electron coupling to a resonant cavity can quickly be come quite complicated. This is because cavities contain an infinite number of resonant modes that at higher orders have a coupling to the electron with a complex spatial dependence. The danger is that improper modeling of the electron's coupling to the cavity can lead to

systematic errors in the CRES measurements that prevent a high enough resolution measurement of the electron's kinetic energy. This in part drives the preference for a single-mode cavity experiment that uses only the electron's coupling to the  $\text{TE}_{011}$  mode to perform CRES. If sufficient information on the electron's position can be obtained with only this mode then this represents the ideal case.

The  $\text{TE}_{011}$  mode is in a region where there are relatively few other modes to which the electron could couple (see Figure 6.8). However, one can see that the frequency of the  $\text{TE}_{011}$  is perfectly degenerate with the  $\text{TM}_{111}$  mode, which means that electrons will inevitably couple to both modes if they have the correct cyclotron frequency.

The magnitude of the impact of the electron coupling to both  $\text{TE}_{011}$  and  $\text{TM}_{111}$  is currently unknown. To first order an electron coupling to more both modes will lose more energy overtime, which can be measured by observing the frequency chirp rate of the signal. This effect may be small enough to be negligible or simple enough to model that the cavity can be treated as an effective single-mode cavity. Alternatively, the one could consider devising a coupling scheme that is sensitive to both the  $\text{TE}_{011}$  and the  $\text{TM}_{111}$  modes. By measuring the coupling of the electron to both modes more information on the position of the electron could be obtained, which might improve the position and energy resolution of the CRES measurements.

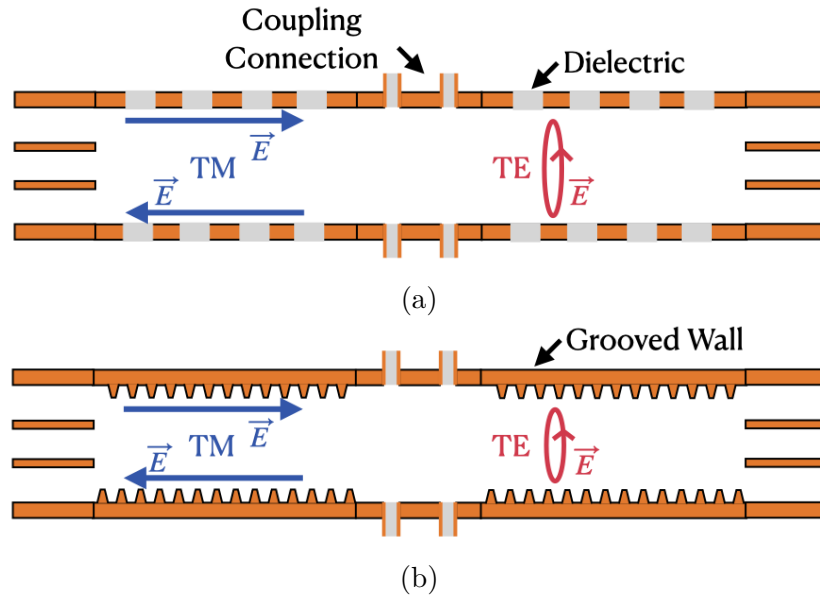


Figure 6.12: Two mode filtering concepts to break the degeneracy of  $\text{TE}_{01}$  and  $\text{TM}_{11}$  modes.

A different approach is the mode filtering approach, which seeks to obtain a true

single  $TE_{011}$  mode cavity by using perturbations to the cavity walls that selectively impede the TM modes, while leaving the TE modes mostly unperturbed. The type of perturbations required can be determined by visualizing the surface currents induced in the cavity walls by each type of mode (see Figure 6.12). By definition, all TM have electric fields directed along the vertical axis of the cylindrical cavity, which means that perturbations that impede currents in this direction will modify TM resonances. On the other hand, the  $TE_{01}$  modes induce azimuthal currents in the cavity walls, therefore, it is possible to break the degeneracy between  $TE_{01}$  and  $TM_{11}$  using a cavity perturbation that impedes axial currents, but does not affect the flow of azimuthal currents.

Figure 6.12 shows two cavity design concepts that achieve this selective current perturbation. The resistive approach inserts a series of thin dielectric rings into the walls of the cavity that introduces a resistive and capacitive impedance to the longitudinal currents, while leaving azimuthal current paths intact. Cavities of this type with high  $TE_{01}$  Q's have also been constructed by tightly wrapping a thin, dielectric coated wire around a mold to form the cavity wall. An alternative method is to introduce an inductive impedance by cutting grooves or a thread pattern on the inside wall of the cavity. For reasons of manufacturability and compatibility with tritium the grooved cavity approach is the preferred method for mode-filtered cavity construction by Project 8.

### 6.4.3 Simulations of Open, Mode-filtered Cavities

The ideal cavity design for a single  $TE_{011}$  mode CRES experiment is potential a cavity that utilizes the coaxial terminations with a mode-filtering wall. The first step towards validating that a cavity that combines these two design features will operate as expected is a thorough simulation effort for which finite element method (FEM) simulation software is invaluable. The primary tool for electromagnetic FEM calculations inside Project 8 is Ansys HFSS, which has a robust and well-established eigenmode solver that can identify the resonant frequencies and associated Q-factors for given structure.

Four variations of a cavity design with a  $\sim 1$  GHz  $TE_{011}$  resonance were implemented in HFSS (see Figure 6.13). The four designs include a standard cylindrical cavity, an open cavity with smooth walls, an open cavity with resistive walls, and an open cavity with grooved walls. The relevant design parameters are summarized in Table 6.3. All cavities were simulated using copper walls and filled with a vacuum dielectric. The identities of the resonant modes found by HFSS were validated by visual inspection of the electric and magnetic field patterns and by comparison to analytical calculations of the mode frequencies.

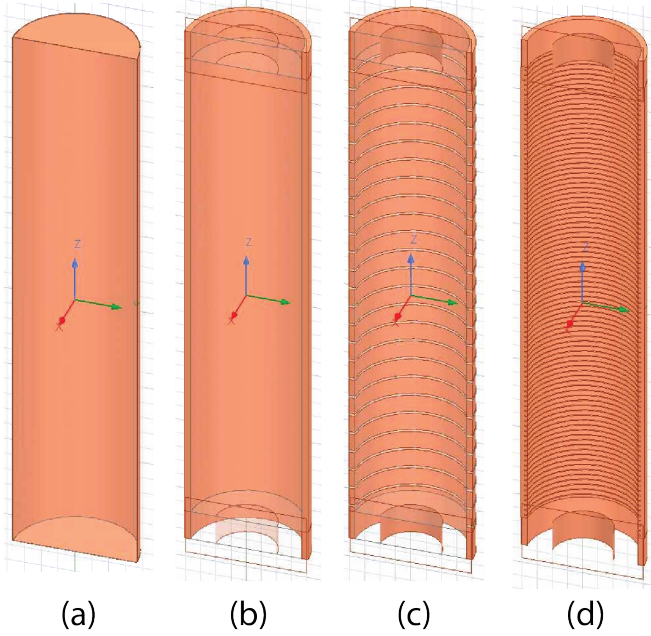


Figure 6.13: Four cavity design variations. (a) is a standard sealed cylindrical cavity, (b) is an open cavity with smooth walls, (c) is an open cavity with resistive walls, and (d) is an open cavity with grooved walls. The main cavity and coaxial terminator parameter are identical for all four cavities.

Table 6.3: A table of cavity design parameters used for HFSS simulations.

Name	Qty.	Unit	Description
$D_{\text{cav}}$	326.4	mm	Cavity diameter
$L_{\text{cav}}$	1668.0	mm	Cavity length
$D_{\text{term}}$	200.2	mm	Inner diameter of coaxial terminator
$L_{\text{term}}$	100.0	mm	Terminator length
$l_{\text{die}}$	8.3	mm	Dielectric spacer thickness
$\Delta l_{\text{die}}$	66.7	mm	Distance between dielectric spacers
$l_{\text{groove}}$	3.0	mm	Groove height
$d_{\text{groove}}$	9.0	mm	Groove depth
$\Delta l_{\text{groove}}$	18.3	mm	Distance between grooves

The results of the HFSS simulations validate our predictions of the resonant behavior of an open, mode-filtered cavity developed in the preceding sections (see Figure 6.14). The resonant modes of the standard cavity agree well with analytical calculations for the resonant frequencies of cylindrical cavities. One can see that for a standard cavity the  $\text{TE}_{01}$  and the  $\text{TM}_{11}$  are degenerate in frequency with relatively high Q-factors. The open ended cavity preserves the high Q-factors of the  $\text{TE}_{01}$  modes, while the other modes, since their boundary conditions do not match the coaxial geometry, have their Q-factors

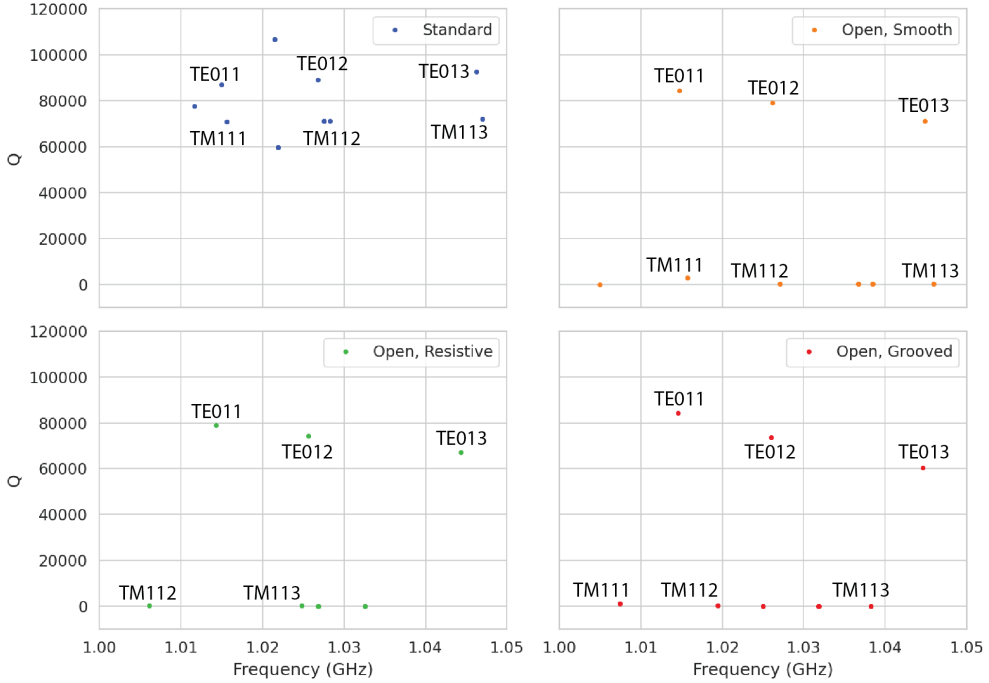


Figure 6.14: The frequencies and Q-factors of the resonant modes identified by HFSS for the cavity variations shown in Figure 6.13.

suppressed. One can see that the effect of the resistive and inductive mode-filtering schemes is to effectively shift the resonant frequencies of the TM<sub>11</sub> modes below those of the associated TE<sub>01</sub> modes, which breaks the degeneracy. Optimization of the dielectric spacer or groove parameters can ensure that the TE<sub>011</sub> mode is isolated from other modes by  $O(10)$  MHz, which provides sufficient bandwidth for a measurement of the tritium spectrum endpoint.

Further optimization of the cavity design requires a more detailed cavity simulation that includes the cavity coupling mechanism as well as other geometry modifications required for integration into the magnetic and tritium gas subsystems. Perhaps more important is the development of the capability to simulate the interaction of electrons with the cavity so that simulated CRES signals can be generated using cavities designed for CRES measurements. Simulated CRES signals can then be used to estimate the neutrino mass sensitivity of the experiment, which allows for the optimization of the cavity design towards the configuration that provides the best measurement of the neutrino mass.

## 6.5 Single-mode Resonant Cavity Measurements

Laboratory prototyping of cavities and measurement test stands play an important role in the research and development process that cannot be replaced by simulations. For example, constructing a prototype of a CRES measurement cavity forces one to consider important practical issues such as manufacturability and machine tolerances that may require modifications to the design. Furthermore, by comparing laboratory measurements of the resonant behavior of a real cavity to simulations of the cavity, one can quantify the impact of mechanical tolerances, which allows for more accurate sensitivity estimates of the experiment. Lastly, the development of these prototypes helps to build the necessary experience and expertise within the collaboration required for more complicated experiments to succeed.

In this spirit a prototype cavity was constructed to demonstrate the open, mode-filtered cavity concept explored in the previous sections. The primary goal of the measurements was to validate that an open, mode-filtered cavity suppressed the TM<sub>11</sub> modes as predicted by HFSS simulations.

### 6.5.1 Cavities and Setup

Two rudimentary, cavities were constructed using segments of copper pipe available from McMaster-Carr (see Figure 6.15). The design consists of copper pipes of two diameters. The larger diameter pipe forms the main cavity wall and the smaller diameter pipe is used to create a coaxial termination. The diameter of the outer pipe was chosen to produce a TE<sub>011</sub> resonance of approximately 6 GHz, while the diameter of the smaller pipe was selected based on the open termination criteria introduced in Section 6.4.1. The

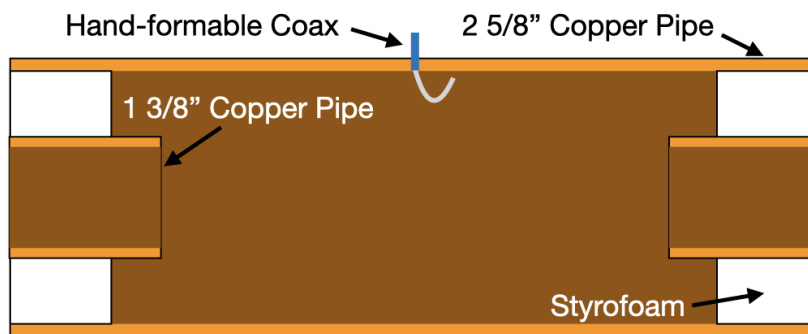


Figure 6.15

approximate diameters and lengths of the copper pipe are summarized in Table 6.4.

Coupling to the cavity was achieved using a hand-formable segment of coaxial cable stripped at one end to form a loop antenna. This was inserted into a small hole located at the center of the main cavity wall. The coaxial terminators were supported inside the main cavity by carving a spacer from polystyrene foam (styrofoam) so that they could be easily inserted into the cavity and repositioned. The dielectric constant of styrofoam is quite close to air at microwave frequencies so this is expected to have minimal impact on the resonant properties of the cavity.

Table 6.4: A table of parameters describing the cavity prototypes. Certain values such as the cavity length and the distance between dielectric spacers are approximate due to variation in the machining of the copper. In particular, the filtered cavity was constructed from conducting copper segments that varied in size from 1.50" to 1.85".

Name	Qty.	Unit	Description
$D_{\text{cav}}$	2.625	in	Cavity diameter
$L_{\text{cav}}$	$\approx 13$	in	Cavity length
$D_{\text{term}}$	1.375	in	Inner diameter of coaxial terminator
$L_{\text{term}}$	1.575	in	Terminator length
$l_{\text{die}}$	0.75	in	Dielectric spacer thickness
$\Delta l_{\text{die}}$	$\approx 1.50$ to $1.85$	in	Distance between dielectric spacers

The actual length of the cavity is given by the distance between the inner edges of the coaxial terminations. The length of the outer section of pipe that forms the main wall of the cavity is approximately 16" in length which leads to a cavity length of  $\approx 13$ " when both terminators are inserted in the cavity. Because the terminators were not rigidly mounted this distance is only approximate, however, the uncertain length of the cavity will not prevent us from validating the open cavity design.

Along with the smooth-walled open cavity a resistively mode-filtered cavity was constructed by creating dielectric spacers out of segments of clear PVC pipe (see Figure 6.16). The spacers were machined such that the conductive segments of the cavity would be separated by 0.75" when the cavity was fully assembled. Due to variations in the lengths of the copper segments that make up the cavity wall the distance between spacers has significant variation with average value of about 1.7". Eight total spacers were used to build the cavity, which when assembled was approximately 16" in total length similar to the non-filtered cavity.

Measurements of both cavities were performed using a VNA connected to the cavity coupling probe (see Figure 6.16). By measuring the return loss over a range of frequencies one can measure the frequencies and relative Q-factors of the resonant modes in the cavity. Due to the opposite polarity of the electric fields for the TE and TM modes,

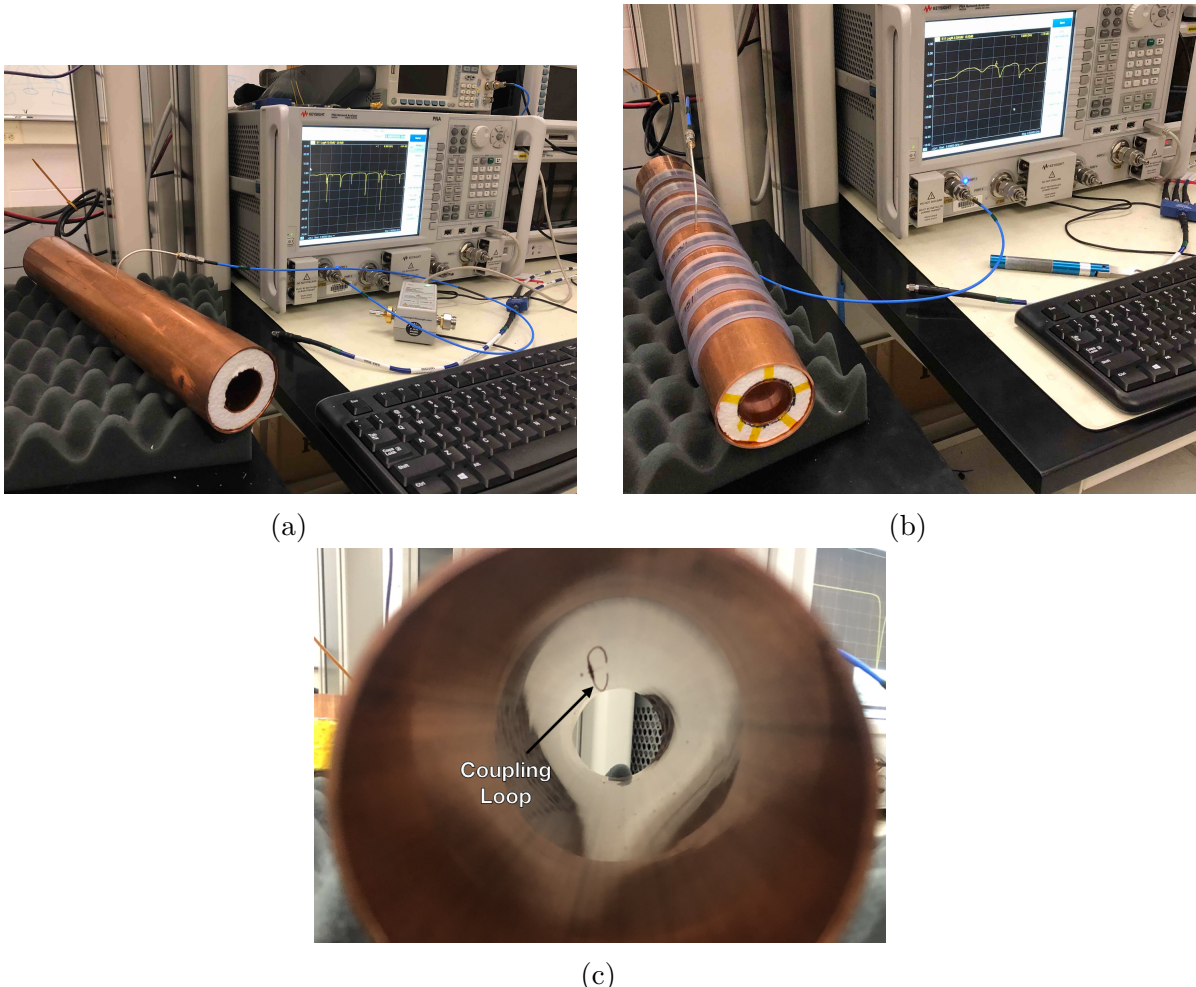


Figure 6.16: Images depicting the measurement of the filtered and non-filtered open cavities using the VNA. The coupling loop in the figure is shown in the TE orientation.

the loop coupling probe must be rotated  $90^\circ$  to change the polarity of the loop antenna. When the antenna is oriented such that the loop opening faces the ends of the cavity, it couples primarily to the TE modes which have magnetic fields directed along the long axis of the cavity (see Figure 6.16). If the coupling loop is turned by  $90^\circ$  from where it is shown in the image then it will couple to the TM modes which have azimuthally directed magnetic fields. In this way both the TE and TM resonances can be measured independently.

### 6.5.2 Results and Discussion

The primary analysis method for the prototype cavities involved simply visualizing the return loss measured by the VNA and comparing between the filtered and non-filtered

cavities. Since the resonances measured by the VNA are not labeled, there is some uncertainty about the true identities of the modes measured by the VNA. To help with this we performed a simulation of the simplest possible cavity that could be created from the prototype components, which is a fully open cavity created by simply removing the coaxial inserts from the non-filtered cavity configuration. The fully open cavity with the as-built dimensions was simulated in HFSS to get estimates on the positions of the  $\text{TE}_{011}$  and  $\text{TM}_{111}$  modes (see Figure 6.17).

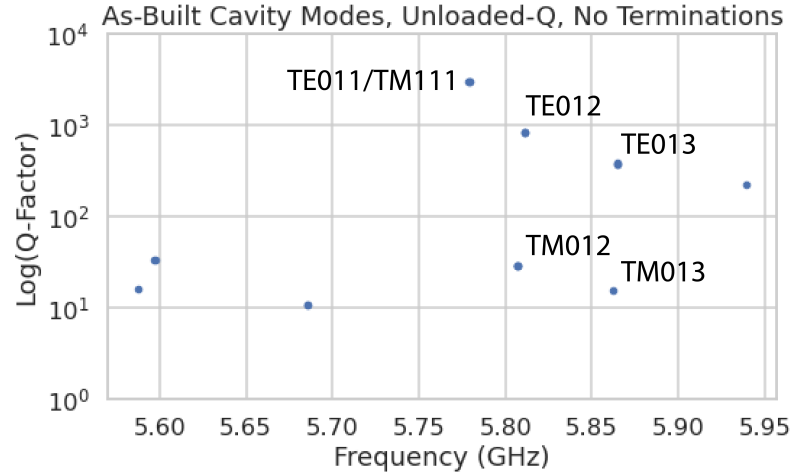


Figure 6.17: HFSS simulation results for a the as-built cavity with the coaxial terminators removed. The  $\text{TE}_{011}/\text{TM}_{111}$  frequency is approximately 5.78 GHz.

Simulation of the fully open cavity shows that the  $\text{TE}_{011}/\text{TM}_{111}$  modes have a frequency of approximately 5.78 GHz in the fully open cavity. If the frequency of this mode is compared to the measurements of the filtered and non-filtered cavities with the terminators removed we can easily identify the  $\text{TE}_{011}$  mode at approximately 5.75 GHz (see Figure 6.18).

For the non-filtered cavity one sees that the  $\text{TE}_{011}$  mode is degenerate in frequency with what appears to be a doublet of TM modes located at the  $\text{TM}_{111}$  frequency position. This doublet is actually the  $\text{TM}_{111}$  mode, which has two polarizations with opposite polarizations. Because the pipe used to construct the cavity is not perfectly round, the frequency degeneracy between the two polarizations is broken producing the doublet peak. In the case of the filtered cavity with no terminators there is an isolated TE resonance at 5.75 GHz that appears to be the  $\text{TE}_{011}$ , however, there is no apparent  $\text{TM}_{111}$  doublet at the same frequency. This is what one would expect if the mode-filtering was effective at suppressing the TM modes. There is a notable difference in the Q of the

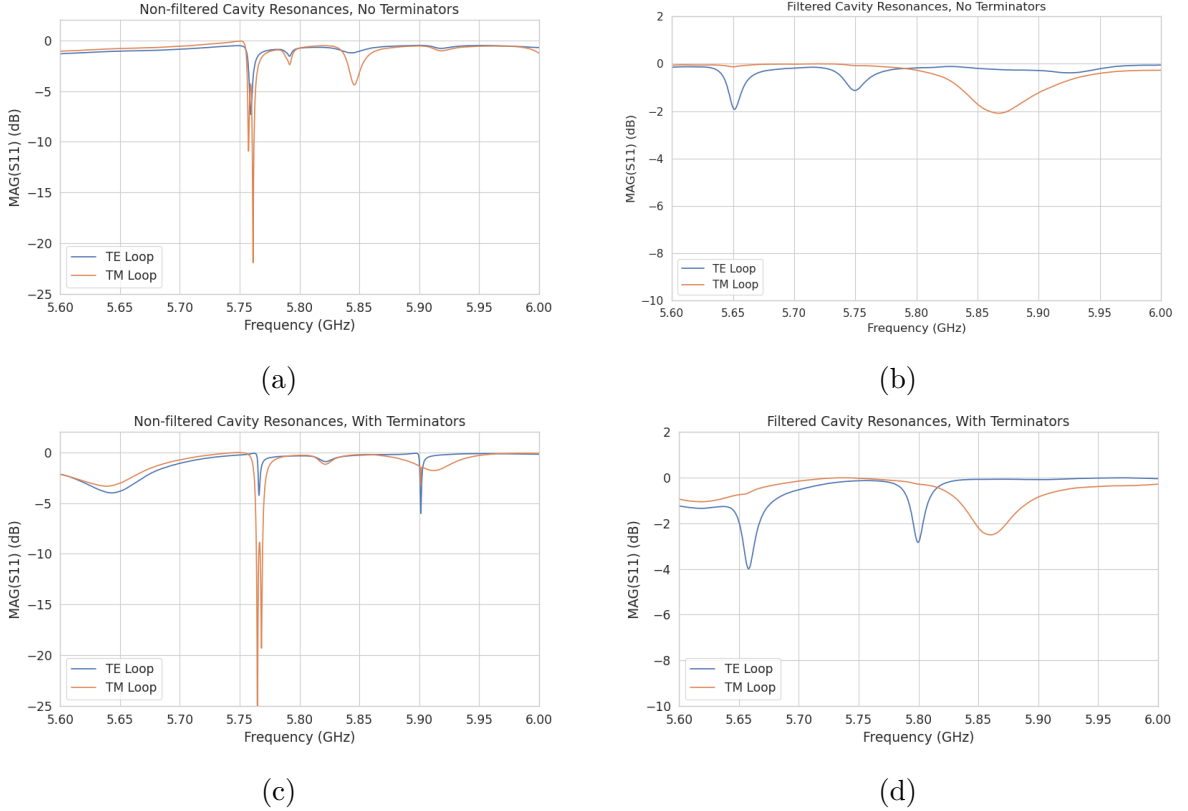


Figure 6.18: Measurements of the filtered and non-filtered prototype cavities acquired with the VNA.

TE<sub>011</sub> resonance for the non-filtered and filtered cavities indicated by the relative widths of the resonances. This is likely caused by the large width of the dielectric spacers that are partially impeding the TE modes. When the terminators are inserted into the cavity one sees that Q-factors of the modes improves as expected, by noticing the narrowing of the peaks compared to the no terminator plots.

In conclusion, one sees from these cavity measurements that, in principle, mode-filtering can be used to separate the TE<sub>011</sub> resonance from the degenerate TM<sub>111</sub> mode in combination with the open cavity design. The ideal next step would be to construct an open, mode-filtered cavity that could be used to perform CRES measurements. In order to study the coupling of an electron to the isolated TE<sub>011</sub> mode.

# Bibliography

- [1] FURSE, D. ET AL. (2017) “Kassiopeia: a modern, extensible C++ particle tracking package,” *New Journal of Physics*, **19**(5), p. 053012.  
URL <https://doi.org/10.1088/1367-2630/aa6950>
- [2] MONREAL, B. and J. A. FORMAGGIO (2009) “Relativistic cyclotron radiation detection of tritium decay electrons as a new technique for measuring the neutrino mass,” *Phys. Rev. D*, **80**, p. 051301.  
URL <https://link.aps.org/doi/10.1103/PhysRevD.80.051301>
- [3] ESFAHANI, A. A., S. BÖSER, N. BUZINSKY, M. C. CARMONA-BENITEZ, C. CLAESSENS, L. DE VIVEIROS, P. J. DOE, M. FERTL, J. A. FORMAGGIO, J. K. GAISON, L. GLADSTONE, M. GRANDO, M. GUIQUE, J. HARTSE, K. M. HEEGER, X. HUYAN, J. JOHNSTON, A. M. JONES, K. KAZKAZ, B. H. LAROQUE, M. LI, A. LINDMAN, E. MACHADO, A. MARSTELLER, C. MATTHÉ, R. MOHIUDDIN, B. MONREAL, R. MUELLER, J. A. NIKKEL, E. NOVITSKI, N. S. OBLATH, J. I. PEÑA, W. PETTUS, R. REIMANN, R. G. H. ROBERTSON, D. R. D. JESÚS, G. RYBKA, L. SALDAÑA, M. SCHRAM, P. L. SLOCUM, J. STACHURSKA, Y. H. SUN, P. T. SURUKUCHI, J. R. TEDESCHI, A. B. TELLES, F. THOMAS, M. THOMAS, L. A. THORNE, T. THÜMMLER, L. TVRZNIKOVA, W. V. D. PONTSEELE, B. A. VANDEVENDER, J. WEINTROUB, T. E. WEISS, T. WENDLER, A. YOUNG, E. ZAYAS, and A. ZIEGLER (2023) “Tritium Beta Spectrum and Neutrino Mass Limit from Cyclotron Radiation Emission Spectroscopy,” [2212.05048](https://arxiv.org/abs/2212.05048).
- [4] ESFAHANI, A. A., S. BÖSER, N. BUZINSKY, M. C. CARMONA-BENITEZ, C. CLAESSENS, L. DE VIVEIROS, P. J. DOE, M. FERTL, J. A. FORMAGGIO, J. K. GAISON, L. GLADSTONE, M. GUIQUE, J. HARTSE, K. M. HEEGER, X. HUYAN, A. M. JONES, K. KAZKAZ, B. H. LAROQUE, M. LI, A. LINDMAN, E. MACHADO, A. MARSTELLER, C. MATTHÉ, R. MOHIUDDIN, B. MONREAL, R. MUELLER, J. A. NIKKEL, E. NOVITSKI, N. S. OBLATH, J. I. PEÑA, W. PETTUS, R. REIMANN, R. G. H. ROBERTSON, D. R. D. JESÚS, G. RYBKA, L. SALDAÑA, M. SCHRAM, P. L. SLOCUM, J. STACHURSKA, Y. H. SUN, P. T. SURUKUCHI, J. R. TEDESCHI, A. B. TELLES, F. THOMAS, M. THOMAS, L. A. THORNE, T. THÜMMLER, L. TVRZNIKOVA, W. V. D. PONTSEELE, B. A. VANDEVENDER, J. WEINTROUB, T. E. WEISS, T. WENDLER, A. YOUNG, E. ZAYAS, and A. ZIEGLER (2023)

“Cyclotron Radiation Emission Spectroscopy of Electrons from Tritium Beta Decay and  $^{83\text{m}}\text{Kr}$  Internal Conversion,” 2303.12055.

- [5] ESFAHANI, A. A., S. BÖSER, N. BUZINSKY, M. C. CARMONA-BENITEZ, C. CLAESSENS, L. DE VIVEIROS, P. J. DOE, S. ENOMOTO, M. FERTL, J. A. FORMAGGIO, J. K. GAISON, M. GRANDO, K. M. HEEGER, X. HUYAN, A. M. JONES, K. KAZKAZ, M. LI, A. LINDMAN, C. MATTHÉ, R. MOHIUDDIN, B. MONREAL, R. MUELLER, J. A. NIKKEL, E. NOVITSKI, N. S. OBLATH, J. I. PEÑA, W. PETTUS, R. REIMANN, R. G. H. ROBERTSON, G. RYBKA, L. SALDAÑA, M. SCHRAM, P. L. SLOCUM, J. STACHURSKA, Y. H. SUN, P. T. SURUKUCHI, J. R. TEDESCHI, A. B. TELLES, F. THOMAS, M. THOMAS, L. A. THORNE, T. THÜMMLER, W. V. D. PONTSEELE, B. A. VANDEVENDER, T. E. WEISS, T. WENDLER, and A. ZIEGLER (2022) “The Project 8 Neutrino Mass Experiment,” 2203.07349.
- [6] REIMANN, R. (2022) “Project 8: R&D for a next-generation neutrino mass experiment,” *PoS*, **PANIC2021**, p. 283.
- [7] LAROQUE, B. (2020) “Zero-deadtime processing in beta spectroscopy for measurement of the non-zero neutrino mass,” *EPJ Web Conf.*, **245**, p. 01014.
- [8] “Antenna Arrays for Physics Measurements with Large-scale CRES Detectors,” *In preparation*.
- [9] ESFAHANI, A. A., V. BANSAL, S. BÖSER, N. BUZINSKY, R. CERVANTES, C. CLAESSENS, L. DE VIVEIROS, P. J. DOE, M. FERTL, J. A. FORMAGGIO, L. GLADSTONE, M. GUIQUE, K. M. HEEGER, J. JOHNSTON, A. M. JONES, K. KAZKAZ, B. H. LAROQUE, M. LEBER, A. LINDMAN, E. MACHADO, B. MONREAL, E. C. MORRISON, J. A. NIKKEL, E. NOVITSKI, N. S. OBLATH, W. PETTUS, R. G. H. ROBERTSON, G. RYBKA, L. SALDAÑA, V. SIBILLE, M. SCHRAM, P. L. SLOCUM, Y.-H. SUN, J. R. TEDESCHI, T. THÜMMLER, B. A. VANDEVENDER, M. WACHTENDONK, M. WALTER, T. E. WEISS, T. WENDLER, and E. ZAYAS (2019) “Electron radiated power in cyclotron radiation emission spectroscopy experiments,” *Phys. Rev. C*, **99**, p. 055501.  
URL <https://link.aps.org/doi/10.1103/PhysRevC.99.055501>
- [10] BUZINSKY, N. (2021) *Statistical Signal Processing and Detector Optimization in Project 8*, Ph.D. thesis, Massachusetts Institute of Technology.
- [11] ESFAHANI, A. A., S. BÖSER, N. BUZINSKY, M. CARMONA-BENITEZ, C. CLAESSENS, L. DE VIVEIROS, M. FERTL, J. FORMAGGIO, L. GLADSTONE, M. GRANDO, J. HARTSE, K. HEEGER, X. HUYAN, A. JONES, K. KAZKAZ, M. LI, A. LINDMAN, C. MATTHÉ, R. MOHIUDDIN, B. MONREAL, R. MUELLER, J. NIKKEL, E. NOVITSKI, N. OBLATH, J. PEÑA, W. PETTUS, R. REIMANN,

- R. ROBERTSON, L. SALDAÑA, P. SLOCUM, J. STACHURSKA, Y.-H. SUN, P. SU-RUKUCHI, A. TELLES, F. THOMAS, M. THOMAS, L. THORNE, T. THÜMMLER, L. TVRZNIKOVA, W. V. D. PONTSEELE, B. VANDEVENDER, T. WEISS, T. WENDLER, E. ZAYAS, A. ZIEGLER, and P. . COLLABORATION (2023) “SYNCA: A Synthetic Cyclotron Antenna for the Project 8 Collaboration,” *Journal of Instrumentation*, **18**(01), p. P01034.  
URL <https://dx.doi.org/10.1088/1748-0221/18/01/P01034>
- [12] KAY, S. (1998) *Fundamentals of Statistical Signal Processing: Detection Theory, Volume II*, Pearson.
- [13] ASHTARI ESFAHANI, A. ET AL. (2019) “Locust: C++ software for simulation of RF detection,” *New J. Phys.*, **21**, p. 113051, 1907.11124.
- [14] <https://www.nvidia.com/en-us/data-center/v100/>.
- [15] <https://www.nvidia.com/en-us/data-center/h100/>.
- [16] HE, K., X. ZHANG, S. REN, and J. SUN (2016) “Deep Residual Learning for Image Recognition,” in *2016 IEEE Conference on Computer Vision and Pattern Recognition (CVPR)*, pp. 770–778.
- [17] SIMONYAN, K. and A. ZISSEMAN (2015) “Very Deep Convolutional Networks for Large-Scale Image Recognition,” in *3rd International Conference on Learning Representations, ICLR 2015, San Diego, CA, USA, May 7-9, 2015, Conference Track Proceedings* (Y. Bengio and Y. LeCun, eds.).  
URL <http://arxiv.org/abs/1409.1556>
- [18] WORKMAN, R. L. and OTHERS (2022) “Review of Particle Physics,” *PTEP*, **2022**, p. 083C01.
- [19] FORMAGGIO, J. A., A. L. C. DE GOUVÊA, and R. G. H. ROBERTSON (2021) “Direct measurements of neutrino mass,” *Physics Reports*, **914**, pp. 1–54, direct measurements of neutrino mass.  
URL <https://www.sciencedirect.com/science/article/pii/S0370157321000636>
- [20] AKER, M. ET AL. (2022) “Direct neutrino-mass measurement with sub-electronvolt sensitivity,” *Nature Physics*, **18**(2), pp. 160–166.  
URL <https://doi.org/10.1038/s41567-021-01463-1>
- [21] MONREAL, B. and J. A. FORMAGGIO (2009) “Relativistic Cyclotron Radiation Detection of Tritium Decay Electrons as a New Technique for Measuring the Neutrino Mass,” *Phys. Rev. D*, **80**, p. 051301, 0904.2860.
- [22] ASNTER, D. M. ET AL. (2015) “Single electron detection and spectroscopy via relativistic cyclotron radiation,” *Phys. Rev. Lett.*, **114**(16), p. 162501, 1408.5362.

- [23] ASHTARI ESFAHANI, A. ET AL. (2017) “Determining the neutrino mass with cyclotron radiation emission spectroscopy—Project 8,” *J. Phys. G*, **44**(5), p. 054004, 1703.02037.
- [24] ESFAHANI, A. A. ET AL. (2022) “The Project 8 Neutrino Mass Experiment,” in *2022 Snowmass Summer Study*, 2203.07349.
- [25] ASHTARI ESFAHANI, A. ET AL. (2021) “Bayesian analysis of a future  $\beta$  decay experiment’s sensitivity to neutrino mass scale and ordering,” *Phys. Rev. C*, **103**, p. 065501.  
URL <https://link.aps.org/doi/10.1103/PhysRevC.103.065501>
- [26] BODINE, L. I., D. S. PARNO, and R. G. H. ROBERTSON (2015) “Assessment of molecular effects on neutrino mass measurements from tritium  $\beta$  decay,” *Phys. Rev. C*, **91**(3), p. 035505, 1502.03497.
- [27] ASHTARI ESFAHANI, A. ET AL. (2019) “Locust: C++ software for simulation of RF detection,” *New Journal of Physics*, **21**(11), p. 113051.  
URL <https://doi.org/10.1088/1367-2630/ab550d>
- [28] JACKSON, J. D. (1999) *Classical electrodynamics*, 3rd ed., Wiley, New York, NY.  
URL <http://cdsweb.cern.ch/record/490457>
- [29] FURSE, D. ET AL. (2017) “Kassiopeia: a modern, extensible C++ particle tracking package,” *New Journal of Physics*, **19**(5), p. 053012.  
URL <https://doi.org/10.1088/1367-2630/aa6950>
- [30] BALANIS, C. (2011) *Modern Antenna Handbook*, Wiley.  
URL <https://books.google.com/books?id=UYpV8L8GNcwc>
- [31] ——— (2015) *Antenna Theory: Analysis and Design*, Wiley.  
URL <https://books.google.com/books?id=PTFcCwAAQBAJ>
- [32] <https://www.ansys.com/products/electronics/ansys-hfss>.
- [33] WIRTH, W. (2001) *Radar Techniques Using Array Antennas*, Institution of Engineering and Technology.  
URL <https://books.google.com/books?id=ALht42gkzLsC>